DESIGN AND DEVELOPMENT OF A NEXT GENERATION ENERGY STORAGE FLYWHEEL

A Dissertation

by

XIAOJUN LI

Submitted to the Office of Graduate and Professional Studies of
Texas A&M University
in partial fulfillment of the requirements for the degree of

DOCTOR OF PHILOSOPHY

Chair of Committee,	Alan Palazzolo
Committee Members,	Bryan Rasmussen
	Chii-Der Suh
	Hamid Toliyat
Head of Department,	Andreas A. Polycarpou

May 2018

Major Subject: Mechanical Engineering

ABSTRACT

Energy storage is crucial for both smart grids and renewable energy sources such as wind or solar, which are intermittent in nature. Compared to electrochemical batteries, flywheel energy storage systems (FESSs) offer many unique benefits such as low environmental impact, high power quality, and larger life cycles. This dissertation presents the design and development of a novel utility-scale FESS that features a shaftless, hubless rotor. The unique shaftless design gives it the potential of a doubled energy density and a compact form factor. Its energy and power capacities are 100 kWh and 100 kW, respectively. The flywheel is made of high-strength steel, which makes it much easier to manufacture, assemble, and recycle. Steels also cost much less than composite materials. In addition, the system incorporates a new combination active magnetic bearing. Its working principle and the levitation control for the flywheel are presented. The development of an integrated, coreless, permanent-magnet (PM) motor/generator for the flywheel is briefly discussed as well. Initial test results show that the magnetic bearing provides stable levitation for the 5443-kg flywheel with small current consumptions. Furthermore, this dissertation formulates and synthesizes a detailed model for designing and simulating a closed-loop control system for the proposed flywheel system at high speed. To this end, the magnetic bearing supporting structure is considered flexible and modeled by finite element modeling. The magnetic bearing is characterized experimentally by static and frequency-dependent coefficients, the latter of which are caused by eddy current effects and presents challenges to the levitation control. Sensor-

runout disturbances are measured and included in the model. System nonlinearities in power amplifiers and the controller are considered as well. Even though the flywheel has a large ratio of the primary-to-transversal moment of inertias, Multi-Input-Multi-Output (MIMO) feedback control demonstrates its effectiveness in canceling gyroscopic torques and stabilize the system. Various stages of PD controllers, lead/lag compensators, and notch filters are also implemented to suppress the high-frequency sensor disturbances and structural vibrations.

DEDICATION

To my family.

For your patience, support and understanding.

ACKNOWLEDGMENTS

I would like to firstly thank Dr. Palazzolo for his immeasurable considerations during my graduate study at Texas A&M University. I would also like to express my gratitude to Dr. Toliyat, Dr. Rasmussen and Dr. Suh for serving as my committee members.

This project won't be possible without the help of the following colleagues: Erwin Thomas, Dustin Tingey, Randall Tucker and Bahar Anvari. And the following Texas A&M student: Greg Hluchan, Hari Shrestha, Matthew Charles, Shiva Thapa, Manjil Magar, Segun Tyler, Shivanand Pattanshetti, Stephen Farris, Billy Taylor, Jose Bendana, Shyam Balasubramanian, Kiriti Madugula and others.

CONTRIBUTORS AND FUNDING SOURCES

This work was supported by a dissertation committee consisting of Professor Alan Palazzolo, Professor Bryan Rasmussen, and Professor Chii-Der Suh of the Department of Mechanical Engineering and Professor Hamid Toliyat of the Department of Electrical and Computer Engineering.

The initial conceptual design of the shaftless flywheel was developed by Professor Alan Palazzolo, Randall Tucker, and Zhiyang Wang. The motor design is done by Bahar Anvari. Dustin Tingey has contributed to making the mechanical drawings. All other work conducted for the dissertation was completed by the student.

Graduate study was supported by the US Department of Energy, and partially supported by the Energy Institute of Texas A&M University and the TRC at Turbo Lab, Texas A&M.

NOMENCLATURE

AMB	Active Magnetic Bearing
C5AMB	Combination 5 DOF Magnetic Bearing
DOF	Degree of Freedom
EMCM	Equivalent Magnetic Circuit Model
EM	Electromagnetic
ESS	Energy Storage System
FESS	Flywheel Energy Storage System
MB	Magnetic Bearing
MMF	Magnetomotive Force
MG	Motor/Generator
PA	Power Amplifier
PM	Permanent Magnet
SHFES	Shaftless High Strength Steel Flywheel Energy Storage System
VBT	Vertical Ball Transfer

Math: Magnetics

A_r	Radial Pole Surface Area
i	Enumeration for the Axial Poles
j	Enumeration for the Radial Poles
$F_{dw}^{pm}(i)$	MMF of the ith Lower PM

$F_{up}^{pm}(i)$	MMF of the ith Upper PM
F_{ia}	MMF of the Axial Coil
$F_{it}(i)$	MMF of the ith Tilt Coil
$F_{ir}(j)$	MMF of the jth Radial Coil
$\phi_{a1}(i)$	Flux of ith Inner Axial Pole
$\phi_{a2}(i)$	Flux of ith Outer Axial Pole
$\phi_t(i)$	Flux of ith PM Pole
$\phi_{ri}(j)$	Flux of jth Inner Radial Pole
$\phi_{ro}(j)$	Flux of jth Outer Radial Pole
ϕ_{a1}	Total Flux of Inner Axial Poles
ϕ_{a2}	Total Flux of Outer Axial Poles
ϕ_a	Total Flux of Axial Poles
ϕ_t	Total Flux of PM Poles
ϕ_{ri}	Total Flux of Inner Radial Poles
ϕ_{ro}	Total Flux of Outer Radial Poles
ϕ_r	Total Flux of Radial Poles
$\mathbf{\Phi}_{ri}$	Flux Vector of Inner Radial Pole
$\mathbf{\Phi}_{ro}$	Flux Vector of Outer Radial Pole
$\mathbf{\Phi}_a$	Flux Vector of Axial Pole
$\mathbf{\Phi}_t$	Flux Vector of PM Pole
$R_{a1}(i)$	Reluctance of ith Inner Axial Pole
$R_{a2}(i)$	Reluctance of ith Outer Axial Pole

$R_t(i)$	Reluctance of ith PM Pole
$R_{ri}(j)$	Reluctance of jth Inner Radial Pole
$R_{ro}(j)$	Reluctance of jth Outer Radial Pole
R_{a1}	Total Reluctance of Inner Axial Poles
R_{a2}	Total Reluctance of Outer Axial Poles
R_a	Total Reluctance of Axial Poles
R_t	Total Reluctance of PM Poles
R_{ri}	Total Reluctance of Inner Radial Poles
R_{ro}	Total Reluctance of Outer Radial Poles
R_r	Total Reluctance of Radial Poles
R_{nr}	Total Reluctance of Non-Radial Poles
$\mathbf{R}_{a1}$	Reluctance Matrix of Inner Axial Pole
$\mathbf{R}_{a2}$	Reluctance Matrix of Outer Axial Pole
$\mathbf{R}_t$	Reluctance Matrix of PM Pole
$\mathbf{R}_{ri}$	Reluctance Matrix of Inner Radial Pole
$\mathbf{R}_{ro}$	Reluctance Matrix of Outer Radial Pole
θ_x	X-Axis tilt motion of the Flywheel
θ_y	Y-Axis tilt motion of the Flywheel
(r, ψ)	Polar Coordinate of the Horizontal Plane
$g(r, \psi)$	Tilt Motion Induced Airgap
$\mathbf{J}_n$	n×n All One Matrix
$\mathbf{0}_{n,m}$	n×m All Zero Matrix

μ_0	Magnetic Permeability of Free Space
x	X-Axis Displacement of the Flywheel
y	Y-Axis Displacement of the Flywheel
z	Axial Displacement of the Flywheel

Math: Dynamics & Control

B_{pm}	Flux Density Associated with Permanent Magnets
B_i	Flux Density Associated with Control Current
$\boldsymbol{C}_s$	Damping Matrix of the Supporting Structure
$\boldsymbol{D}$	Matrix of the Derivative Gain
$\boldsymbol{D}_f$	Transformation Matrices of Structure-to-C5AMB Forces
$\boldsymbol{D}_s$	Transformation Matrices of Structure-to-AMB Sensory Signal
E	Energy Capacity of the Flywheel
$\boldsymbol{G}_{sn}$	Matrix of the Sensory Gain
$\boldsymbol{G}_f$	Gyroscopic Matrix of the Flywheel Rotor
$\boldsymbol{G}_{PA}$	Matrix of the PA feedback Gain
$\boldsymbol{i}$	Vector of the PA Output Current
K	Shape Factor
$\boldsymbol{K}_p$	Position Stiffness Matrix of the C5AMB
$\boldsymbol{K}_i$	Current Stiffness Matrix of the C5AMB
$\boldsymbol{K}_s$	Stiffness Matrix of the Supporting Structure

$\boldsymbol{K_{PA}}$	Matrix of the PA Output Gain
$\boldsymbol{L}$	Matrix of the Coil Inductance
$\boldsymbol{L_l}$	Matrix of the Lead Compensators Transfer Functions
$\boldsymbol{L_g}$	Matrix of the Lag Compensators Transfer Functions
$\boldsymbol{M_s}$	Mass/Inertia Matrix of the Supporting Structure
$\boldsymbol{M_f}$	Mass/Inertia Matrix of the Flywheel Rotor
$\boldsymbol{N_f}$	Matrix of the Low Pass Filters Transfer Functions
$\boldsymbol{P}$	Matrix of the Proportional Gain
$\boldsymbol{q_s}$	State Vector of the Supporting Structure
$\boldsymbol{q_s^c}$	State Vector of the C5AMB
$\boldsymbol{q_r}$	Vector of the Sensory Disturbance
$\boldsymbol{q_f}$	State Variable of the Flywheel Rotor
$\boldsymbol{R}$	Matrix of the Coil Resistance
$\boldsymbol{TF_{if}}$	Matrix of C5AMB Eddy Current Effect Dynamics
$\boldsymbol{T_{sn}}$	Matrix of the Sensory Filter Constant
$\boldsymbol{V}$	Vector of the PA Output Voltage

TABLE OF CONTENTS

LIST OF FIGURES

LIST OF TABLES

CHAPTER I

INTRODUCTION*

The Paris Climate Pact, which will take effect in 2020, has called on nations worldwide to "hold the increase in average global temperature to well below 2° C above the pre-industry level" and to pursue the goal of 1.5° above the pre-industry level. To achieve this target, it is critical to reducing greenhouse gas emissions generated by fossil fuels. As depicted in Figure 1.1, in the year of 2010, global carbon-dioxide emissions produced by fossil-fuel have reached over 9,000 million metric ton [1], a 500% increase comparing to 1900.

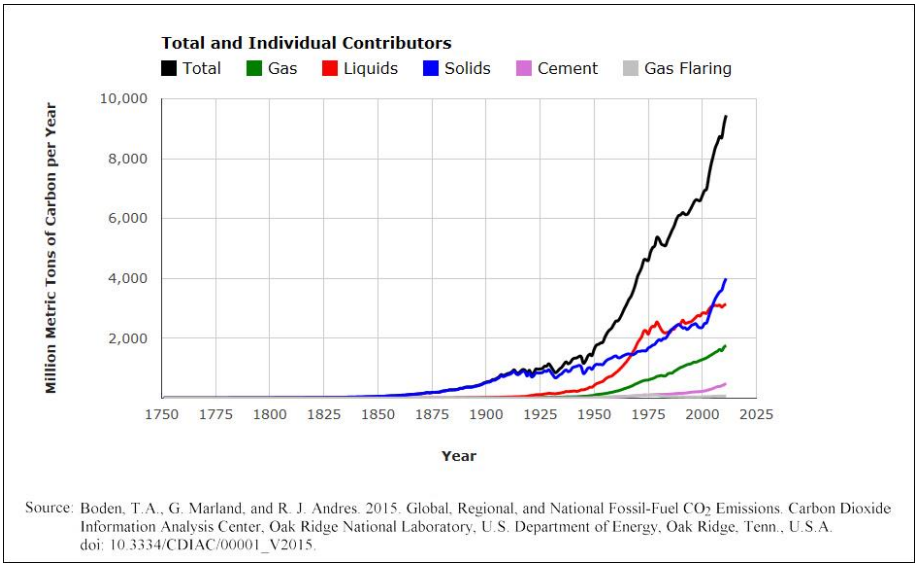

Figure 1.1 Estimation of World Carbon-Dioxide Emission (1900-2025), reprinted from [1]

*Part of this chapter is reprinted with permission from "A Utility Scale Flywheel Energy Storage System with a Shaftless, Hubless, High-Strength Steel Rotor" by X. Li and B. Anvari, 2017., *IEEE Transactions on Industrial Electronics*, PP, 1-1, Copyright [2017] by IEEE.

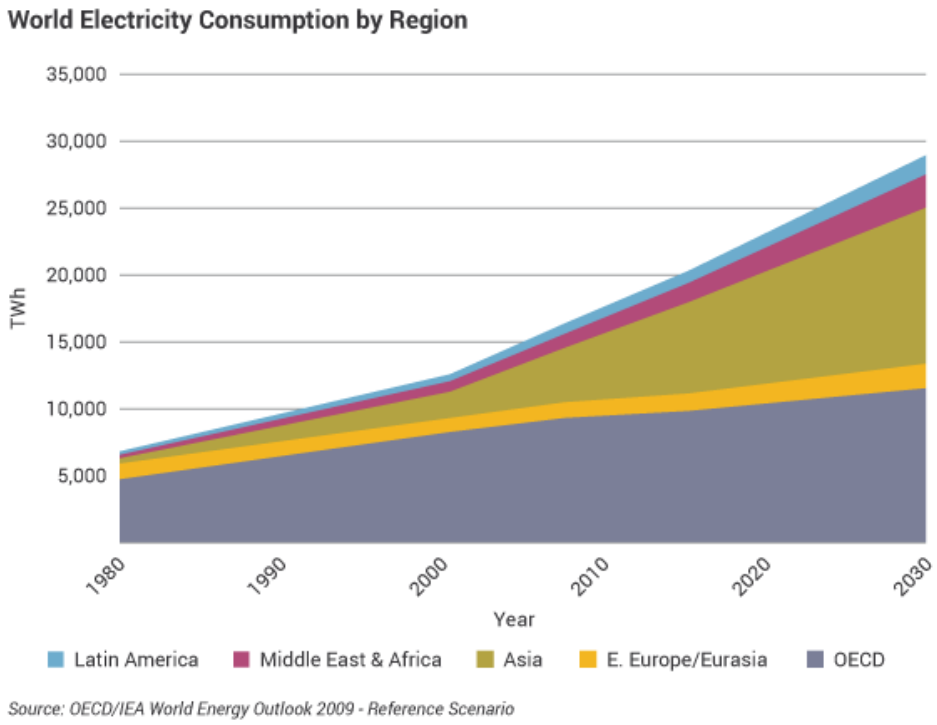

Figure 1.2 World Electricity Demand: from 1980 to 2030, reprinted from [3]

A significant amount of fossil-fuel was consumed in power stations. In 2015, 37% of the CO2 emission in the U.S. was associated with electricity generation [2]. On the other hand, rapid economic development is driving energy consumptions. As depicted in Figure 1.2, the world electricity demand will approach 30,000 TWh and double itself comparing to 2010 [3]. Considerable efforts have been made in renewable energy technologies such as wind and solar technology to provide sustainable and clean energies, which is ideal for replacing fossil-fuel generated electricity. Also, renewable energies are more available at many places in the world, where electrical shortages are common due to inadequate infrastructures. However, the intermittent nature of these energy sources prevents them from being reliable sources for micro-grids. Energy storage systems can play an essential

role in solving both problems. Firstly, they can be used to efficiently distribute electricity by balancing the supply and the load. Secondly, they can be used for storing intermittent renewable energy sources to create reliable micro-grids. The existing energy storage systems employ various technologies including hydro-electrical, batteries, supercapacitors and energy storage flywheels. Owing to its recent advancement, flywheel energy storage systems (FESSs) are gaining attention for providing solutions for both energy storage and distribution.

Due to their high power rating, superior depth of discharge and number of lifetime charge cycles, when compared to electrochemical batteries [4], FESSs are ideal for power grid regulations to improving distribution efficiency, as well as smoothing power output from renewable energy sources such as wind/solar farms. FESSs can convert electrical energy and store it as kinetic energy. A bidirectional power converter allows the stored energy to be discharged back to electrical power [4]. They are usually supported by active magnetic bearing (AMB) systems to avoid any friction loss or wear by conventional bearings. Therefore, FESSs can store energy at high efficiency over a long time. Apart from frequency regulation and renewable energy, typical applications of FESSs also include uninterruptible power service (UPS), hybrid locomotives, power pulsation.

Different energy storage methods can be measured by the following metrics:

- Capital cost (per kW and kWh)
- Environment impact
- Power capability
- Energy capability

- Life cycles/ operational life
- Energy efficiency
- Energy deterioration
- Discharge / charge time
- Technological feasibility

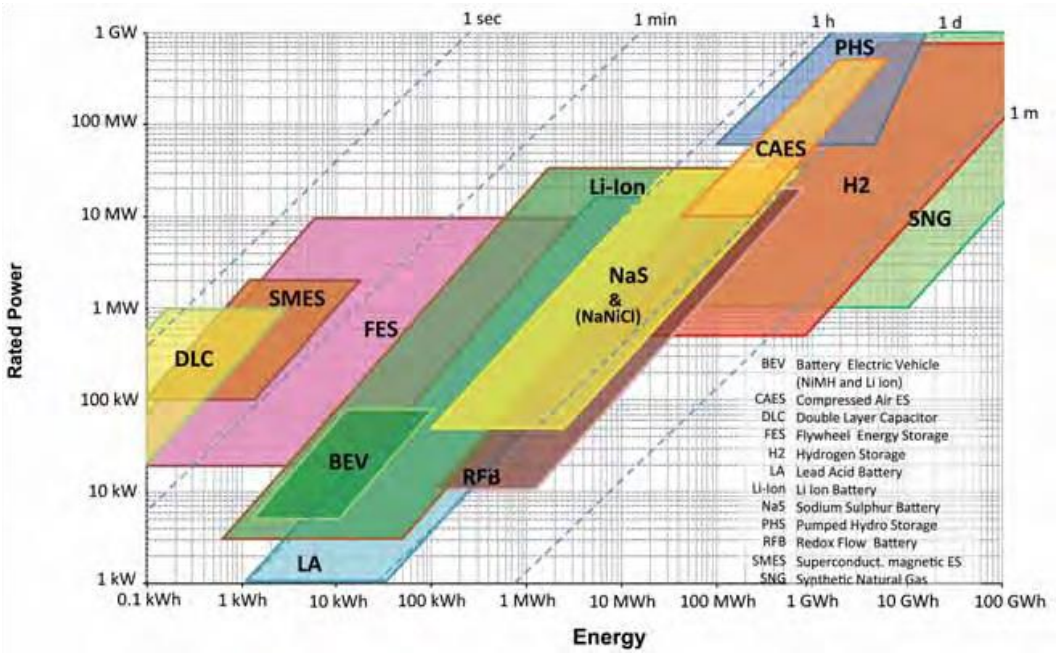

Figure 1.3 Comparison of the Rated Power, Energy Content and Discharge Time of Different Energy Storage Technologies, reprinted from [5]

Comparison between different ESSs is depicted in Figure 1.3. The primary candidate for energy storage technologies is Flywheel, capacitor, and battery (see Table 1.1). In summary:

- The lithium-ion battery has high energy density but much less power density.
- Both flywheel and supercapacitor has high power density and high life cycles

- Supercapacitor has a narrower discharge duration and significant self-discharges
- The flywheel is also highly efficient and has the least environmental impact (no chemicals)

TABLE 1.1 COMPARISON OF DIFFERENT ENERGY STORAGE TECHNOLOGIES, REPRINTED FROM [6]

	Battery	Flywheel
Cost /kW	average	good
Cost /kWh	good	average
Energy Density	good	average
Power Density	average	good
Life cycles	average	good
Energy Efficiency	average	good
maturity	good	good
Response time	good	good
Environment impact	poor	good

Challenges and Motivations

The current FESSs are not yet widely adopted as a utility-scale energy storage solution. They have higher capital cost than electrochemical batteries [7,8]. For instance, the Beacon Power's flywheel system cost almost ten times higher than a Li-on battery system with similar energy capacity even though it can provide competitive cost/(kWh*cycles) considering its higher charge/discharge cycles. Comparing to other technologies like batteries or supercapacitors, FESSs have "moving" parts, thus are considered to have higher uncertainties in failure modes. Composite flywheels are particularly subject to this shortcoming because of their higher operational speeds and the unpredictable mechanical property of the material. At last, almost all the existing flywheel systems are designed for specific applications such as frequency regulation or UPS. They require specialized knowledge and techniques for manufacture, assembly, and maintenance, preventing them being produced en masse with a lower cost per unit.

Research Objects/Contributions

This thesis is aimed at designing a novel flywheel energy storage system that fills the gap between flywheel and well-established energy storage systems such as Li-ion batteries by providing a cost-effective and recyclable solution with minimal environmental impact:

- To minimize the cost per kWh and kW for flywheel energy storage systems. Make it competitive with the mainstream Li-ion battery and superior to older generation flywheels.
- To increase the recyclability and reduce the environmental impact of flywheel systems.
- To improve the manufacturability of the system and to achieve an efficient, compact design by eliminating redundant components.
- Develop a full-scale flywheel system including a combination active magnetic bearing.
- Develop a feedback control system for the magnetic levitation, verify experimentally.
- Develop a preliminary motor/generator system
- Low-speed motor/generator test with full magnetic levitation control
- Simulation and control of the flywheel system at high speed

Dissertation Outline

Chapter II gives a literature review of current research and commercial developments in flywheel energy storage systems. Chapter III provides an overview of the SHFES system components. In Chapter IV, the analysis of shaftless flywheel and a design improvement is presented. In Chapter V, the modeling and analysis of the combination magnetic bearing are presented. In Chapter VI, the modeling and control of the SHFES are discussed in detail. Development and experimental testing results of the SHFES are given in Chapter VII. Conclusions and future work are made in the last chapter.

The bibliography follows an ASME journal format.

CHAPTER II

LITERATURE REVIEW

Overview of Conventional FESS

Unlike electrochemical-based battery system, a typical FESS is an electromechanical device that converts electricity into kinetic energy and releases kinetic energy to electricity. To realize its functions, a FESS includes a rotor with a significant moment of inertia. The rotor is either made of composite or metallic material. Energy is stored in the form of rotational kinetic energy. When it is rotating, the flywheel is supported by a set of bearings, which are either mechanical bearings or magnetic bearings. To enable the energy conversion process, a FESS also includes an electrical machine and its power electronics. Other auxiliary components of a FESS include a vacuum pump, catcher bearings, and others. As depicted in Figure 2.1 , the NASA G2 flywheel is one of the pioneering modern FESSs developed in the 2000s [9].

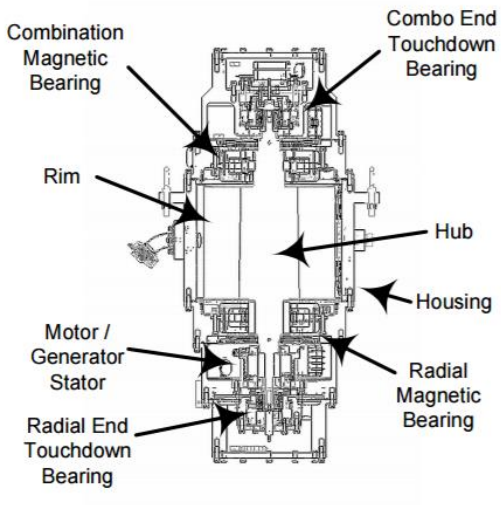

Figure 2.1 The NASA G2 Flywheel, reprinted from [9]

FESS Components

The components of a FESS are briefly introduced in this section.

Rotor and shaft

The rotor (sometimes referred as flywheel or rim) is the essential part of a FESS. This part stores most of the kinetic energy during the operation. The rotor is typically carried by a shaft through its hub. The shaft, which is supported by bearings, also acts as the rotating part of the motor/generator. The orientation of the rotor-shaft assembly can be horizontal or vertical. Designing of the rotor is usually the starting point of the entire FESS design. Two kinds of materials are frequently chosen in building the rotor: composite and metal.

Motor/Generator (MG)

Generally, an electrical machine is needed to convert the electrical energy into kinetic energy and vice versa. It is acting as a motor and generator. Permanent Magnet Synchronous Motors (PMSM) are popular options for flywheel applications because of their high efficiency, high performance, and compact size. Other electrical machines such as induction motors or switch reluctance motors are also reported being designed for flywheels [10]. The M/G's design is a crucial factor affecting flywheel's power rating, which is based on their torque density and current carrying capacity.

Power electronics

Power electronics can be viewed as an interface between the FESS and electrical load/ supply. A typical case is the use of a back-to-back converter includes two voltage source controllers (VSC). The VSCs switch their roles between rectifiers and inverters to

realize the transformation between charge and discharge modes. The current carrying capacity of the VSC is also a critical factor in determining the FESS's power rating.

Operational bearings

Operational bearings refer to the set of bearings that support the rotor when it is under normal operation. One of the critical features of a modern FESS is the use of Magnetic Bearings (MB). MB allows the rotor being spinning without physically contacting any other components to eliminate the friction loss, which is inevitable for mechanical bearings. For ball bearings, power loss is proportional to the rotor's spinning speed. Therefore, it prevents the FESS from running at a higher speed. Fluid-film bearings may have a lower power loss, but they need an extra lubrication system. The MB of a FESS can be either active or passive. An active magnetic bearing (AMB) requires power electronics and a feedback controller. It can be homopolar, which means it has permanent magnets to provide the bias flux, or heteropolar, which does not include permanent magnets. Many commercial MBs are heteropolar AMBs due to the lower cost.

Catcher/touchdown bearings

Catcher Bearings (CB) are sometimes referred to as touchdown or backup bearings. They are auxiliary bearings that are used as a backup in case of MB failures caused by power shortage or excessive external disturbances. CBs are not designed to provide operational support in lieu of MBs. Ball bearings are typically adopted as CBs. To increase the damping coefficients so that the rotor's kinetic energy can be quickly dissipated after dropping, squeeze film dampers are sometimes added to the CB system [11].

Controller

Both MB and M/G requires feedback control system. MB supported rotors are complex, frequency dependent system which demands fast and high order compensators. In addition, data acquisition and monitoring systems are used to monitor the FESS's conditions such as rotor vibration, coil temperatures, and energy/power status.

Other components

Many of the housing/casing designs of FESSs also include a vacuum enclosure to reduce the windage loss when the flywheel is rotating at high speed. For mobile applications, the housing structure needs to be optimized to reduce its overall weight and provides vibration absorption to prevent the FESS from failures caused by excessive external vibrations. The flywheel that operates in a vacuum enclosure may also include other components such as an air pump for maintaining its vacuum status and an active cooling system for the MB and M/G.

Literature Review

Major research efforts are made in making innovative FESSs. They can generally be summarized in the following areas:

Research Focuses

Design and optimization of the flywheel rotor

Most of the research work focuses on the optimization of the composite flywheel. For example, A. C. Arvin and C. E. Bakis [12] proposed a concept design of a flywheel made of multiple rims, press-fit, filament wound composite materials. The optimization uses a simulated annealing algorithm and yields a specific energy of 40-50 kWh/kg. J. Abrahamsson et al. [13] presented an optimized high-speed kinetic buffer flywheel. The rotor comprises a solid composite shell of carbon and glass fibers in an epoxy matrix, constructed in one curing. R. F. Thelen et al. [14] proposed a 100KWh, 2MW flywheel made of composite material. It achieved a specific energy of 15-18 Wh/kg. Y. H. Ha et al. [15] studied the interferences and the rim thickness to maximize the specific energy of a multi-rim composite flywheel rotor. Up to five rims of graphite/Ep and glass/Ep are analyzed.

Design of innovative magnetic bearing and its control

Both P. Tsao [16] and Kailasan [17] have focused on designing integrated MB and M/G system along with the flywheel. T. H. Sung et al. [18] developed a 300Wh flywheel supported by two superconducting magnetic bearing. The superconducting magnetic bearing does not need active control and achieved 20,000 RPM spin speed. S. Jinji et al. [19] proposed a novel integrated radial hybrid magnetic bearing for small-sized

magnetically suspended control moment gyroscope (MSCMG), The MB can control four degrees of freedom motions. Magnetic bearing control is another critical fields. Albeit they may not be directly related to flywheel applications. J. Park [20] studied the MIMO control of a magnetically levitated FESS and showed its benefit to SISO control. [21] studied the control of AMB for a large order, flexible shaft which is modeled by FEA.

Design novel motor/generator and power electronics:

R. S. Talebi et al. [22] discussed the schemes to design power electronics and controllers such that the FESS has increased power output. The primary target was to increase the discharge power up to four times to the nominal rating of the PMSM. H. Hofmann and S. R. Sanders [23] presented a synchronous reluctance motor for flywheel application. The machine is rated 60KW at 48,000 RPM. A. S. Nagorny et al. [24] investigated the design aspects of PMSM for flywheel applications. In this study, permanent magnet properties and abilities to withstand demagnetization due to the temperature variations and armature reactions are considered.

Applications of FESSs

Uninterruptable power supply (*UPS*)

Many of the commercial flywheel systems are developed and marketed for UPS applications, the key advantages of flywheel-based UPSs include high power quality, longer life cycles, and low maintenance requirement. Active power Inc. [25] has developed a series of flywheels that are capable of 5 kWh and 675 kW for UPS application. The flywheel weight is 4976 kg. Calnetix's Vycon VDC is another example of FESS designed for UPS application [26]. The max power of VDC is 300KW with the max energy of 1.7 kWh. The operational range is from 36,750 RPM to 14,000 RPM. Flywheel-battery hybrid energy storage system also has been proposed to mitigate DC voltage ripple [27].

Renewable energy

FESSs have been used as an integral part of renewable energy resources such as solar farms or wind turbines. Since the wind speed is unpredictable, the power output of a wind turbine is not stable. Many FESSs have been proposed to smooth the output and increase the efficiency of a wind turbine [4,28–31]. R. Sebastián and R. Peña Alzola [4] presented the simulation of using a FESS for an isolated wind power system that consists of a wind turbine generator, a consumer load, a synchronous machine. The scheme is illustrated in Figure 2.2 . In [32], different connection topologies of FESSs with wind farms are investigated. For solar PVs, sun radiation varies within the daytime and are not available during the night. Therefore, ESS is irreplaceable. It was reported in [33] that a

high-temperature superconducting FESS was tested with solar cells experimentally at different spinning speeds to verify its functionality.

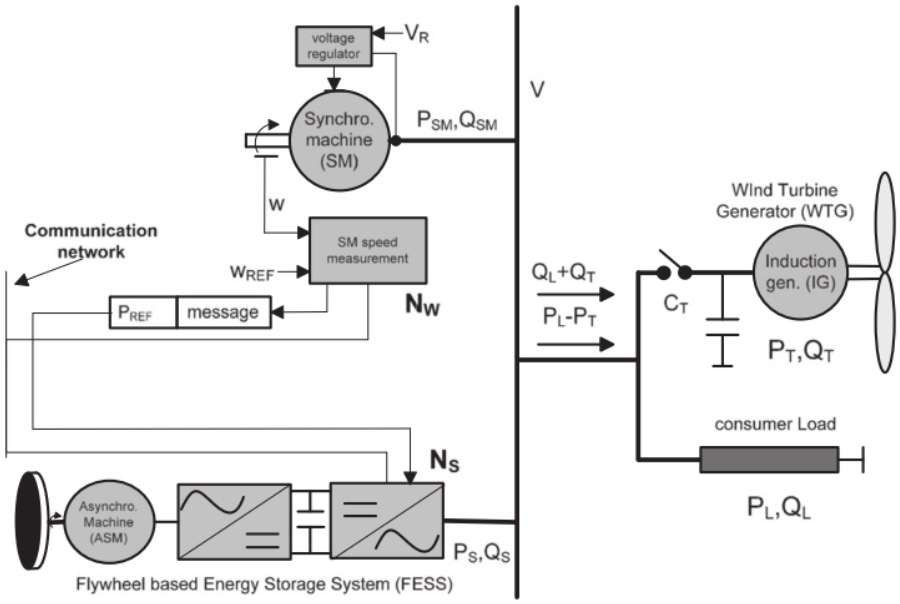

Figure 2.2 A FESS with an Isolated Wind Farm, reprinted from [4]

Frequency regulation (Power smoothing)

Most of the utility electricity is generated by gas turbines which are operating at a specific range of speeds for high efficiency. However, the load of a power grid is not constant. Minute-to-minute load variability results from the random turning on-and-off of millions of individual loads. There is a need to maintain the generation and load in real-time [34]. Whenever the load exceeds the generation, more kinetic energy is drawn from the turbine, causing it to slow down. Subsequently, the grid frequency deviates from its nominal value. FESS is an emerging technology in frequency regulation for many of its features. Such as, it reacts almost instantly, it has very high power to mass ratio, and it has a very long life cycle when compared to lion batteries. [35] is one of the early works that presented the use of FESS for voltage compensations.

Vehicles/transportation

The FESSs are used in many aspects in vehicular and transportation applications. They are used either as an ESS installed on the vehicle or as an ESS for charging the electric vehicle. M. Hedlund et al. [36] gives a review of FESS applications in cars. The high power to mass ratio is the key characteristics that enable the FESS to take the place of conventional powertrain systems. In [13], an energy buffer storing up to 867 Wh is presented, it is primarily for utility vehicles in urban traffic. R. A. Smith and K. R. Pullen [37] presented the optimization of flywheel parameters for braking energy recovery and acceleration of hybrid vehicles. Yimin Gao et al. [38] studied the application of FESS in hybrid vehicles. The power and energy of a passenger vehicle with a typical acceleration

profile are studied with FESSs to show what design decisions can be made for FESS based hybrid vehicles.

Aerospace

Many of the FESS research work in aerospace are focused on replacing lion-batteries with astronautical FESSs so that satellites or space stations can benefit from the flywheel's high-power rating and long life-cycle. In particular, FESS can also be used as an attitude control device [39]. The International Space Station has investigated the use of FESS carried out a flight test [40,41]. For aircraft, FESSs have been used in Electromagnetic Launching systems owing to their high power density [42]. So far, the author has not noticed any research activity of applying FESS directly on an aeronautical aircraft.

Current Commercial FESS Models

Some of the representative FESSs that have been commercialized are given as follows:

Beacon Power

Beacon Power Corporation commissioned a frequency regulation power plant with flywheels made of carbon fibers rotors (see Figure 2.3). The project costs over 40 million dollars and is capable of 20MW peak power output [43]. Based on the author's estimation, a single unit costs about $260k and is capable of 25KWh. The flywheel consists of a composite rotor (rim) with a metallic shaft. While the assembly is levitated by magnetic bearing in the vertical direction, the radial bearings are mechanical. The max spinning speed of this composite flywheel is 16,000 RPM. It has a life cycle of 175K, which is impressive.

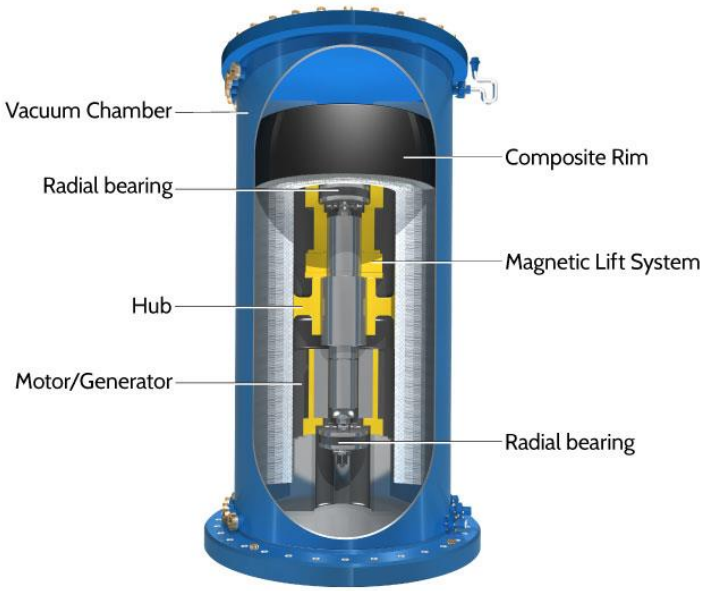

Figure 2.3 Beacon Power Flywheel, reprinted from [44]

Calnetix

The Calnetix VDC and REGEN systems [45] are products of formally Vycon inc. The VDC system is a UPS that can last up to 40 seconds. It was targeted at mission-critically applications, such as hospitals and data center. The REGEN model has been successfully applied at the Los Angeles (LA) metro subway [46] as a Wayside Energy Storage Substation (WESS). It was reported that the system has saved 10 to 18% of traction energy daily. The LA METRO WESS includes 4 flywheel unit and has an energy capacity of 8.33KWh. The power rating is 2 MW. The analysis in [46] shows that "WESS will save at least $99,000 per year at the Westlake/MacArthur Park TPSS". As depicted in Figure 2.4 , the Calnetix FESS is made of steel. The flywheel is also designed to be fully levitated by magnetic bearings. Its operational speed range is from 10,000 to 20,000 RPM.

Figure 2.4 Calnetix Flywheel REGEN, reprinted from [45]

Ricardo

Ricardo's flywheel system, the so call "TorqStor," took a very different technology approach. As depicted in Figure 2.5, the FESS does not include a motor/generator. Instead, the flywheel is coupled to a magnetic gear system to transfer power between FESS and automotive transmissions. The energy and power ratings are 55KWh and 101KW [36]. Being sealed in a vacuum container, the FESS is designed to be an integral part of the powertrain. This approach is an effort of downsizing the entire powertrain. This FESS was tested with a hydraulic speed matching system with a train model simulated in-the-loop. It showed that the FESS's effectiveness as a retrofit to diesel engines. The payback time is estimated to be 4.5 years with a 9MJ system [47].

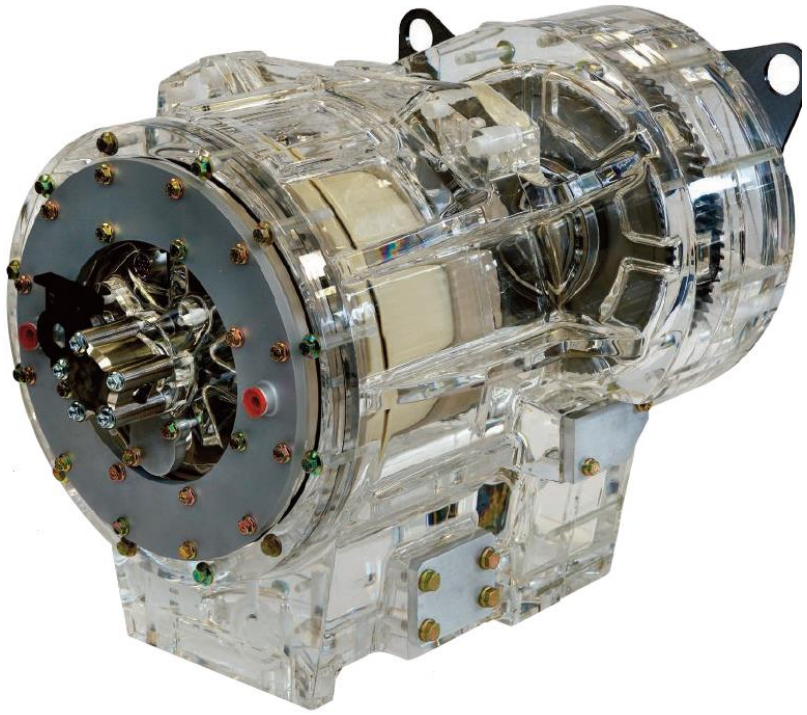

Figure 2.5 Ricardo TorqStor, reprinted from [48]

Amber Kinetics

Amber Kinetics [49] is a startup company in California who solely focuses on flywheels. Their prototype system is capable of 32 kWh and 8 kW, with continuous operation of 4 hours. The system does not need active cooling. It utilizes a hybrid mechanical/magnetic bearing where the magnetic bearing provides the most weight-lifting force, and the mechanical bearings are used for stabilizing the system. The self-discharge rate is quite impressive since it is only 65 W. The FESS includes one flywheel made of high strength steel. However, considering its weight of 10,000 lb., the energy density is not impressive. The system is mainly targeted at renewable energy applications. Especially for photovoltaic systems.

CHAPTER III

OVERVIEW OF THE SHFES*

The SHFES [50–52] design schematic is depicted in Figure 3.1. Its main specifications are summarized in Table 3.1. The shaftless flywheel is in the form of a solid disc. High strength steel is adopted as the building material so that it can provide a competitive power and energy capacity at a much lower cost. The manufacture and fabrications, as well as recycling, are also made easy with the composite component being replaced. Moreover, SHFES has predictable fatigue life cycles that are designed to last for 30 years of operation. As shown in Figure 3.1, the design of SHFES is entirely different from a conventional flywheel, which has a shaft and hole through its center. The core component of the SHFES is a shaftless, hubless, high strength steel (HSS) flywheel weighing 5443 kg, which is sandwiched between the AMB and the catcher bearings. On top of the flywheel lies a single Combination, 5 degree-of-freedom Active Magnetic Bearing (C5AMB) that is designed to provide 5-DOF magnetic suspension for the 5443kg rotor. The C5AMB is supported by a housing structure, which is bolted to the ground. A catcher bearing is installed underneath the flywheel for drop protection. Spacers are placed between the C5AMB and the flywheel in case of C5AMB failure. The custom coreless permanent magnets motor/generator is illustrated in Figure 3.1 as well.

---

*Part of this chapter is reprinted with permission from "A Utility Scale Flywheel Energy Storage System with a Shaftless, Hubless, High-Strength Steel Rotor" by X. Li and B. Anvari, 2017., *IEEE Transactions on Industrial Electronics*, PP, 1-1, Copyright [2017] by IEEE.

The motor coils are installed on a movable holding structure. During charge/discharge, they will be inserted into the flywheel's motor slot. To increase its efficiency, the flywheel is designed to work in a vacuum chamber.

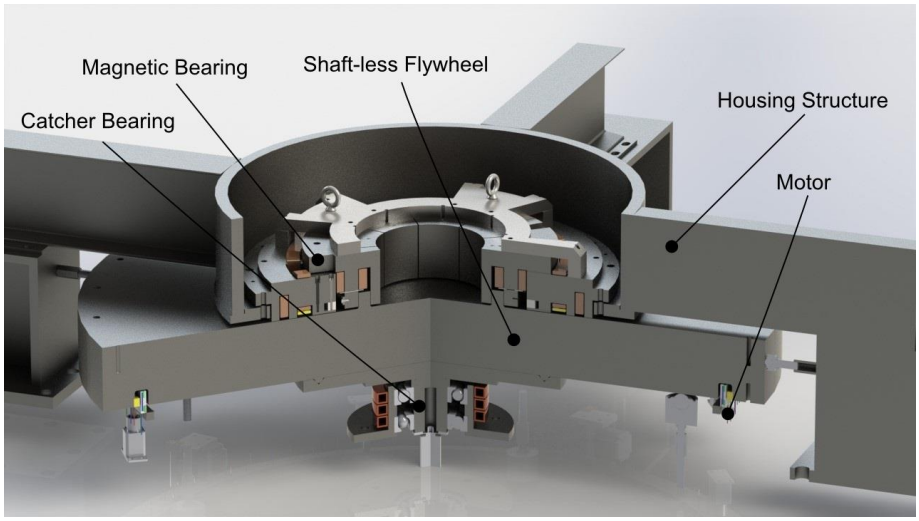

(a)

(b)

Figure 3.1 The SHFES with Rated Energy and Power of 100kWh/100kW.
(a) Section View of the SHFES with System Components Illustrated. (b) the Full-Scale SHFES

TABLE 3.1 FLYWHEEL SPECIFICATIONS

Parameter Name	Quantity	Unit
Outer diameter/	2133	[mm]
Height	20	[mm]
Mass	5443	[kg]
Moment of inertia	3087	[kg·m^2]
Rotational speed	5000	[rpm]
Tip speed	558	[m/s]
Energy/Power capacity	100/100	[kWh/kW]
Materials	4340	AISI
Material tensile strength	1500	[Mpa]
Linear relative magnetic permeability	200	-

The advantage of the SHFES is summarized in Table 3.2. It made considerable technology advancement by reducing the overall cost (see Figure 3.2), both in cost per energy capacity and cost per lifetime energy capacity.

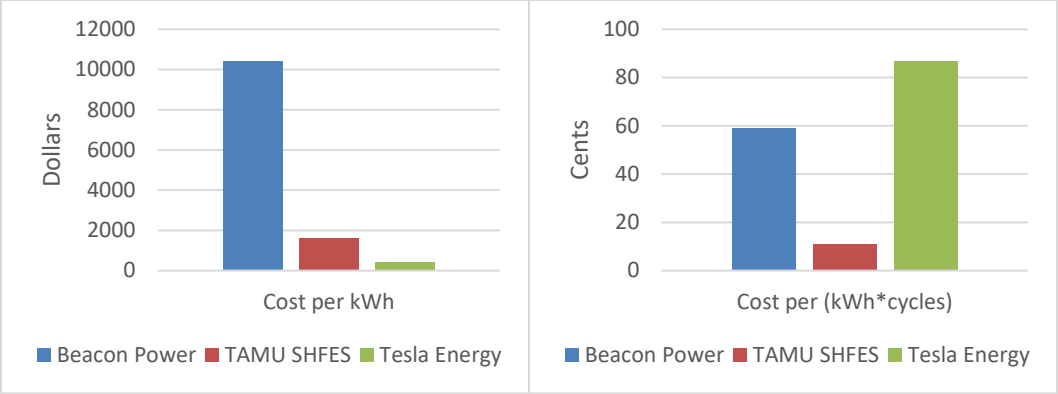

Figure 3.2 Cost Comparison Between Flywheel and Battery

TABLE 3.2 COST COMPARISON OF SHFES, COMPOSITE FLYWHEEL, AND LION BATTERIES

	Beacon Power[1]	SHFES[2]	Tesla Energy
Cost of one unit	$260K	$160K	$5.9K
Unit capacity	25KWh	100KWh	13.5KWh
Unit power	100KW	100KW	5KW
Life Cycles	175K	145K	5K
Cost per kWh	$10,400	$1600	$437
Cost per life time*energy	$0.059	$0.011	$0.0874
Cost per kW	$2600	$1600	$1180
Cost per life time*power	$0.0148	$0.0110	$0.236
Recyclability	Partial recyclable	Recyclable	Partial recyclable
Maint. & life	Low & 20yr	Low & 20yr	<< 20 yr
Environ. impact	Low	Low	Medium-High

[1]Estimated based on [43]

[2]Cost estimated based on following: rotor – 60K, power electronics for motor – 30K, motor – 10K, controller 5K, C5AMB – 15K, supporting structure - 10K, Catcher bearing – 10K, Cooling system – 5K, Vacuum enclosure and its maintenance system 15K.

CHAPTER IV

ANALYSIS AND IMPROVEMENT OF THE SHAFTLESS FLYWHEEL

Introduction

The kinetic energy (E) stored in a flywheel is simply:

$$E = \frac{1}{2} I_p \omega^2 \tag{4.1}$$

where I_p is the moment of inertia and ω is the flywheel spinning speed. To raise the energy capacity, flywheels are designed to have a higher moment of inertia and able to rotate at a higher spinning speed. However, a very high spinning speed will eventually lead to a failure caused by the stress developed by inertia load [53]. Genta [54] has laid out the foundation of flywheel design by his research of theoretical analysis of isotropic flywheels. He has introduced the following equation (4.2) that characterizes the factors that determine a flywheel's specific energy (mass based energy):

$$\frac{E}{m} = \alpha' \alpha'' \alpha''' K \frac{\sigma}{\rho} \tag{4.2}$$

in which α' is the safety factor, α'' the depth of discharge factor, α''' the ratio of rotating mass to the total system mass, σ the material's tensile strength and ρ the density. Composite materials are often chosen to make FESS flywheels for its low density and high tensile strength. Light-weight composite materials (LCFM) have a very high specific energy, which is crucial in aerospace or mobile applications. Research works in [15,55,56] have claimed very high specific energies between 50 to 100 Wh/kg. However, only the composite rim was included in the calculation. The metallic shaft, which is an essential

component and has considerable mass, is normally neglected. Other components are also not considered. One of the composite based FESS being successfully developed [14], for example, has a specific energy of 42KJ/kg which is equivalent to only 11.7Wh/kg. The specific energy drops to 5.6Wh/kg when the whole system weight is included. The cost of composite materials is significantly higher than steel too. The comparison of density, tensile strength and costs between composite and steel is summarized in Table 4.1 [53]. While Carbon T1000 may have a density only 20% of steel's and a tensile strength 26% higher than steel's. Its cost is almost 100 times more. Also notice that the maximum specific energy of T1000 is based on an ideal, pure composite flywheel. The energy capacity per dollar of composite flywheels are only a fraction of steel flywheels. From the standpoint of cost, steel based FESSs are more suitable for massive productions.

TABLE 4.1 COMPARISON OF DIFFERENT FLYWHEEL MATERIALS, REPRINTED FROM [53]

MATERIALS	DENSITY (KG/M3)	TENSILE STRENGTH (MPA)	MAX SPECIFIC ENERGY (WH/KG)	COST ($/KG)	ENERGY PER DOLLAR (WH/$)
Steel 4340	7700	1520	50	1	50
E-glass	2000	100	14	11	1.27
S2-glass	1920	1470	210	24.6	8.54
Carbon T1000	1520	1950	350	101.8	3.47
Carbon AS4C	1510	1650	300	31.3	9.59

Also, sizeable ground-based FESS applications are less reliant on system weight reduction. HSS flywheels, on the other hand, have a high energy density (volume-based

energy) due to their high mass density, therefore are very suitable for fixed, ground-based, large capacity, widespread applications. Furthermore, HSS flywheels are superior to composite ones regarding thermal conductivity and availability of design data such as SN curves, fracture toughness, etc.

FESSs are complex systems that require an integration of mechanical, magnetic and electrical systems. Specific energy determines the rotor's cost which eventually drives the overall cost of the entire FESS. Thus, the design and analysis of the rotor is usually the starting point of developing a FESS. In the remainder of this chapter, the stress distribution and specific energy of a shaftless flywheel are formulized compared with other designs. Improvement is then carried out on the current shaftless design with detailed consideration of magnetic levitation, motor and catcher bearings. Shrink-fit of a new radial ring and parametric study significantly reduce the equivalent stress induced by rotation. A new flywheel design with higher specific energy is achieved.

Stress Analysis

During the rotational motion, a flywheel is subject to both hoop (σ_θ) and radial (σ_r) stress but only has radial displacement $u(r)$. The equilibrium equation [57] of a rotating disk is given in (4.3):

$$\frac{d}{dr}(r\sigma_r) - \sigma_\theta + \rho\omega^2 r^2 = 0 \tag{4.3}$$

Failure Criteria

Von-Mises is widely used as the failure criteria:

$$\sigma_v = \sqrt{\frac{(\sigma_1 - \sigma_2)^2 + (\sigma_2 - \sigma_3)^2 + (\sigma_1 - \sigma_3)^2}{2}} = \sqrt{\sigma_r^2 + \sigma_\theta^2 - \sigma_r\sigma_\theta} \tag{4.4}$$

The solutions of (4.3) under different boundary conditions and geometries are:

1. The radial stress (σ_r) and tangential stress (σ_θ) of a rotating solid disk with external pressure imposed on the outer radius [57]:

$$\sigma_r(r) = -p_b + \frac{3+v}{8}\rho\omega^2 b^2\left[1 - \frac{r^2}{b^2}\right]$$
$$\sigma_\theta(r) = -p_b + \frac{3+v}{8}\rho\omega^2 b^2\left[1 - \left(\frac{1+3v}{3+v}\right)\frac{r^2}{b^2}\right] \tag{4.5}$$

where a, b represents the inner and outer radius of the disk, ρ the material density, ω the rotational speed and v the Poisson ratio. The equations include two terms. One compressive stress, which is caused by and proportional to external pressure p_b. The other tensile stress is proportional to $\rho\omega^2 b^2$ and caused by centrifugal force. These two components are independent of each other.

2. The radial stress and tangential stress of an annulus disk with external pressure imposed on the inner and outer radius [57]:

$$\sigma_r(r) = \overbrace{p_a \frac{t^2}{1-t^2}\left(1-\frac{b^2}{r^2}\right)}^{inner} - \overbrace{p_b \frac{1}{1-t^2}\left(1-\frac{a^2}{r^2}\right)}^{outer} + \overbrace{\frac{3+v}{8}\rho\omega^2 b^2\left[t^2+1-\frac{r^2}{b^2}-\frac{a^2}{r^2}\right]}^{rotational}$$

$$\sigma_\theta(r) = \overbrace{p_a \frac{t^2}{1-t^2}\left(1+\frac{b^2}{r^2}\right)}^{inner} - \overbrace{p_b \frac{1}{1-t^2}\left(1+\frac{a^2}{r^2}\right)}^{outer} + \overbrace{\frac{3+v}{8}\rho\omega^2 b^2\left[t^2+1-\frac{1+3v}{3+v}\left(\frac{r^2}{b^2}\right)+\frac{a^2}{r^2}\right]}^{rotational} \quad (4.6)$$

The radial stresses associated with outer and inner radius pressure are compressive, the hoop stress associated with inner radius pressure is tensile, but the hoop stress associated with outer radius pressure is compressive. The stresses are products of dimensionless factors, and the causes of stress include external pressure (p_a, p_b) or the rotational motion ($\rho\omega^2 b^2$). The dimensionless factors only depend on materials and geometries. Figure 4.1 shows how the inner radius pressure caused stresses are distributed inside the flywheel and how the ratio of inner to outer radius (t) affects the stress distributions.

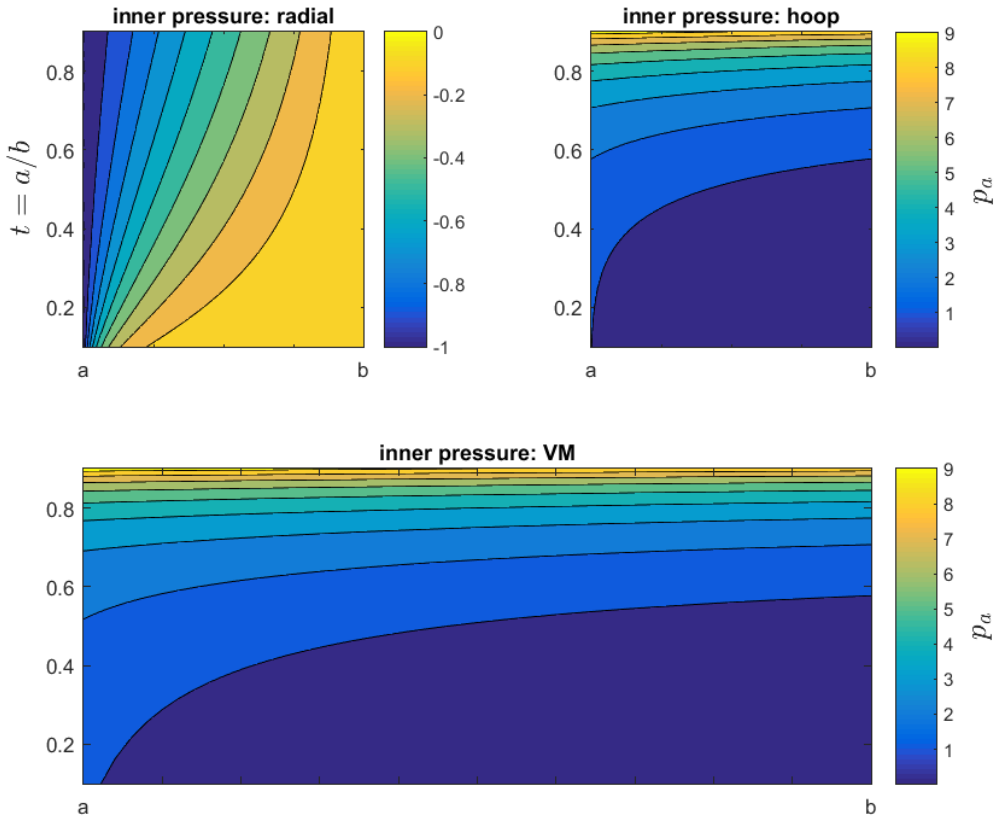

Figure 4.1 Contour Plot of Inner Radius Pressure Caused Stress

Note: Stress w.r.t. to t (inner to outer radius) and radial position (from a to b) inside an annulus flywheel.

Based on the contour plots of Figure 4.1 and Figure 4.2, the external pressure induced radial stresses, whether inner or outer pressure induced, are more sensitive to the change of radial position. In other words, the stress varies noticeably with respect to the radial position where it is evaluated. Such variation becomes more linear spread as *t* increases. However, increasing *t* itself has little effect on the magnitude or maximum value of radial stresses. On the contrary, the inner and outer pressure induced hoop stress

increase significantly when t increases, I.e. when the annulus flywheel becomes thinner, the pressure-induced hoop stress becomes more significant.

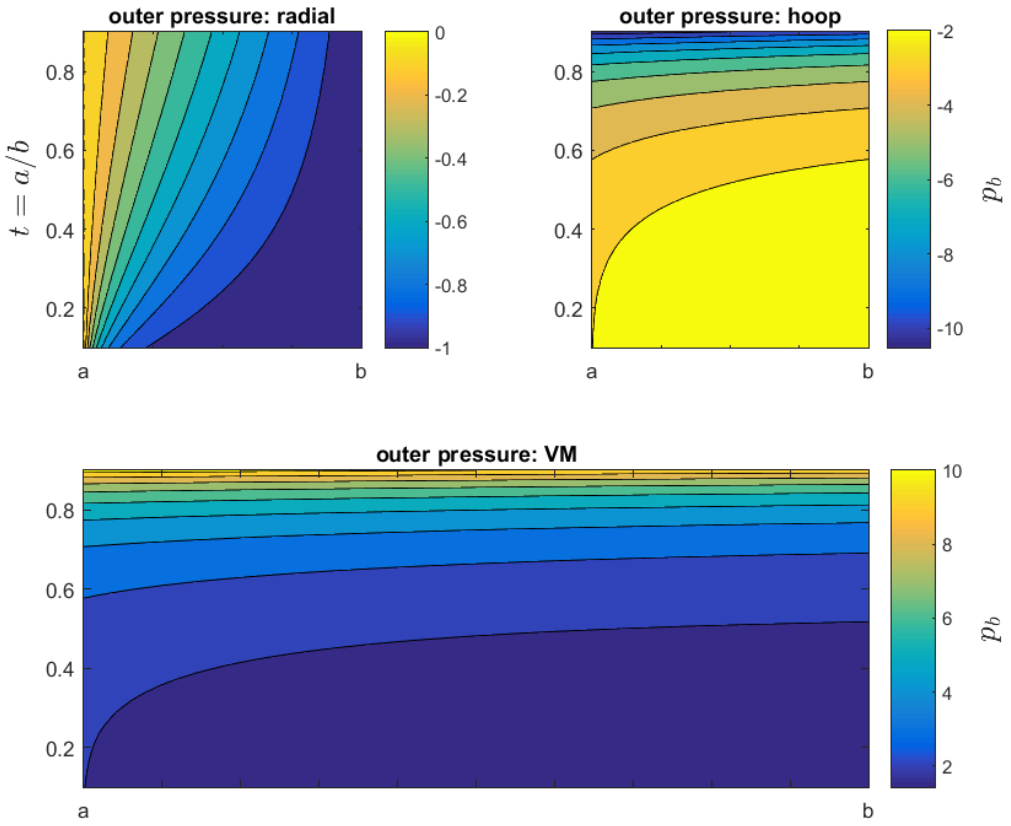

Figure 4.2 Contour Plot of Outer Radius Pressure Caused Stress
Note: Stress w.r.t. to t (inner to outer radius) and Radial Position (from a to b) Inside an Annulus Flywheel.

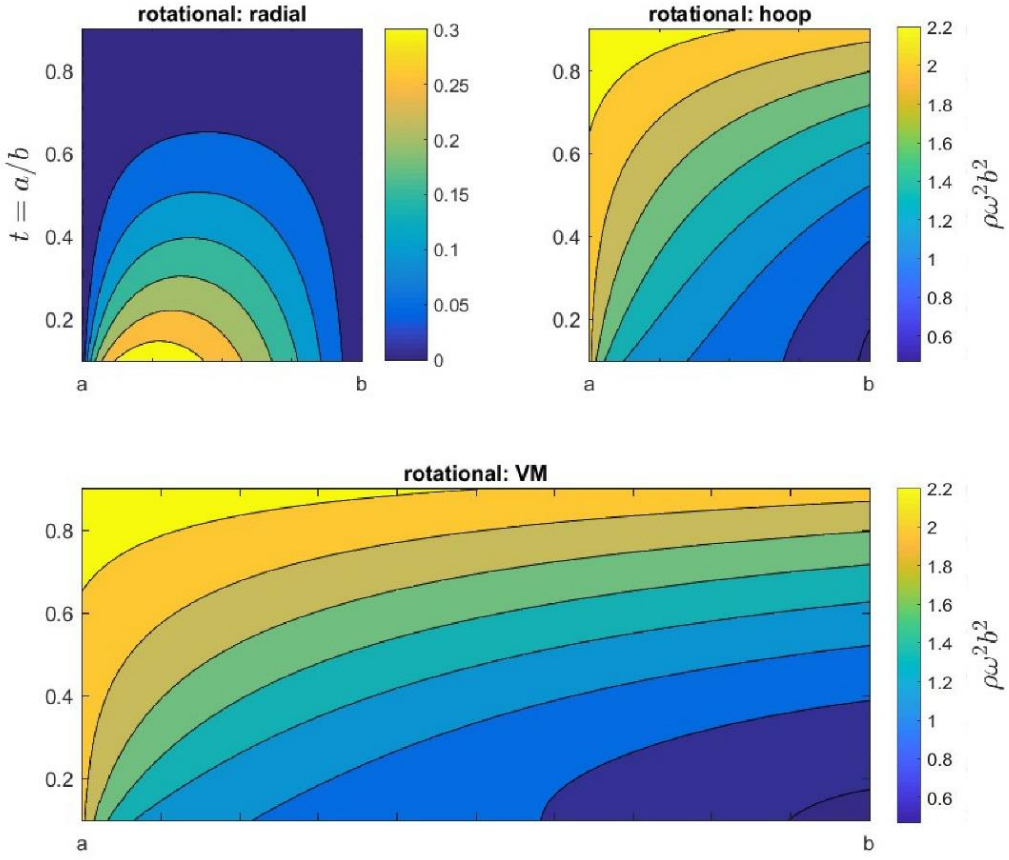

Figure 4.3 Contour Plot of Rotation Caused Stress

Note: Stress w.r.t. to t (inner to outer radius) and Radial Position (from a to b) Inside an Annulus Flywheel.

The Von-Mises stress of rotational induced stresses is given in Figure 4.3 . For the rotational radial stress, the maximum value occurs at $\sqrt{ab}$ along the radial direction. For hoop stress, the maximum value occurs at the inner radius a. As the flywheel become thinner (as t increases), radial stress decreases but hoop stress increases. For the rotation caused Von-Mises stress, hoop stress is clearly the dominating factor. Notice that the

external pressures (p_a, p_b) and rotational load ($\rho\omega^2 b^2$) are not directly comparable. To include pressure-induced stress in failure analysis. The following lemma is introduced:

Lemma: *The maximum Von-Mises (σ_{mv}) of an annulus flywheel subject to inner radius pressure and rotational load has a simplified upper boundary:*

$$\sigma_{mv}(\omega + p) \leq \sigma_{mv}(\omega) + \sigma_{mv}(p) \tag{4.7}$$

when $\sigma_{mv}(\omega)$ and $\sigma_{mv}(p)$ are the maximum Von-Mises stress of the flywheel caused by rotation and inner radius pressure independently.

Proof:

$\sigma_{max}(\omega + p)$ occurs at $r = a$ for typical cases. Notice that $\sigma_r(\omega)|_{r=a} = 0$

$$\sigma_{max}(\omega + p) = \sqrt{\sigma_r^2 + \sigma_\theta^2 - \sigma_r\sigma_\theta}\Big|_{r=a}$$
$$= \sqrt{\sigma_r^2(p) + \sigma_\theta^2(\omega) + \sigma_\theta^2(p) + 2\sigma_\theta(\omega)\sigma_\theta(p) - \sigma_r(p)\sigma_\theta(\omega) - \sigma_r(p)\sigma_\theta(p)}\Big|_{r=a} \tag{4.8}$$

Therefore:

$$\sigma_{max}(\omega + p)$$
$$= \sqrt{\sigma_{mv}^2(\omega) + \sigma_{mv}^2(p) + 2\sigma_{mv}(\omega)\left(\sigma_\theta(p) - \frac{1}{2}\sigma_r(p)\right)}\Big|_{r=a} \tag{4.9}$$

Since $\sigma_r(p) \leq 0$ and $\sigma_\theta(p) \geq 0$ for inner pressure caused stress.

$$\sigma_\theta(p) - \frac{1}{2}\sigma_r(p)\Big|_{r=a} = \sqrt{\frac{1}{4}\sigma_r^2(p) + \sigma_\theta^2(p) - \sigma_r(p)\sigma_\theta(p)}\Big|_{r=a} \leq \sqrt{\sigma_r^2(p) + \sigma_\theta^2(p) - \sigma_r(p)\sigma_\theta(p)}\Big|_{r=a} = \sigma_{mv}(p) \tag{4.10}$$

Refactoring (4.9) yields:

$$\sigma_{vm}(\omega + p) \leq \sqrt{\sigma_{mv}^2(\omega) + \sigma_{mv}^2(p) + 2\sigma_{mv}(\omega)\sigma_{mv}(p)} = \sigma_{mv}(\omega) + \sigma_{mv}(p) \tag{4.11}$$

Therefore:

$$\sigma_{mv} \leq \sigma_{mv}(\omega) + \sigma_{mv}(p) \approx C_1\omega^2 + C_2u' \tag{4.12}$$

where $C_1\ and\ C_2$ are constants related to flywheel geometry and material and u' is the shrink-fit percentage. In conclusion, if $\sigma_{mv}(\omega) + \sigma_{mv}(p)$ is within the material's tensile strength. The flywheel will not failure. In addition, $\sigma_{mv}(p)$ and $\sigma_{mv}(\omega)$ can be evaluated separately based on rotational and external pressure, which will facilitate the design process.

Shaftless Flywheel

For a solid, shaftless flywheel, the maximum radial, tangential stress occurs at the center of it. The maximum Von-Mises stress also occurs at the center of the flywheel which is equal to $\frac{3+v}{8} \times \rho\omega^2 b^2$. For a 42-inch, high strength steel shaftless flywheel, the maximum theoretical Von-Mises stress at 5000 RPM is about 145 KSI.

Annulus Disk with a Shrink-Fit Shaft

As depicted in Figure 4.4, this is a typical case where a flywheel is supported by a shaft. Most of the moment of inertia in the system is provided by the rotor while the shaft acts as an interface to the magnetic bearings and the motor/generator. The flywheel is subject to both the rotational and shrink-fit caused stress. The maximum VM stress level can be derived by (4.11).

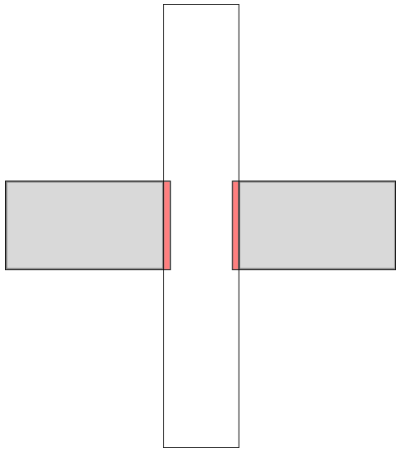

Figure 4.4 Annulus Flywheel with a Shrink-Fit Shaft

Specific Energy

The specific energy of a spinning disk depends on its moment of inertia, maximum rotating speed, and its mass.

$$\frac{E}{m} = \frac{\frac{1}{2} J \omega_{max}^2}{m} \tag{4.13}$$

Consider the angular velocity is bounded by the max stress (σ_y) that the flywheel can undertake.

$$\begin{gathered} \omega^2(solid) = \frac{8\sigma_y}{(3+v)\rho b^2} \\ \omega^2(annulus) = \frac{8\left(\sigma_y - \sigma_s\right)}{(3+v)\rho b^2}\left(\frac{1}{\kappa}\right) \\ where\ \kappa = \frac{2-2v}{3+v} t^2 + 2 \end{gathered} \tag{4.14}$$

Therefore

$$\begin{gathered} \frac{E}{m}(solid) = \frac{2\sigma_y}{(3+v)\rho} \\ \frac{E}{m}(annulus) = \frac{\left(\sigma_y - \sigma_s\right)(t^2+1)}{\rho[(1-v)t^2 + 3 + v]} \end{gathered} \tag{4.15}$$

The ratio of specific energy between a solid and an annulus flywheel is

$$\begin{gathered} \lambda_k = \frac{E}{m}(solid) \div \frac{E}{m}(annulus) \\ = \frac{2}{(1-\Delta\sigma)}\left[1 - \frac{2(1+v)t^2}{(3+v)(t^2+1)}\right] \end{gathered} \tag{4.16}$$

where $t = a/b$ denotes the ratio between inner and outer radius (equivalent to shaft-to-flywheel radius) for the annular flywheel and $\Delta\sigma$ denotes the ratio of shrink-fit-

caused stress to the material's yield stress. In the following sections, the shaftless flywheel is used as a benchmark to compare with other typical flywheel designs.

Annulus Flywheel without a Shaft (Shell Flywheel)

For this type of flywheel, the max specific energy can reach 80% of the benchmark (shaftless flywheel, see Figure 4.5). However, it can be only achieved with an inner to outer radius ratio of nearly 1, which creates a thin-wall-like flywheel and reduces its mass significantly. Making such flywheels requires extensive matching, which is a significant waste of materials. Also, such type of flywheel requires specialized MB and MG since it has no shaft.

$$\lim_{t\to 1}\frac{1}{\lambda_k}=\frac{1}{2-\frac{(2+2v)}{(3+v)}}\approx 0.825 \tag{4.17}$$

Figure 4.5 Comparison of Specific Energy: Shell vs. Shaftless Flywheel

Annulus Flywheel with a Shrink-fit Shaft

Based on the previous investigation, the shell flywheel usually fails at the inner radius of the rotor because of the lifted hoop stress. It is important to note that an annulus flywheel usually is supported by a shaft which is also rotating. The combined mass is more substantial than the mass of a solid flywheel with the same radius. Furthermore, because that the maximum spinning speed is further confined by the center hole, the specific energy is lowered even further. In addition, the stress caused by interference fit ($\Delta\sigma$) is derimental to the flywheel. Depending on the inner radius of the flywheel and the shrink-fit stress, it can be concluded that the specific energy of a solid shaftless flywheel can be 100% or higher than that of an annulus flywheel.

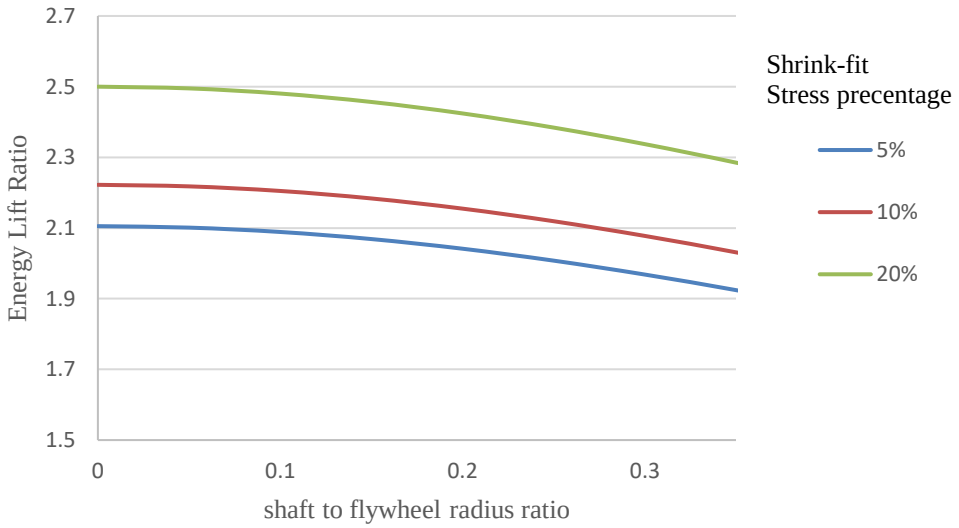

Figure 4.6 The Ratios of Specific Energy: Shaftless vs. Annulus Flywheel

Per Figure 4.6, the horizontal axis is the ratio of shaft radius to flywheel radius. The different curves are results of stresses caused by different shrink-fit allowances. In general, the shaftless flywheel will have doubled energy density. The shaftless flywheel

nearly doubles its specific energy to 18-21 Wh/kg and energy density to 138-161 kWh/m^3. Composite flywheels reportedly [3–5] have similar or higher specific energy due to their low density and higher hoop tensile stress. But they are inferior in providing competitive energy density. Furthermore, they need to be operated at a much higher speed (typically above 10,000 RPM) to provide the same energy and have a higher cost of the materials and fabrication.

Flywheel Design and Improvement

To facilitate magnetic levitation, motoring/regeneration, and drop protection, the flywheel is not a pure disk. The section view of the flywheel is given in the following figure. The upper body includes an extra rim to allow radial levitation fluxes. The lower body has a large ring attached for drop protection. At last, there is a slot machined out for installation of motor magnets.

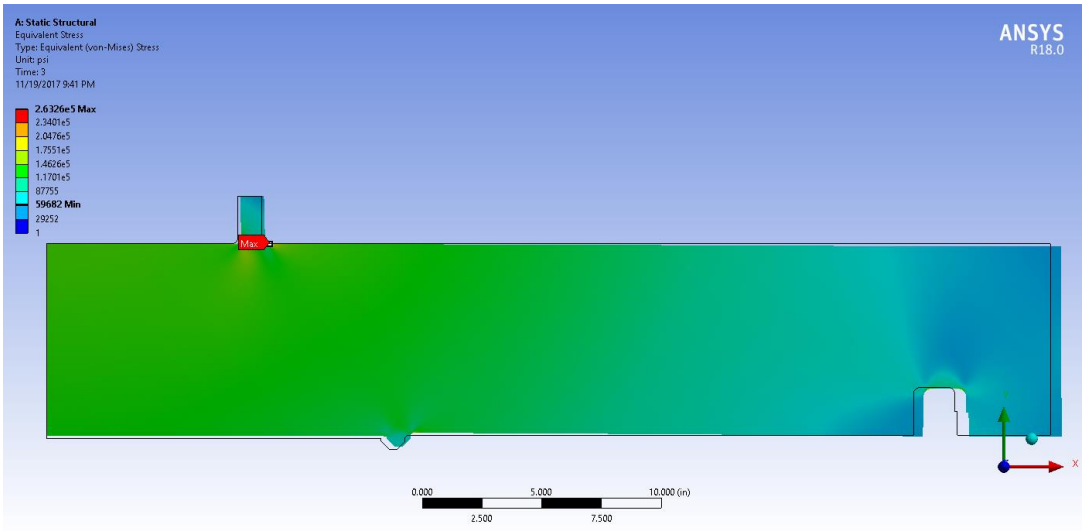

Figure 4.7 Flywheel Section View and Overall Stress Distribution

The maximum rotational velocity is determined so that the stresses within the flywheel do not exceed material's yield strength. The detailed stress analysis was carried out using commercial finite element analysis software. It was found that the max stress occurs at the interface between the flywheel's radial ring and the main body. As shown in Figure 4.7, the stress level is below the yielding strength of heat-treated 4340 stainless steel as long as the flywheel is operating below 4500 RPM. There are commercially available 4340 steel that has a yield strength of 240Ksi (1655Mpa). However, at 5000

RPM, the current flywheel design has a maximum Von-Mises of 265 KSI occurring at the outer fillet, which is approaching the yield stress (depicted in Figure 4.8).

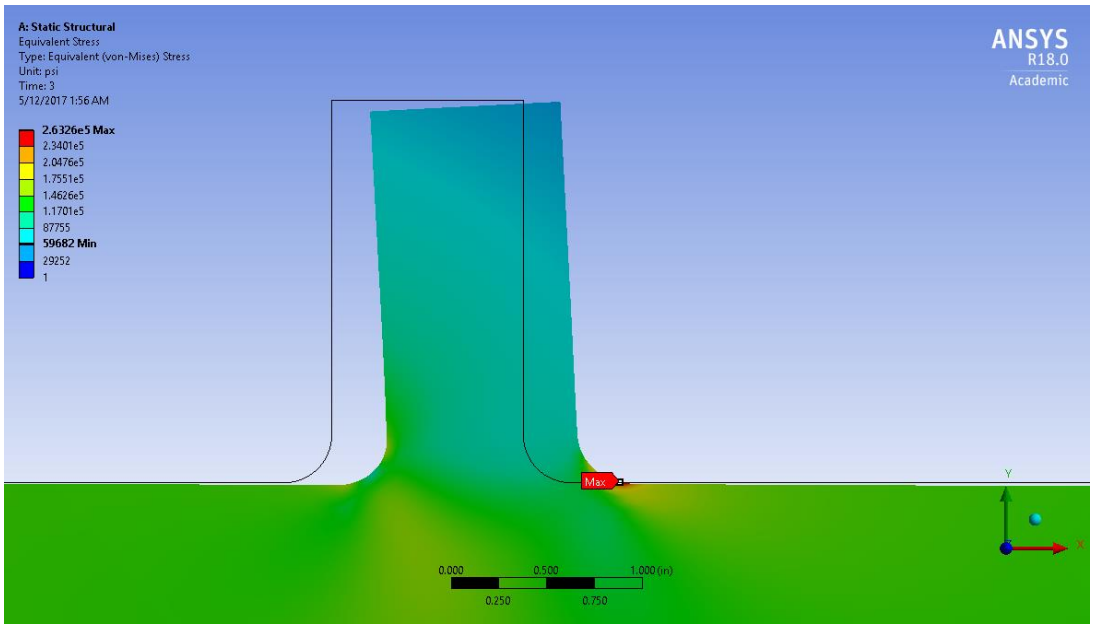

Figure 4.8 Close Look of the Stress Concentration Near the Outer Radius Fillet. Note: The deformation was amplified by 10, Notice the max VM Stress is close to 265KSI.

Flywheel Design Improvement

To achieve a higher spinning speed, the current design is improved with FEA studies and optimization searches. To ensure the new flywheel will fit the existing AMB and to alleviate the stress concentration, a shrink-fit ring is introduced for the flywheel (shown in Figure 4.9). Its thickness (Th_s) is constrained to be ($1\ inch - Th_r$). Design parameters are chosen to have minimal impact on the present magnetic bearing and motor designs. They are the fillet radius (R_r), radial ring height (H_r), radial ring thickness (Th_r) and motor slot fillet (R_m). Since the catcher bearing ridge can be moved further outside or completely removed to avoid stress concentration, it is not considered as a design parameter. The design parameters are confined by constraints:

$$\begin{gathered} 0.25\ inch < R_r < 1\ inch \\ 1.8\ inch < H_r < 2.2\ inch \\ 0.25\ inch < Th_r < 0.75\ inch \\ 0.1\ inch < R_m < 1\ inch \\ 0.001\ inch < Sh < 0.025\ inch \end{gathered} \tag{4.18}$$

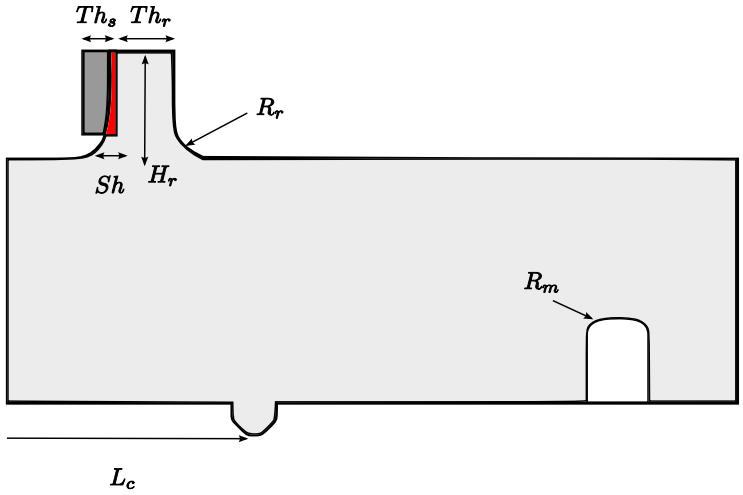

Figure 4.9 Flywheel Design Modifications and the Parameters to be Optimized
Note: (Dimension not Drawn to Scale)

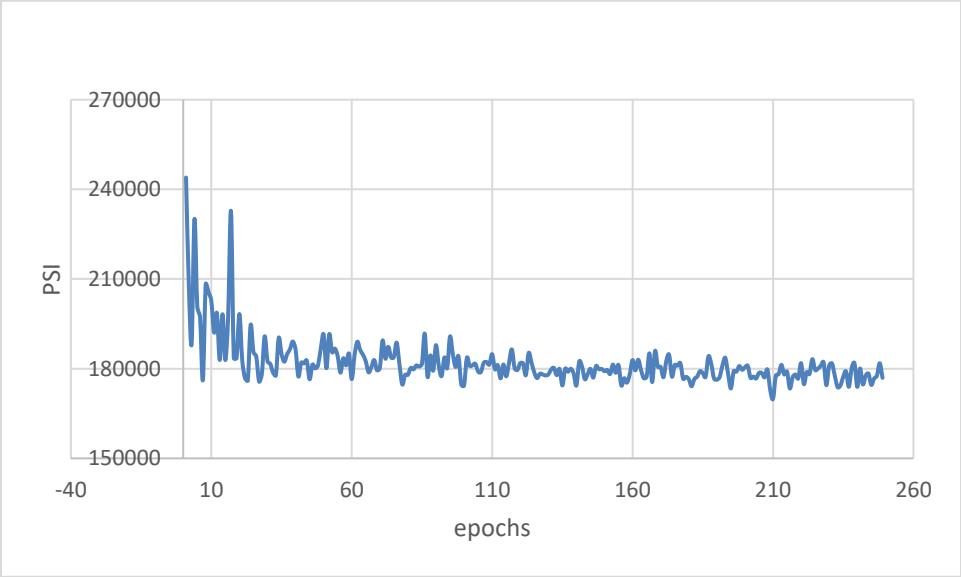

Figure 4.10 Stress Optimization Results

The optimization process utilizes the built-in adaptive single target solver. The optimization parameters are treated as continuous variables rather than manufacture-feasible variables to reduce complexity. When a satisfying result is achieved (shown in

Figure 4.10), the design parameters are rounded to manufacture-possible values and adjusted manually. The resulting design parameters are summarized in Table 4.2:

TABLE 4.2 NEW FLYWHEEL DESIGN PARAMETERS

Parameter Name	Symbol	Quantity	Unit
Outer diameter	-	2133	[mm]
Height	-	20	[mm]
Radial ring height	Hr	55	[mm]
Radial ring filler radius	Rr	22.22	[mm]
Motor slot fillet radius	Mr	10.16	[mm]
Radial Ring shrink-fit	Sh	0.5	[mm]
Radial Ring thickness	Thr	7	[mm]
Materials	-	4340	AISI
Material tensile strength	-	1500	[Mpa]
Linear relative magnetic permeability	-	200	-

The resulting improvements regarding maximum speed and energy capacity are summarized in Table 4.3. As depicted in Figure 4.11, the stress concentration is alleviated.

TABLE 4.3 IMPROVED FLYWHEEL SPECIFICATIONS

Parameter Name	Quantity	Unit	Improvement to	
			Design target	Current design
Mass	5443	[kg]	-	
Moment of inertia	3087	[kg·m^2]	-	
Max rotational speed	5750	[rpm]	15%	28%
Tip speed	642	[m/s]	15%	28%
Max Energy	155	[kWh]	32.25%	63%
Operational Energy	132	[kWh]	32.25%	63%
Power capacity	100	[kw]	-	

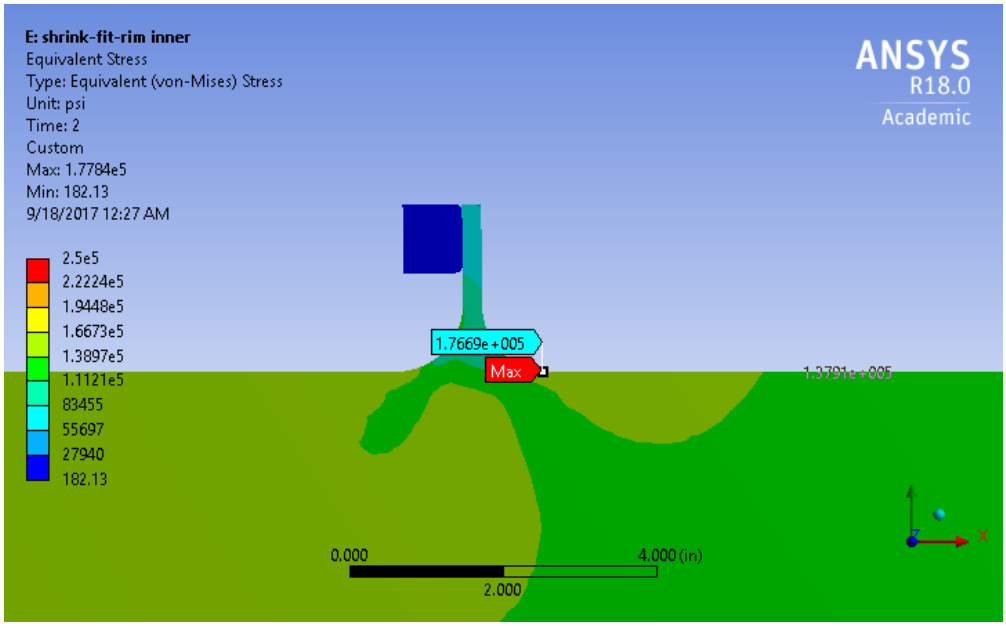

Figure 4.11 A Close Look at the Improved Stress Distribution near the Radial Ring

Eddy Current Brake Design

A preliminary eddy current braking system is designed for slowing down the flywheel and dissipate much of the stored energy in case of system failure. As depicted in Figure 4.12, a single brake is designed to have two permanent magnets, which are installed vertically facing the flywheel with opposing magnetic orientation. A back-iron help closing the magnetic circuit. The preliminary design considers four brakes.

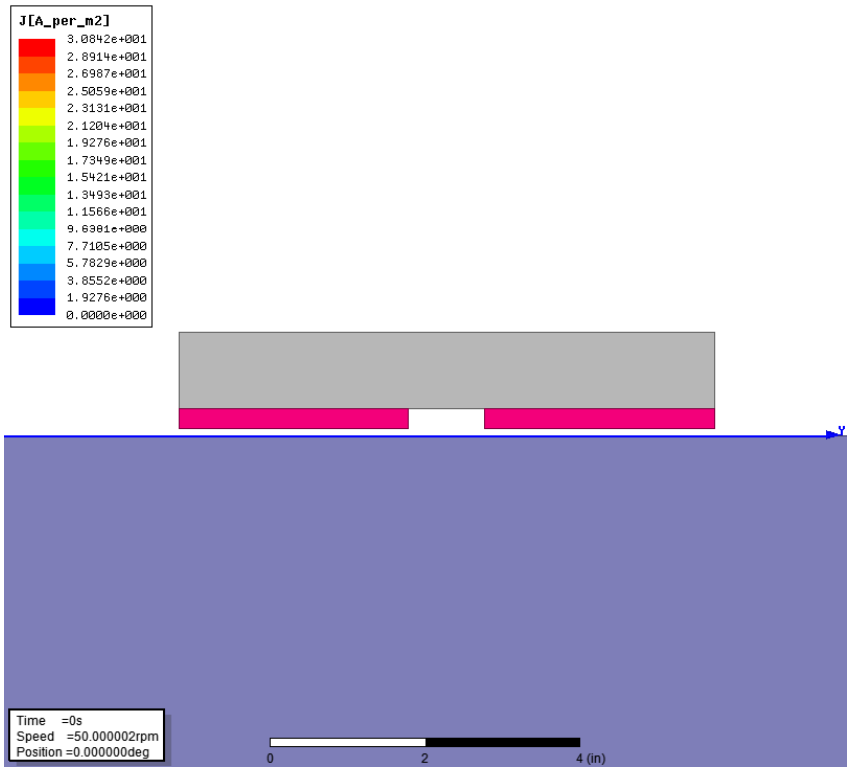

Figure 4.12 The Eddy Current Brake Design
Note: Magnets (red), Back-iron(gray) and the Flywheel (light purple)

The eddy current brake is simulated by a commercial FEA software. Its performance and design parameters are summarized in Table 4.4 and Table 4.5. Due to the reason of limited computation power, it is difficult to evaluate the eddy current brake's performance at high speed.

TABLE 4.4 EDDY CURRENT BRAKING POWER

Spinning speed	Drag torque	Power loss
10 RPM	-22 NM	-23 W
50 RPM	-67 NM	-350W
100 RPM	-82.5 NM	-865 w
500 RPM	-100NM	-5.2 kW
1000 RPM	-215 NM	-22.5 kW

TABLE 4.5 EDDY CURRENT BRAKE DESIGN PARAMETERS

Parameters	dimension	unit
Magnet size	3X4	inch
Back-iron size	4X7	inch
Magnet Thickness	0.25	inch
airgap	0.1	inch
Magnet grade	N48	~

Flywheel Thermal Analysis

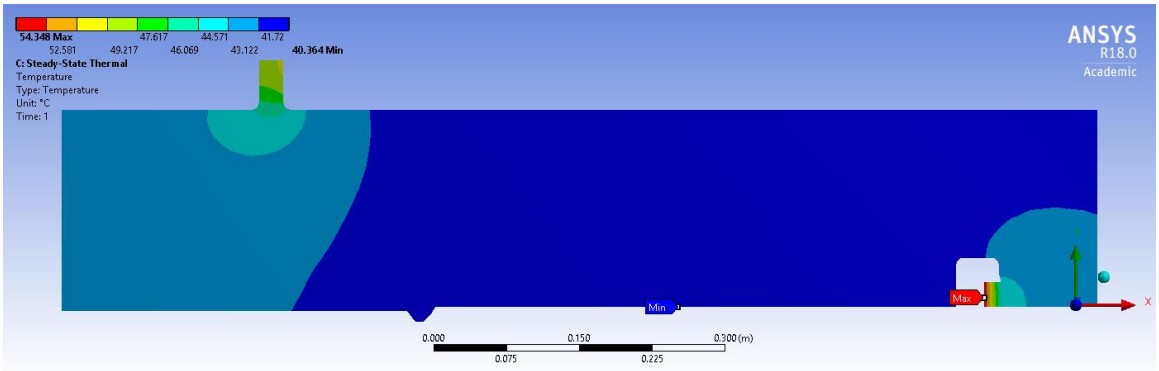

Figure 4.13 Static Analysis of the Vacuum-Enclosed Flywheel Subjected to Motor and Magnetic Bearing Losses.

The PM motor/generator for the flywheel is presented in [51]. Since the system operates in a vacuum chamber, it brings up a concern of heat dissipation. For the flywheel, which is being magnetic levitated without any physical contact and rotating in a vacuum space, there is no convective dissipation. In the meantime, heat generated by copper loss does not transfer from the coils to the magnets and rotor. Hence, eddy current is the only significant source that generates heat, whereas radiation is the only mean of heat dissipation. The employing of a large rotor reduces the opportunity of localized heat concentrations. Nevertheless, the steady-state temperature of the flywheel is investigated. An axial-symmetric model is used for static thermal FEA of the flywheel and motor magnets (see Figure 4.13). The boundary conditions are set to radiation only. According to the loss estimations, the highest MG-related power loss is about 825W. In addition to the motor loss, relative rotational motion between the flywheel and AMB also brings eddy current loss. It was estimated by [23] that the AMB-related loss is around 315W at 5000 RPM. When the flywheel reaches a surface emissivity of 0.9, the steady-state magnet

temperature does not exceed 56 Celsius, which is well below the max operating temperature for N48 neodymium magnets. Under such temperature, its thermal expansion is also not significant. The maximum and minimum temperatures under different emissivity are summarized in Table 4.6.

TABLE 4.6 THE FLYWHEEL'S STEADY-STATE TEMPERATURE IN THE VACUUM CHAMBER

Initial Temperature (Celsius)	*Minimal Temperature (Celsius)*	*Maximum Temperature (Celsius)*	*Flywheel Emissivity*
22	40.36	54.35	0.95
22	42.65	55.25	0.9
22	44.82	57.32	0.8
22	50.98	63.17	0.6

CHAPTER V

DESIGN AND ANALYSIS OF THE COMBINATION MAGNETIC BEARING

Introduction

Active Magnetic Bearings (AMB) have many advantages over conventional bearings. They require low maintenance costs and produce low pollution by eliminating the lubrication system, which is a necessity for fluid-film bearings. At the same time, AMBs offer no friction loss and much higher operational spinning speeds [58] because of the nature of magnetic levitation. Magnetic bearings have been increasingly used in industrial applications such as compressors, pumps, turbine generators and flywheel energy storage system.

This chapter presents a combination, 5-degree-of-freedom, active magnetic bearing (C5AMB) system that is designed for supporting the shaftless energy storage flywheel. Due to the nature of its design, traditional magnetic bearing systems, which requires magnetic flux path through the shaft, are not applicable to the SHFES. A novel PM biased magnetic bearing is designed to serve this purpose. The remainder of this chapter is organized as follows: The design, working principle, and modeling of the C5AMB are presented at first. Secondly, EMCM is used to analyze the force/moment to position and current relations, which are compared with FEM simulations. The coupling effects between magnetic poles are also discussed. The last section of this chapter discusses the frequency responses of the C5AMB.

Lumped Element Magnetic Bearing Modeling

The Maxwell's equations govern electrodynamics. For a static, lumped element problem without considering inductions:

$$\oint H \cdot dl = NI \rightarrow \sum H\,\Delta l = NI$$
$$\oiint B\,dA = 0 \rightarrow \sum \phi = 0 \tag{5.1}$$

The Magneto-motive force is defined as

$$mmf = \int H \cdot dl \tag{5.2}$$

The Magnetic flux is defined as

$$\phi = \int B\,dA \tag{5.3}$$

The magnetic reluctance is defined by (symbol R will be used in the later context for convenience)

$$\Re = \frac{mmf}{\phi} \tag{5.4}$$

The magnetic permeability is defined by

$$\mu = \frac{B}{H} \tag{5.5}$$

The reluctance of the air gap can be derived:

$$R_g = \frac{mmf}{\phi} = \frac{Hg}{B_g A} = \frac{g}{\mu_0 A} \tag{5.6}$$

where μ_0 is the permeability of free space. The magnetic force generated in the air gap can be derived by the virtual work method, consider that most of the energy is stored in the air gap.

$$W = \frac{1}{2}\int BHdv = \frac{1}{2\mu_0}\int B^2 dv = \frac{1}{2\mu_0}\int ({B_g}^2 A)dl$$

$$f = \frac{dW}{dl} = \frac{A}{2\mu_0}B_g^2 \tag{5.7}$$

$$df = \frac{1}{2\mu_0}B^2 dA = \frac{1}{2\mu_0}\left(\frac{F\mu_0}{g}\right)^2 dA = \frac{\mu_0}{2}\left(\frac{F}{g}\right)^2 dA$$

The attraction force is normal to the pole surface. Typically, the magnetic force can be contributed to flux provided by permanent magnets or by excitation currents:

$$f = \frac{A}{2\mu_0}\left(B_g^{pm} + B_g^i\right)^2$$

Linearization of the magnetic force yields:

$$\mathrm{f} = \overbrace{\frac{A}{\mu_0}\left(B_g^{pm}\right)|\Delta B_g^{pm}}^{PM\ force} + \overbrace{\frac{A}{\mu_0}\left(B_g^{pm}\right)|\Delta B_g^{i}}^{EM\ force} \tag{5.8}$$

Design of the C5AMB

Energy Storage flywheels are typically supported by active magnetic bearings to avoid mechanical friction loss. A convention FESS includes several magnetic bearings installed at different locations along the shaft for radial and axial levitation correspondingly. Typically, two sets of radial AMBs are responsible for controlling the radial and tilting motions of the flywheel while thrust bearings are used for axial motion control solely. The elimination of multiple actuators will simplify the system, reduce overall costs and potentially improve rotor-dynamics and control performances. Several combination designs have been proposed with different focuses. Among one of the early works, Mcmullen [59] includes the design of five-axis, two bearing system for a 42,000 RPM flywheel. In [60], a combined radial-axial is magnetic bearing is optimized with multiple objectives to improve its performance. A combined radial-axial magnetic bearing for a 1kw, 500,000 rpm machine is presented in [61]. In [62], a PM-biased axial hybrid magnetic bearing is presented. It has four segments of poles to control 3-DOF. S. Jinji et al. [19] proposed a 4-DOF magnetic bearing for capable of two radial and two radial tilting controls. In [63], a radial hybrid MB is proposed to replace the thrust bearing with axial passive resilience. Apart from combination designs, tapered magnetic bearings can provide radial and axial control at the same time [64–67] as well.

As discussed previously, the new flywheel design has eliminated the shaft. Traditional AMBs are not applicable to the SHFES. The proposed novel combination magnetic bearing is introduced to accommodate the shaftless design and reduce system complexity and costs. Its half-section view is depicted in Figure 5.1. The C5AMB's

dimension and materials are refined by intensive nonlinear 3D Finite Element Electromagnetic Analysis using commercial FEA software. It was found that low carbon steel with proper heat treatment will result in satisfying saturation flux density (B_s) and relative permeability (μ_r). With a sufficient magnetic property, it also beats electrical steels in price and availability. Apart from its magnetic properties, the C5AMB is also designed to have la ower weight in the effort of increasing the stator structure's stiffness to facilitate the feedback control. Although low frequency modes from the stator structure can be compensated by derivative feedback, it is desirable to use lthe ess derivative term as possible, for high derivative will in return magnify high frequency resonance.

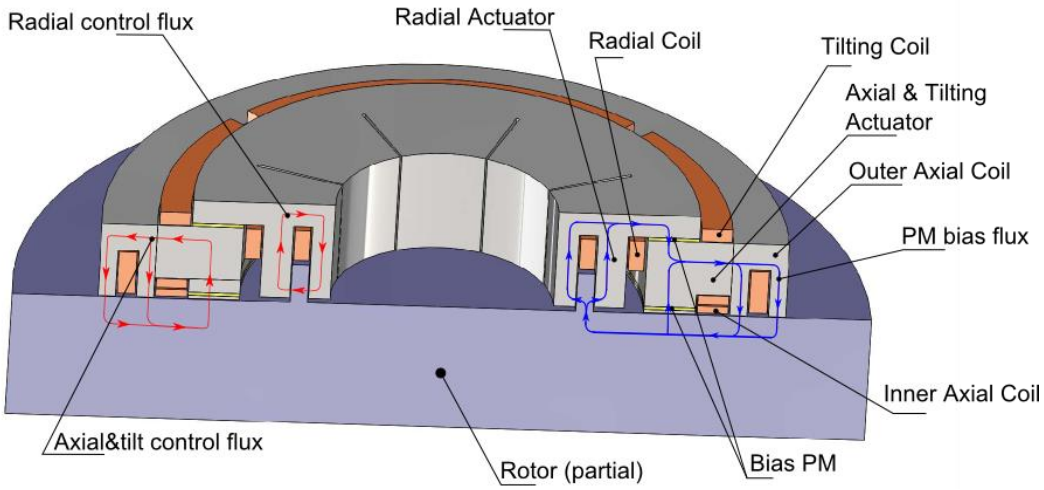

Figure 5.1 Section View of the Full C5AMB

As depicted in Figure 5.1, the permanent magnets are colored in bright yellow; coils are colored in orange. For better illustration, the flywheel is truncated radially without affecting the magnetic flux paths. For the same reason, the PM bias flux path is only highlighted in the right half of the section, and the EM flux paths are only highlighted

in the left half. Be noted that there are eight radial control coils, four tilting control coils, and two axial control coils. The combination magnetic bearing includes two major parts:

- *Radial part*: the inner circular part with radial poles attached to it. There are eight radial sub-actuators, each of which includes two poles, a flywheel ring is inserted into these poles to complete the radial flux paths.
- *Axial/tilting part*: The outer circular part with axial and PM poles. There are four segmented ring-shaped poles and two large circular ring-shaped poles. These poles are shared by the tilting and axial actuators.

The magnetic bearing is permanent-magnets-biased to provide load force for holding the flywheel's weight at the equilibrium position. Therefore, there is no need for bias current and the system energy consumption is reduced. Another benefit of PM-bias design is alleviated eddy current effects on the rotor/flywheel. If the radial poles of the AMB are not biased, magnetic fields of different polarities need to be applied to generate a net radial force along a specific axis. When the flywheel is spinning, its radial ring will travel through magnetic fields with alternating polarities, which induces eddy current. In a PM-biased AMB, the flywheel suffers less from eddy currents by traveling through magnetic fields with varying flux density but the same polarity. The bias flux is provided by two sets of magnetic rings. One of them is installed between the radial part and the axial/tilting part. The 1st PM ring also serves as a joint between the two. The other PM

ring is installed underneath the PM poles. Two sets of PM rings are used instead of one because of the following considerations:

- Adequate axial bias flux to support the 12000 lbs flywheel at the target air gap, while providing decent radial bias flux at the same time.
- Bias flux is evenly distributed without local saturation effect that may be caused by a single dominant PM ring.
- Magnets have high reluctance to provide barriers between the axial and radial flux paths so that there is less flux leakage between them.

For radial flux paths, a single pair of two radial poles is designed to have the same bias flux density so that the net radial force is zero when the flywheel is centered and no radial excitation current is applied. On the other hand, flux circulation generated by the radial currents strengthens one of the radial poles and weakens the other one, resulting in a net radial force. The outer portion of the C5AMB provides axial and moment control. There are four tilting coils in total. Each can vary the flux in its own quadrant. Moment control is realized by giving excitation current to one tilting coil, and giving the same amount of current with reversed direction, to the opposite tilting coil w.r.t the moment axis, so that no axial force is generated. For axial control, two large ring-shaped axial coils are installed for varying the flux strength throughout the entire axial flux paths to provide vertical forces without generating any moment. The two main bodies are depicted in Figure 5.2 and Figure 5.3.

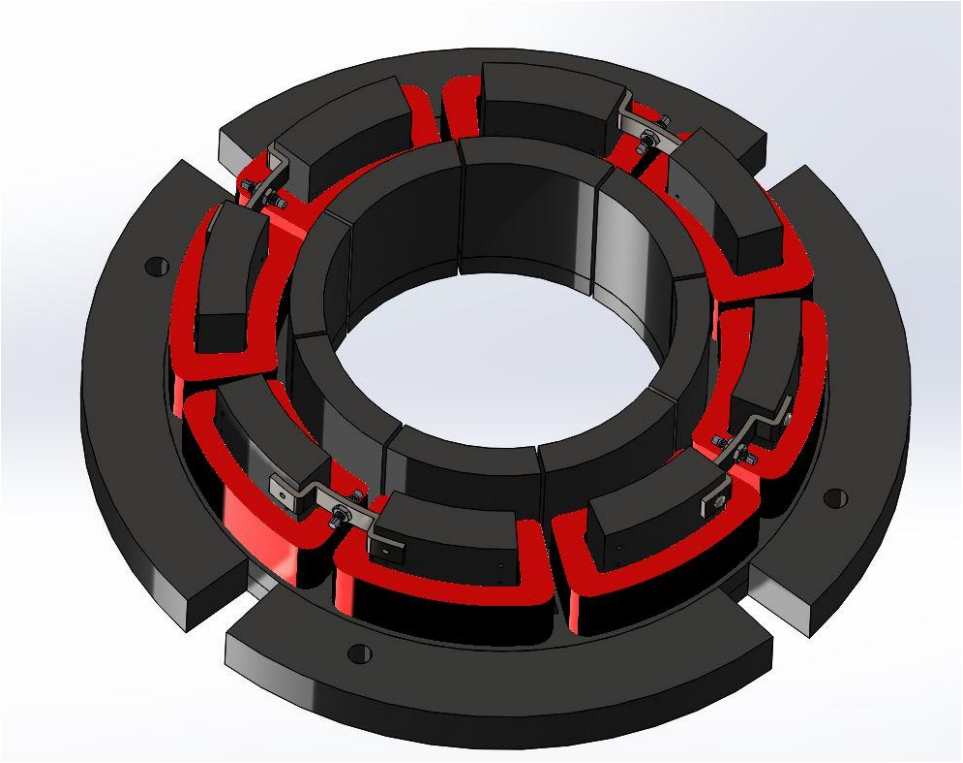

Figure 5.2 Inner Part of C5AMB

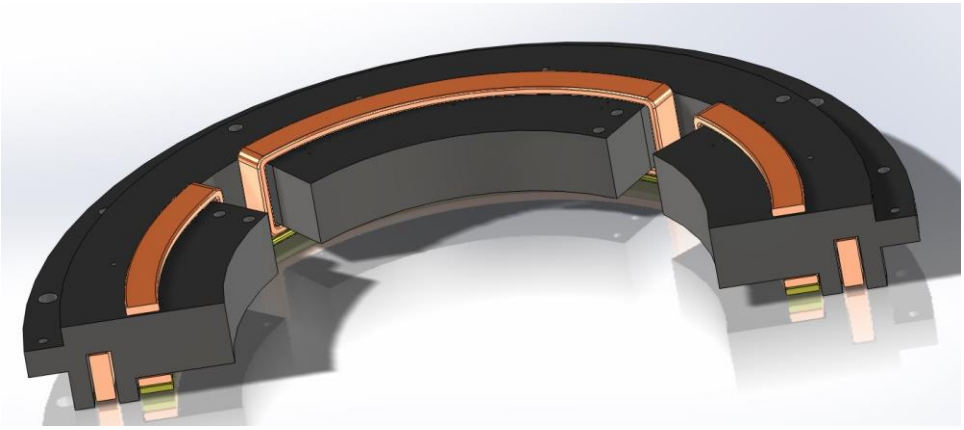

Figure 5.3 Configuration of the PM Poles

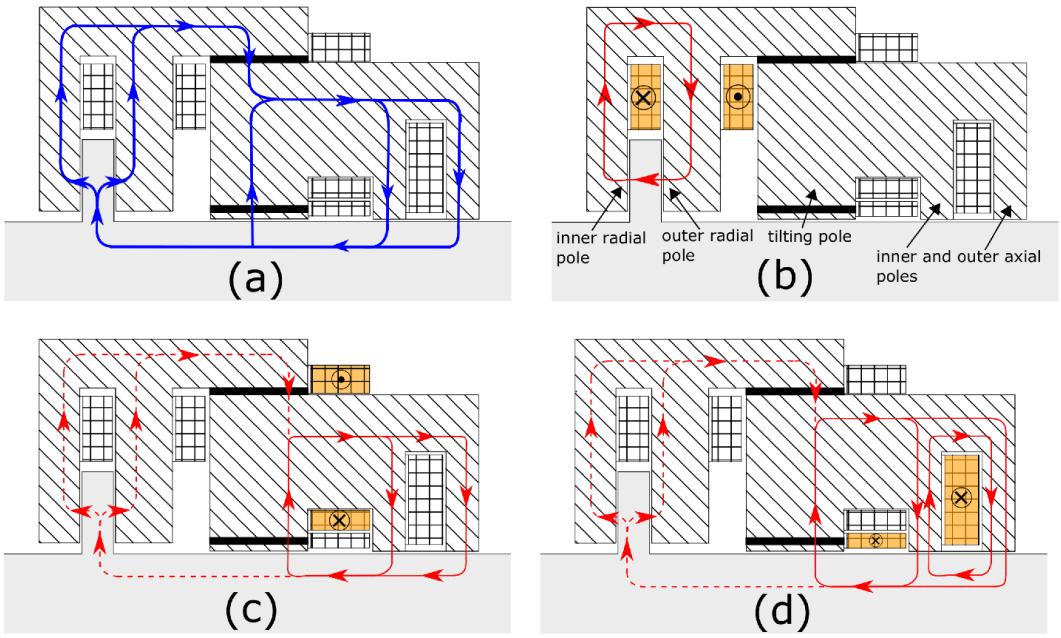

Figure 5.4 Radial Section View of Flux Paths

Note: (a) Bias flux path (b) Radial Control Flux (c) Tilting Control Flux (d) Axial Control Flux

The bias flux and electromagnetic paths are depicted in Figure 5.4. The two sets of rings (colored as solid black) are placed against each other magnetically. They provide bias fluxes for radial, tilt and axial poles at the same time (depicted in Figure 5.4. (a), colored in blue). The inner part of the C5AMB provides radial levitation. The bias flux travels through the flywheel radial ridge and evenly diverge to the inner and outer poles.

Equivalent Magnetic Circuit Modeling

As illustrated in Figure 5.5, a simple axial-symmetric equivalent-magnetic-circuit-model (EMCM) is used for modeling the bias flux distribution. This model is also used for deriving the axial control flux and serves as a foundation for the later context of PM and EM analysis of the C5AMB. The fluxes at the air gaps are defined as follows: flux at PM pole air gap (ϕ_t), flux at inner axial pole air gap (ϕ_{a1}), flux at outer axial pole air gap (ϕ_{a2}), flux at inner radial air gap (ϕ_{ri}) and flux at the outer radial pole (ϕ_{ro}). The combined flux of axial poles and radial poles are denoted as ϕ_a^{pm} and ϕ_r^{pm} accordingly. To reduce design complexity, axial pole a_1 and outer axial pole a_2 are set to have similar reluctances and pole surface areas. The solution of the axial symmetric bias magnetic circuit is given in (5.11):

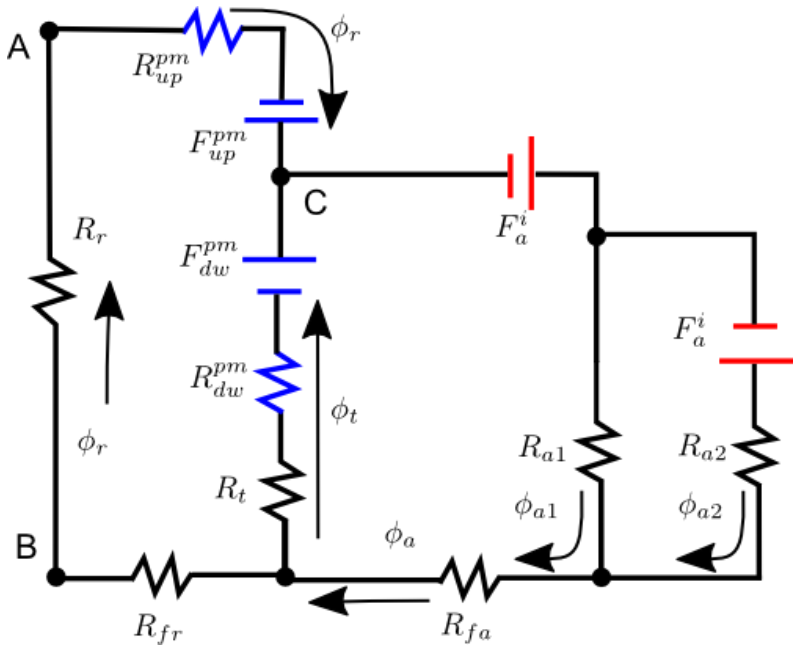

Figure 5.5 The Axial-symmetric EMCM Including PM and Axial EM MMF

Conservation of flux:

$$\phi_t^{pm} + \phi_r^{pm} - \phi_a^{pm} = 0 \tag{5.9}$$

Conservation of magneto-motive force:

$$\begin{aligned} \phi_a^{pm}(\overbrace{R_a + R_{fa}}^{\alpha}) + \phi_t^{pm}(\overbrace{R_{dw}^{pm} + R_t}^{\beta}) - F_{dw}^{pm} = 0 \\ \phi_r^{pm}(\overbrace{R_r + R_{up}^{pm} + R_{fr}}^{\gamma}) - F_{up}^{pm} + F_{dw}^{pm} - \phi_t^{pm}\left(R_{dw}^{pm} + R_t\right) = 0 \end{aligned} \tag{5.10}$$

where $\phi_a^{pm} = \phi_{a1}^{pm} + \phi_{a2}^{pm}$ and $\phi_r^{pm} = \phi_{r,pm}^{out} + \phi_{r,pm}^{in}$ are the combined PM-bias flux at axial and radial poles. The solution is:

$$\begin{aligned} \phi_a^{pm} &= \frac{1}{L}\left[\gamma F_{dw}^{pm} + \beta F_{up}^{pm}\right] \\ \phi_t^{pm} &= \frac{1}{L}\left[\alpha(F_{dw}^{pm} - F_{up}^{pm}) + \gamma F_{dw}^{pm}\right] \\ \phi_r^{pm} &= \frac{1}{L}\left[\alpha\left(F_{up}^{pm} - F_{dw}^{pm}\right) + \beta F_{up}^{pm}\right] \end{aligned} \tag{5.11}$$

in which F_{up}^{pm} and F_{dw}^{pm} are the total MMF of the top and bottom permanent magnets respectively. Further defined in (5.12) , $\alpha, \beta \; and \; \gamma$ are the parameters derived based on the equivalent magnetic reluctances of axial (R_a), PM (R_t) and radial pole (R_r). The magnetic bearing itself is made of material with a higher permeability and working below its saturation point so that its reluctance can be ignored in the lumped element model. The flywheel is made of high strength steel with lower permeability and designed to work at a flux density that is closer to its saturation point. Its reluctance must be considered. They have little variation respect to EM or flywheel's motion. They are also not design

parameters for the C5AMB, the flywheel's total equivalent reluctances (R_{fa} and R_{fr}) are estimated by the dimensions first adjusted by initial FEA simulation. The variables are highlighted in Eq. (5.10) are defined as following:

$$\begin{gathered} L = \alpha\beta + \beta\gamma + \gamma\alpha \\ \alpha = R_a + R_{fa} \\ \beta = R_t + R_{dw} \\ \gamma = R_r + R_{up} + R_{fr} \end{gathered} \tag{5.12}$$

From eq.(5.11), it can be concluded that the increase of the top magnets coercive force F_{up}^{pm} or decrease of the bottom magnets coercive force F_{dw}^{pm} will lead to a stronger radial pole bias flux ϕ_r^{pm} but a weaker PM pole bias flux ϕ_t^{pm}. Either way, the axial pole flux density can benefit from both PM rings. The effects of different permanent magnets thickness on bias flux densities are depicted in Figure 5.6. Because that the bias flux density has a direct influence on magnetic actuator's position and current stiffness. The current/position stiffness can be adjusted by choosing different thickness or materials of the PM rings, which results in different bias flux density. In addition, reluctance parameters α, β, γ are functions of the airgaps, which are eventually functions of the flywheel's translational and rotational positions. It must be noted that the radial flux between inner and outer poles are equal only when they have same reluctances, which is often hard to be achieved. Nevertheless, bias flux difference caused by design or machining will not generate a net radial force as long as radial poles are axial-symmetrical and the rotor is placed at the center of the CAMB.

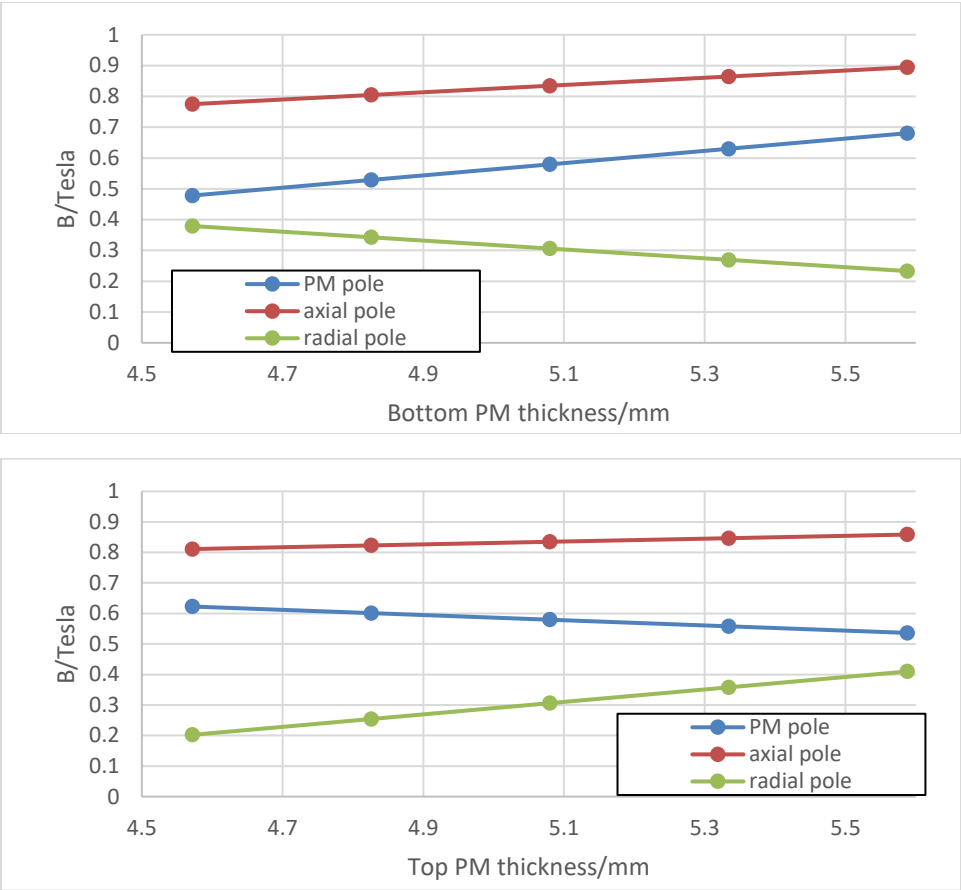

Figure 5.6 PM Bias Flux Density Change w.r.t. Bottom and Top Magnet Thickness

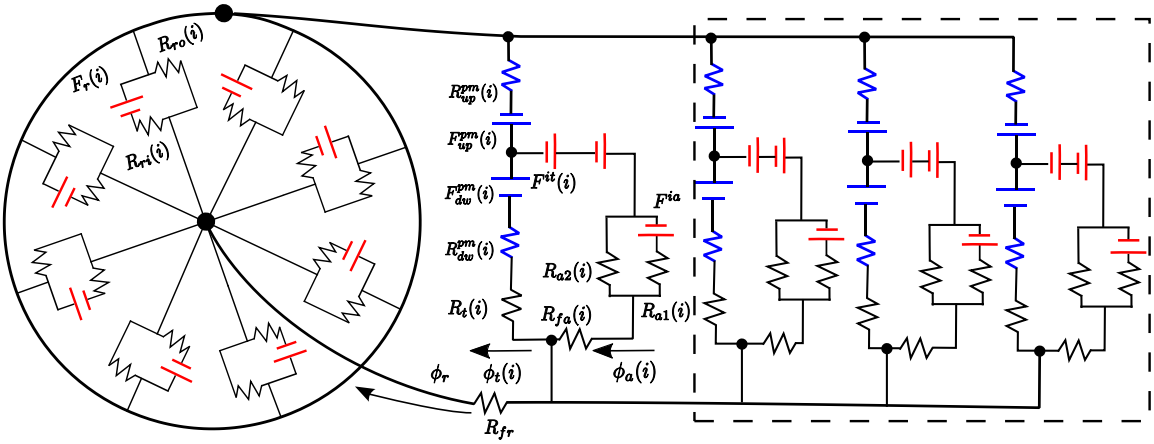

Figure 5.7 The 3D EMCM for C5AMB including PM and EM MMFs

Due to the large dimension of the MB and the relatively small air gaps. Modeling and simulation using FEM methods require significant computational power and time. With regret, there is no access to supercomputing. Therefore, an EMCM is developed for design and analyzing the C5AMB. FEM is then carried out for verification and fine-tuning purpose. As depicted in Figure 5.7, modeling of the 3D EMCM circuit consists of four axial poles, each of which has two sets of permanent magnets. Reluctance parameters are functions of the air gaps, which are eventually determined by the flywheel's transnational and rotational position. The radial ($R_r(j)$), tilt ($R_t(i)$) and axial ($R_{a1}(i)$, $R_{a2}(i)$) reluctances are given in (5.13). The reluctances of the axial and PM poles are derived using surface integral in the polar coordinate because that the air gap $g(i)$ is not constant across the pole surface:

$$
\begin{aligned}
R_r(j) &= \frac{z_1 + g_r(j)}{\mu_0 A_r(j)} \\
R_t(i) &= \frac{1}{\Lambda_t(i)} = \frac{1}{\iint \frac{\mu_0}{z_0 + g_t(i)} r dr d\phi} \\
R_{a1}(i) &= \frac{1}{\Lambda_{a1}(i)} = \frac{1}{\iint \frac{\mu_0}{z_0 + g_{a1}(i)} r dr d\phi} \\
R_{a2}(i) &= \frac{1}{\Lambda_{a2}(i)} = \frac{1}{\iint \frac{\mu_0}{z_0 + g_{a2}(i)} r dr d\phi}
\end{aligned}
\tag{5.13}
$$

Where z_0 and z_1 are the airgaps caused by axial and radial translations of the flywheel. $i = 1, \dots, 4$ and $j = 1, \dots, 8$ are the enumerations for the axial quadrants and radial pole pairs. $g(i)$ is the airgap change caused by small attitude changes of the flywheel. It is further defined in (5.14):

$$
g(r, \psi) = v'_z = r\left[\sin\theta_x sin\psi - sin\theta_y cos\psi\right] \tag{5.14}
$$

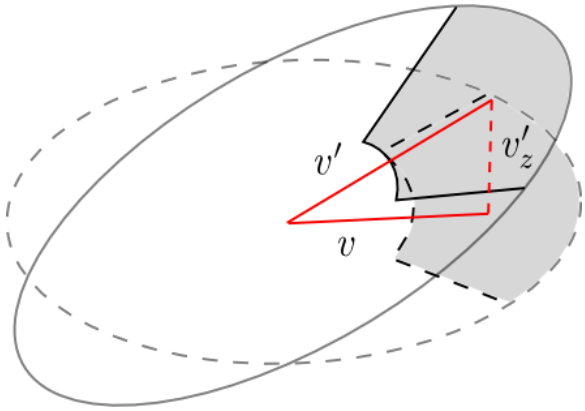

Figure 5.8 Axial Airgap Caused by Tilting Motion

In which θ_x, θ_y are the x-axis and y-axis tilting angle of the flywheel respectively (see Figure 5.8).

The radial air gaps $g_r(j)$ for each pole is determined by the flywheel's radial position relative to the C5AMB (x, y). For the outer radial poles, the reluctance is given by:

$$\boldsymbol{g}_r \approx \begin{bmatrix} g_0 - .92x - .38y \\ g_0 - .92x + .38y \\ g_0 - .38x + .92y \\ g_0 + .38x + .92y \\ g_0 + .92x + .38y \\ g_0 + .92x - .38y \\ g_0 + .38x - .92y \\ g_0 - .38x - .92y \end{bmatrix} \tag{5.15}$$

Based on the Ampere's law and conservation of flux, the 3D EMCM is described by the following set of equations:

$$\begin{gathered} \phi_a^{pm}(i)\alpha(i) + \phi_t^{pm}(i)\beta(i) = F_{dw}^{pm}(i) \\ \left(R_r + R_{fr}\right)\phi_r^{pm} + \left[\phi_a^{pm}(i) - \phi_t^{pm}(i)\right]R_{up}^{pm}(i) + \phi_a^{pm}(i)\alpha(i) = F_{up}^{pm}(i) \end{gathered} \tag{5.16}$$

Solving the following 8 by 8 equations given in the following equation gives the axial and tilt flux vector $(\boldsymbol{\Phi}_a, \boldsymbol{\Phi}_t)$:

$$\begin{gathered} \begin{bmatrix} \boldsymbol{\alpha} & \boldsymbol{\beta} \\ \boldsymbol{\alpha} + \boldsymbol{R}_{up}^{pm} + \boldsymbol{J}_4\left(R_r + R_{fr}\right) & -\boldsymbol{R}_{up}^{pm} - \boldsymbol{J}_4\left(R_r + R_{fr}\right) \end{bmatrix} \begin{bmatrix} \boldsymbol{\Phi}_{\mathrm{a}} \\ \boldsymbol{\Phi}_t \end{bmatrix} = \begin{bmatrix} \mathbf{F}_{\mathrm{dw}}^{pm} \\ \mathbf{F}_{up}^{pm} \end{bmatrix} \\ \phi_r^{pm} = [\boldsymbol{\Phi}_{\mathrm{a}} - \boldsymbol{\Phi}_t]\boldsymbol{e} \end{gathered} \tag{5.17}$$

In which $\boldsymbol{\alpha}, \boldsymbol{\beta}$ and $\boldsymbol{R}_{up}^{pm}$ are the diagonal matrices for axial, tilt and PM-related reluctance. $\mathbf{F}$ is MMF and $\boldsymbol{J}_n$ is an $n \times n$ unit matrix. For the radial poles, the combined flux ϕ_r is also given in (5.17). The individual flux for each radial pole can be further derived by $\phi_r(i) = \phi_r \times R_r./R_r(i)$, where R_r is the equivalent reluctance of all radial poles.

Axial control circuit analysis

The asymmetric model given in Figure 5.5 can also be used to derive the axial control flux. Superposition principle is utilized to acquire the overall flux for the axial poles. For the two axial coils, they are designed to have the same turns N_a and current i_a. The axial control fluxes are given in (5.18):

$$\begin{aligned}\phi_{a1}^{ia} &= \frac{N_a i_a (R_{a2} - \beta||\gamma - R_{fa})}{(\beta||\gamma + R_{fa})R_{a1} + R_{a2}R_{a1} + R_{a2}(\beta||\gamma + R_{fa})} \\ \phi_{a2}^{ia} &= \frac{N_a i_a (2R_{a1} + \beta||\gamma + R_{fa})}{(\beta||\gamma + R_{fa})R_{a1} + R_{a2}R_{a1} + R_{a2}(\beta||\gamma + R_{fa})} \\ \phi_t^{ia} &= \frac{(\phi_{a1}^{ia} + \phi_{a2}^{ia})(\beta||\gamma)}{\beta}\end{aligned} \tag{5.18}$$

Moment control circuit

Based on the EMCM depicted in Figure 5.5, the solution of tilting control circuit is similar to the PM circuit defined previously, only with the PM MMF replaced by the current generated MMF:

$$\begin{aligned}\phi_{a1}^{it}(i)\alpha(i) + \phi_t^{it}(i)\beta(i) &= F_{it}(i) \\ (R_r + R_{fr})\phi_r^{it} + \left[\phi_a^{it}(i) - \phi_t^{it}(i)\right]R_{up}^{pm}(i) + \phi_a^{it}(i)\alpha(i) &= F_{it}(i)\end{aligned} \tag{5.19}$$

$$\begin{bmatrix} \boldsymbol{\alpha} & \boldsymbol{\beta} \\ \boldsymbol{\alpha} + \boldsymbol{R}_{up}^{pm} + \boldsymbol{J}_4(R_r + R_{fr}) & -\boldsymbol{R}_{up}^{pm} - \boldsymbol{J}_4(R_r + R_{fr}) \end{bmatrix} \begin{bmatrix} \boldsymbol{\Phi}_a \\ \boldsymbol{\Phi}_t \end{bmatrix} = \begin{bmatrix} \boldsymbol{F}_t^i \\ \boldsymbol{F}_t^i \end{bmatrix} \tag{5.20}$$

Radial control circuit

The radial portion of the magnetic bear has 8 pole-pairs, 16 poles in total. Allocation of each of the radial flux is governed by the radial position of the flywheel relatively to the C5AMB, and the radial control current MMF.

$$\begin{gathered} \phi_{ri}^{ir}(j)R_{ri}(j) - \phi_{ro}^{ir}(j)R_{ro}(j) + F_{ir}(j) = 0 \\ R_{nr}\phi_{r}^{ir} + \phi_{ri}^{ir}(j)R_{ri}(j) = 0 \\ \phi_{r}^{i} = \sum\left[\phi_{ri}^{i}(j) + \phi_{ro}^{i}(j)\right] \end{gathered} \tag{5.21}$$

where R_{nr} is the equivalent total non-radial reluctance. The solution of (5.21) is given by a set of 16 by 16 linear equations:

$$\begin{bmatrix} \boldsymbol{R}_{ri} & -\boldsymbol{R}_{ro} \\ \boldsymbol{J}_8 R_{nr} + \boldsymbol{R}_{ri} & \boldsymbol{J}_8 R_{nr} \end{bmatrix} \begin{bmatrix} \boldsymbol{\Phi}_{ri} \\ \boldsymbol{\Phi}_{ro} \end{bmatrix} = \begin{bmatrix} -\boldsymbol{F}_{ir} \\ \mathbf{0}_{8,1} \end{bmatrix} \tag{5.22}$$

where $\mathbf{R}_{ri}$ and $\mathbf{R}_{ro}$are the diagonal matrix of inner and outer radial pole reluctance. $\mathbf{F}_{ir}$ is the MMF vector contributed by radial current excitations.

Deriving magnetic force

The superposition principle is utilized to acquire the overall flux for all the magnetic poles.

$$\begin{aligned}\phi_{a1}(i) &= \phi_{a1}^{pm}(i) + \phi_{a1}^{it}(i) + \phi_{a1}^{ia}(i)\\ \phi_{a2}(i) &= \phi_{a2}^{pm}(i) + \phi_{a2}^{it}(i) + \phi_{a2}^{ia}(i)\\ \phi_{t}(i) &= \phi_{t}^{pm}(i) + \phi_{t}^{it}(i) + \phi_{t}^{ia}(i)\\ \phi_{ri}(j) &= \phi_{ri}^{pm}(j) + \phi_{ri}^{ir}(j)\\ \phi_{ro}(j) &= \phi_{ro}^{pm}(j) + \phi_{ro}^{ir}(j)\end{aligned} \tag{5.23}$$

With $f(i)$ defined as the magnetic force of the i^{th} pole. The infinitesimal force $df(i)$ and moment $dM(i)$ are given in the following:

$$\begin{aligned}df(i) &= \frac{1}{2\mu_0}B_g^2(i)dA\\ &= \frac{\mu_0}{2}\left[\frac{F^2(i)}{\left(z+g(i)\right)^2}\right]dA\\ dM(i) &= \vec{r}df(i)\end{aligned} \tag{5.24}$$

where $\vec{r}$ denotes the moment arm, $F(i)$ denotes the combined bias and control MMF for the i^{th} pole. Depends on whether it being a radial or axial/pm pole, the integrated force $f(i)$ for the i^{th} axial/tilt pole is derived based on the formulas given in:

$$f(i) = \iint_{(\pm\phi_a),(r_1,r_2)} \left(\frac{\mu_0}{2}\frac{F_t^2(i)}{\left(z+g_t(i)\right)^2}\right) r dr d\theta \tag{5.25}$$

and the integrated force for the j^{th} radial pole is:

$$f(j) = \int_{-\theta_r}^{+\theta_r} lr\left(\frac{1}{2\mu_0}B_r^2\right)cos\theta d\theta = 2\sin\theta_r\left(\frac{A}{2\mu_0}\right)B_r^2(j) \tag{5.26}$$

The integrated moment for the i^{th} pothe le is given in given by:

$$M(i) = \iint_{(-\phi,+\phi),(r_1,r_2)} \left(\frac{\mu_0}{2} \frac{F_t^2(i)}{\left(z + g_i(i)\right)^2} \vec{r} \right) r dr d\phi \tag{5.27}$$

Analysis of the C5AMB

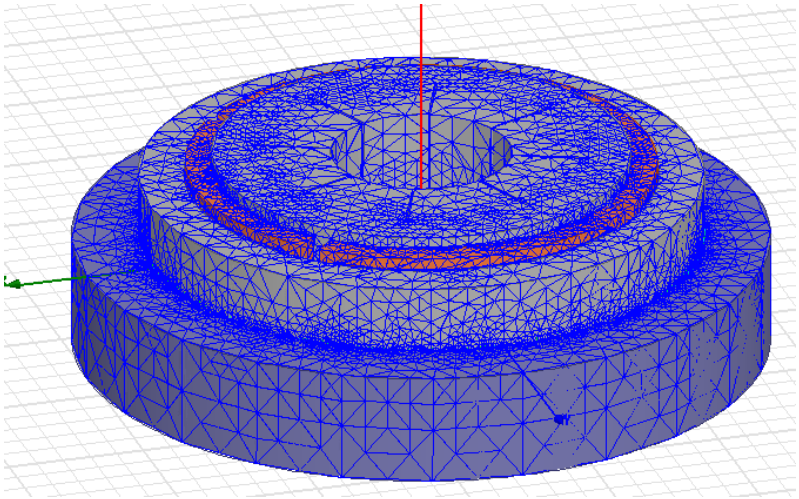

Figure 5.9 3D, Solid Mesh FEM Model of the C5AMB-SHFES by a Commercial Software.

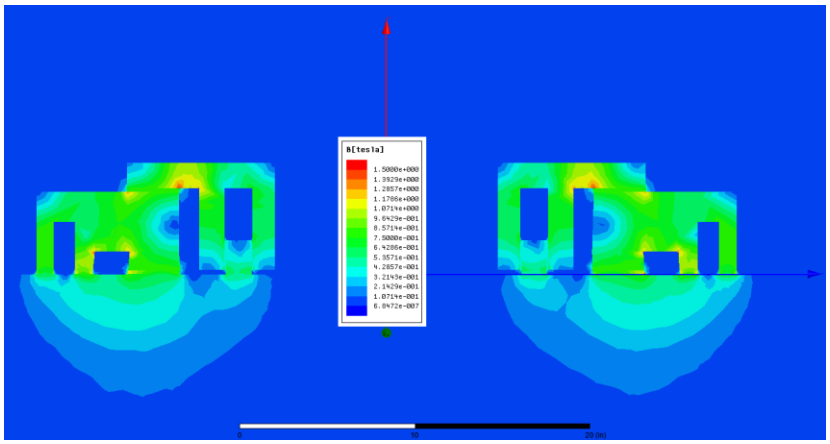

Figure 5.10 A Section View of the Flux Density Plot of the C5AMB-SHFES

With the EMCM fully developed, the force-to-position and force-to-current characteristics are analyzed by the mathematical formulas and compared with FEM.

Depicted in Figure 5.9 and Figure 5.10, the FEM simulation adopts a 3D, solid mesh model with a nonlinear and adaptive solver to ensure converged results. The current excitations are carried by stranded wires. The FEM simulation costs significant time and effort and is used for verification and fine-tuning purpose. Also, the coupling effects between different actuators are also investigated by EMCM.

Force/Moment vs. Position

The force to position relationship is analyzed when zero control current is applied to the MB. Both EMCM and FEM results are given for comparison. Figure 5.11 (a) shows the radial magnetic force w.r.t. the radial displacement. The total allowable radial displacement is ±1.27mm. For the EMCM results, radial force vs. position relation is linear up to 0.5 mm of deviation, while the 3D FEM results are linear up to 1 mm. Figure 5.11 (b) shows the axial force to position relations. The nominal axial air gap is about 1.14mm. Moment caused by attitude changes of the flywheel is depicted in Figure 5.11 (c). Generally, the EMCM overestimates the force/moment w.r.t. position and attitude because that it has not taken the saturation and fringing effects into account.

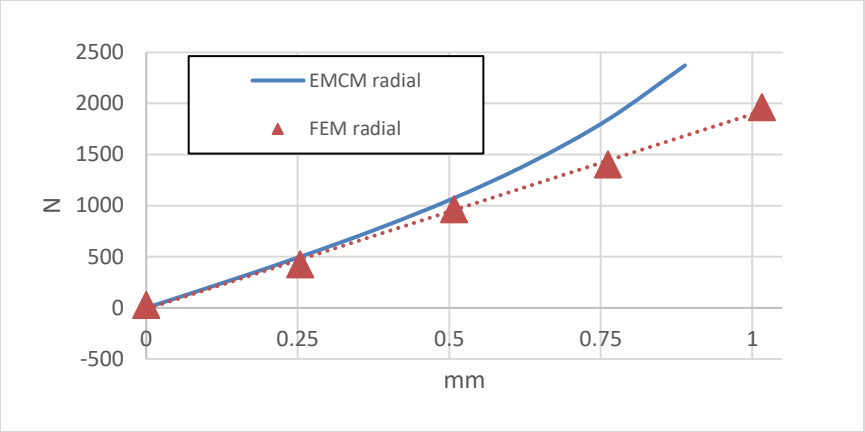

(a)

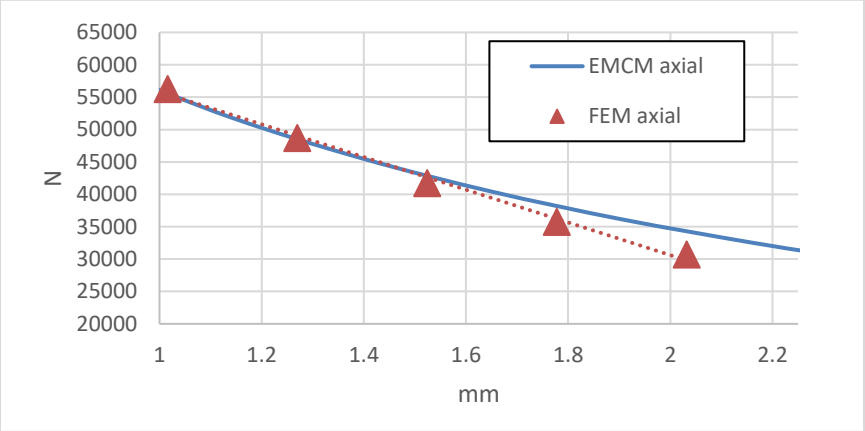

(b)

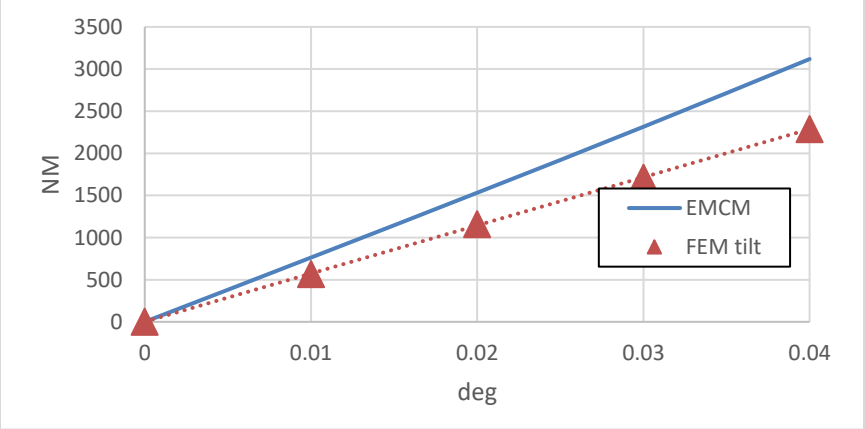

(c)

Figure 5.11 The Force/Moment vs. Flywheel Position

Force/Moment vs. Current

The force/moment to current plots are acquired when the flywheel is placed at the magnetic equilibrium position radially. The axial air gap is set to generate a force equal to its weight. Figure 5.12 (a) shows the radial forces vs. current excitations. The radial coil is designed to have 100 turns. The maximum excitation current is set to 10 A, which will give a maximum ampere-turn of 1000 AT. Figure 5.12 (b) shows the axial force vs. current excitation. In this case, the ampere-turn excitation is set to -500 AT to 500AT. The moment to current excitation relation is depicted Figure 5.12 (c). In general, the EMCM and FEM results agree well for force/moment-to-current relations.

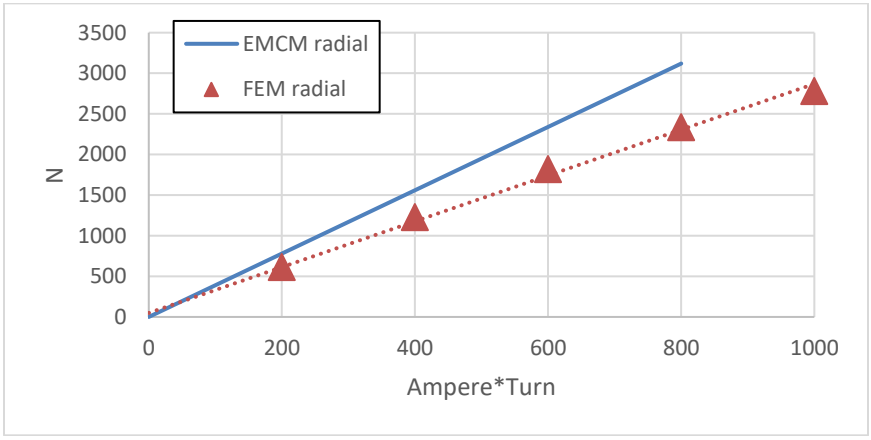

(a)

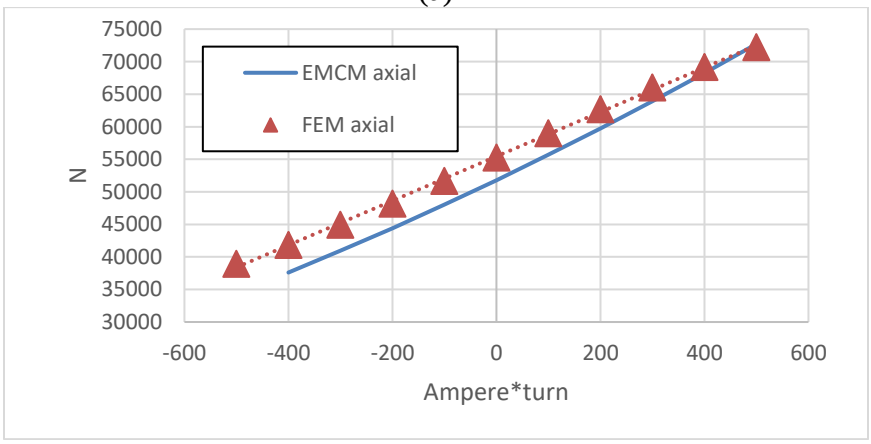

(b)

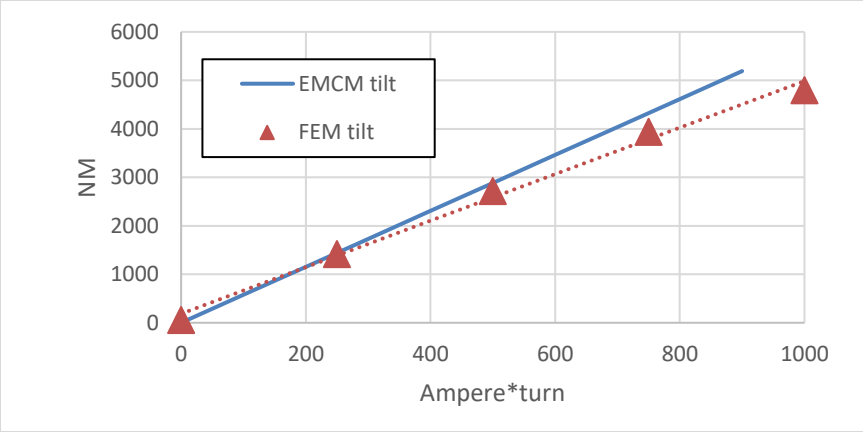

(c)

Figure 5.12 The Force/Moment vs. Control Current

Position Coupling effects

Because that the C5AMB has shared flux path between radial, tilt and axial magnetic poles. The coupling effects between actuators are also investigated. While y-axis displacement will create a negligible radial force in the x-direction, it does affect the radial reluctance and bias flux, which subsequently affects x-axis force-to-position relationships. In detail, when y motion is significant in either direction, x-axis will have larger position stiffness and become more nonlinear. Figure 5.13 (a) depicts the coupling effects between radial motions. The tilting displacements of the flywheel create a small change in the combined equivalent axial reluctances and could potentially impact axial force. As depicted in Figure 5.13 (b), a significant tilting motion will cause some extra axial force. When θ_x and θ_y both are tilted at 0.04 deg, the axial force is 6% larger than its nominal. Nevertheless, when the tilt angles are smaller between 0 to 0.02 deg, the axial force is almost unaffected. As shown in Figure 5.13 (c). There is no moment coupling effect between tilt motions.

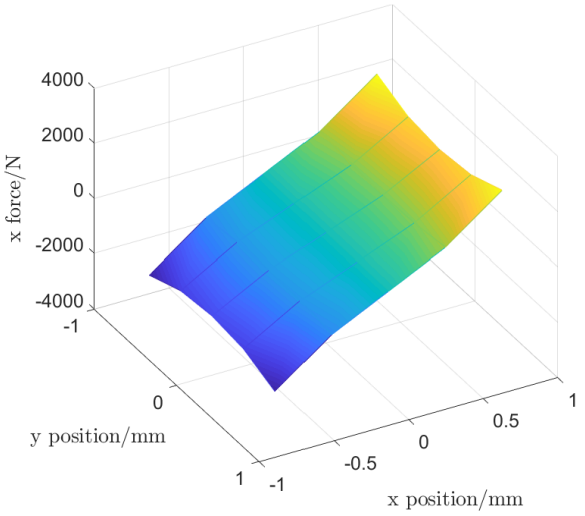

(a)

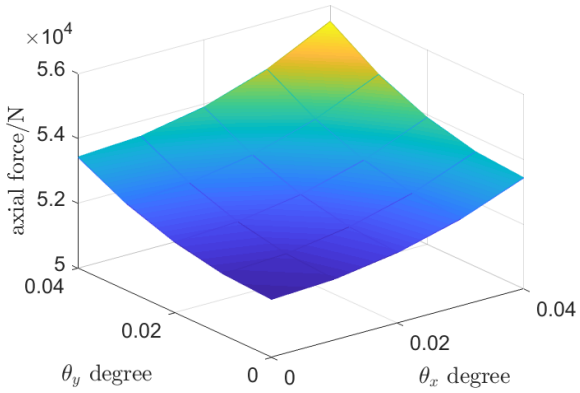

(b)

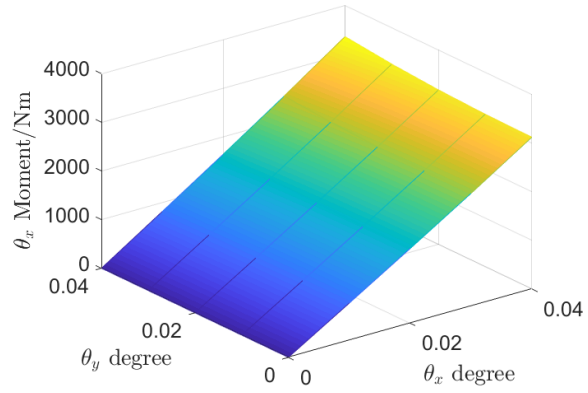

(c)

Figure 5.13 Position-Force/Moment Coupling Analysis

Current Coupling effects

For the couple effects from current excitations, the radial poles are linear (shown in Figure 5.14(a)) and show minimal coupling effects since that currents are applied in pairs with reversed directions, which sums near zero bias flux for the rest poles in the system. Also, there is no coupling effect found between the tilting excitations (as shown in Figure 5.14 (c)). Pm poles show little to none impact on the axial force. As depicted in Figure 5.14 (b), a -400 Ampere turn tilting currents of θ_x and θ_y only cause the axial force to deviate by less than 1% of its nominal value.

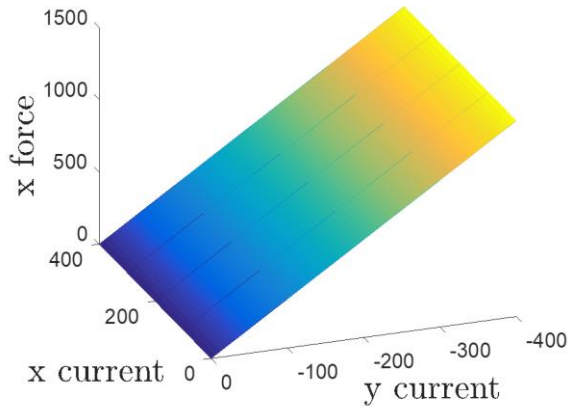

(a)

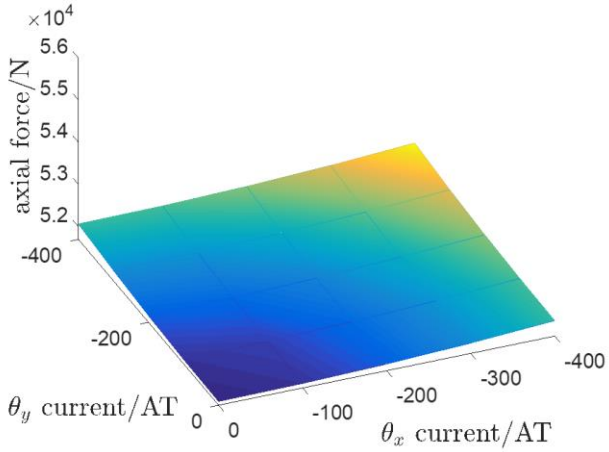

(b)

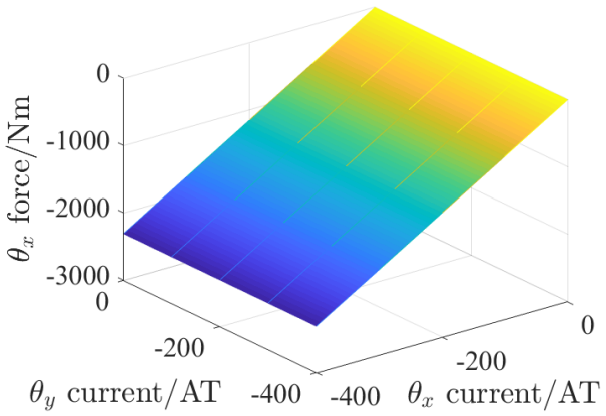

(c)

Figure 5.14 Current-Force/Moment Coupling Analysis

Frequency Response of the C5AMB

Since the linearized magnetic force w.r.t. the excitation current:

$$f = \frac{1}{2\mu_0}\oint \left(B_{pm} + B_i\right)^2 dA$$
$$f(\omega) \approx \frac{B_{pm}}{\mu_0}\oint B_i(\omega)\, dA \rightarrow \frac{f(\omega)}{f(0)} \approx \frac{\phi(\omega)}{\phi(0)} \tag{5.28}$$

The frequency response of force to current can be approximated by the frequency response of flux ($\phi_i(\omega)$) to current or the average flux density ($\bar{B}_i(\omega)$) to current.

FEM model

The FEA simulation (shown in Figure 5.15) of eddy current effects depends on the proper modeling of skin depth, which is a function of permeability, conductivity, and frequency

$$\delta = \sqrt{\frac{2}{\omega\sigma\mu_0\mu_r}} \tag{5.29}$$

where ω is the frequency. σ is the conductivity. μ_r is the relative permeability. μ_0 is the permeability of free space.

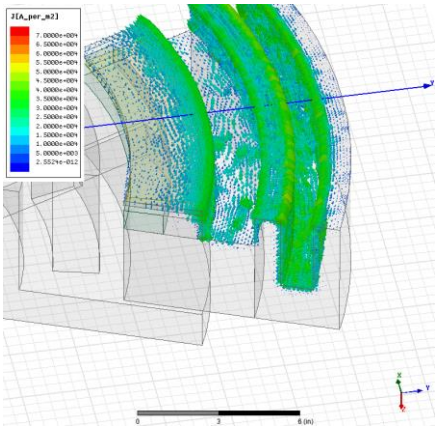

Figure 5.15 FEM Simulation of Eddy Current Effects on C5AMB

Testing Results of the Frequency Response of the C5AMB

Figure 5.16 In-house Magnetic Field Density Measurement Tool

With regret, for the C5AMB, only the axial and tilt flux to current responses are accessible for measurement with the present equipment (as depicted in Figure 5.16). However, the frequency responses of the axial and tilt actuators are directly related to the gyroscopic effects and crucial to the flywheel's stability. The axial response is displayed in Figure 5.17. In the following chapter, these data are curved fitted as transfer functions and included in the system dynamical modeling.

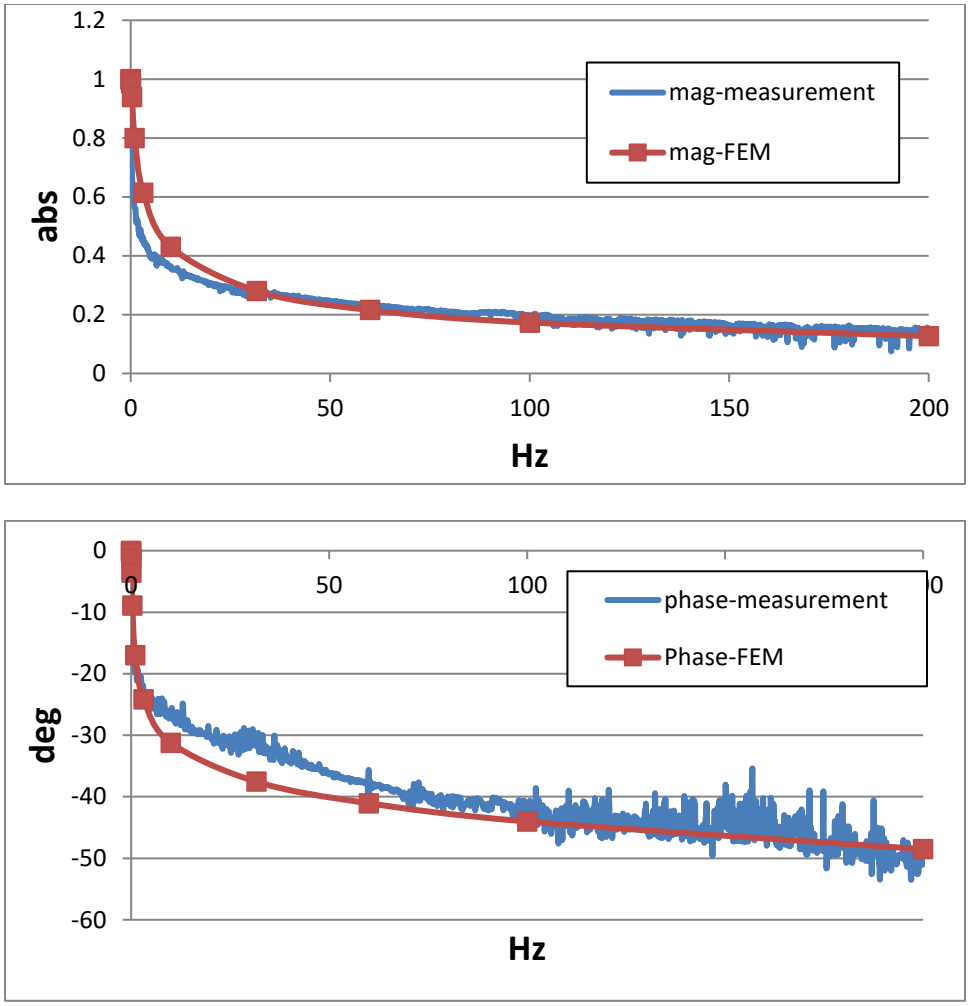

Figure 5.17 Axial Pole Frequency Responses

CHAPTER VI

MODELING AND CONTROL OF THE SHFES*

Modeling of the SHFES

The entire electromechanical system simulation includes following parts:

- Magnetic bearing with eddy current effects
- Flywheel with Gyroscopic effects
- Flexible Housing structure
- Sensor dynamics
- Power amplifiers with saturation effects and Coil inductance/ resistance
- Feedback controller with SISO and MIMO control algorithms

Modeling of the C5AMB

To include the C5AMB into system dynamic simulation. It is characterized by static and frequency-dependent coefficients. Static characteristics of the C5AMB include position and current stiffness (shown in Table 6.1).

TABLE 6.1 THE MEASURED CURRENT AND POSITION STIFFNESS OF THE C5AMB

	Axial	Radial	Tilting
K_p	-2.599e7(N/m)	-1.858e6(N/m)	-2.737e6(Nm/rads)
K_i	3714(N/A)	343(N/A)	546(Nm/A)
Coil Turns	100×2	100	100

*Part of this chapter is reprinted with permission from "Multi-Input Multi-Output control of a utility scale, shaft-less energy storage flywheel with a 5-DOF combination magnetic bearing" by X. Li and A. Palazzolo, 2014., *ASME. J. Dyn. Sys., Meas., Control. 2018; doi:10.1115/1.4039857.* Copyright [2018] by ASME.

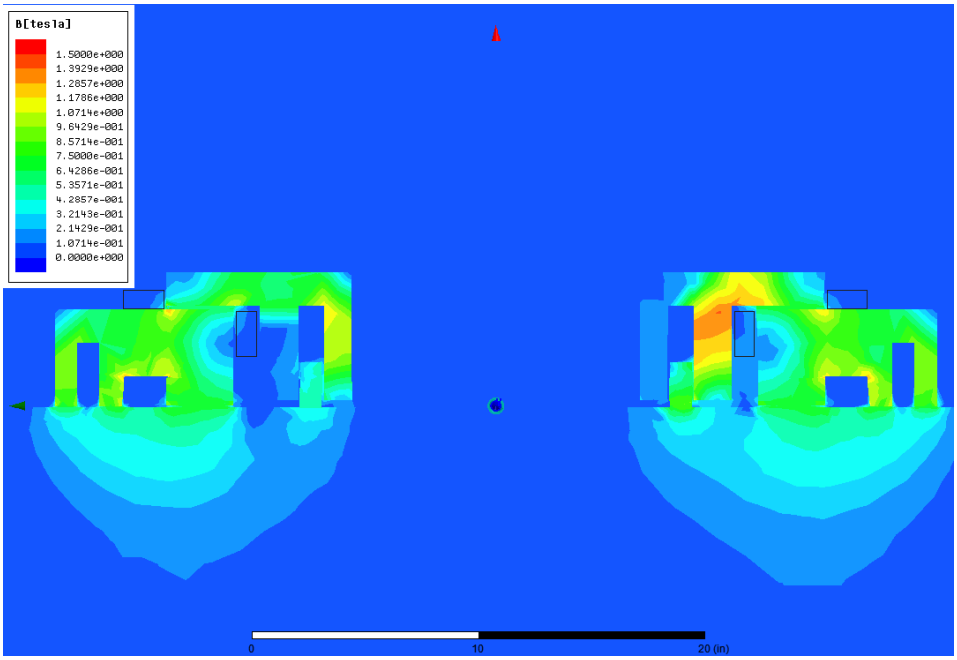

Figure 6.1 Section Flux Plot of the 3D Electromagnetic Static Simulation

Studies are carried out near the equilibrium position where the flywheel is centered horizontally and 50/1000 inch below the C5AMB vertically. At the equilibrium position, current stiffness is acquired by giving current excitations at different amperages to the radial, axial and tilting coils respectively. Similarly, position stiffness is obtained by studying the electromagnetic forces when different position/attitude is applied to the flywheel. As shown in Figure 6.1, there are both radial and axial flux paths in the C5AMB. The conventional laminated design is difficult to be applied and not cost-effective. Eddy current effects cause phase lags and magnitude mitigations in the electromagnetic force as the excitation frequency increases. This phenomenon may affect system dynamics. The frequency responses of electromagnetic the force to the excitation current could be approximated by the frequency response of controlled flux to the current excitation [59].

Since the AMB is also designed to work in the linear range, The results are curve fitted [68] as transfer functions (depicted in Figure 6.2) and incorporated into the later dynamical system modeling.

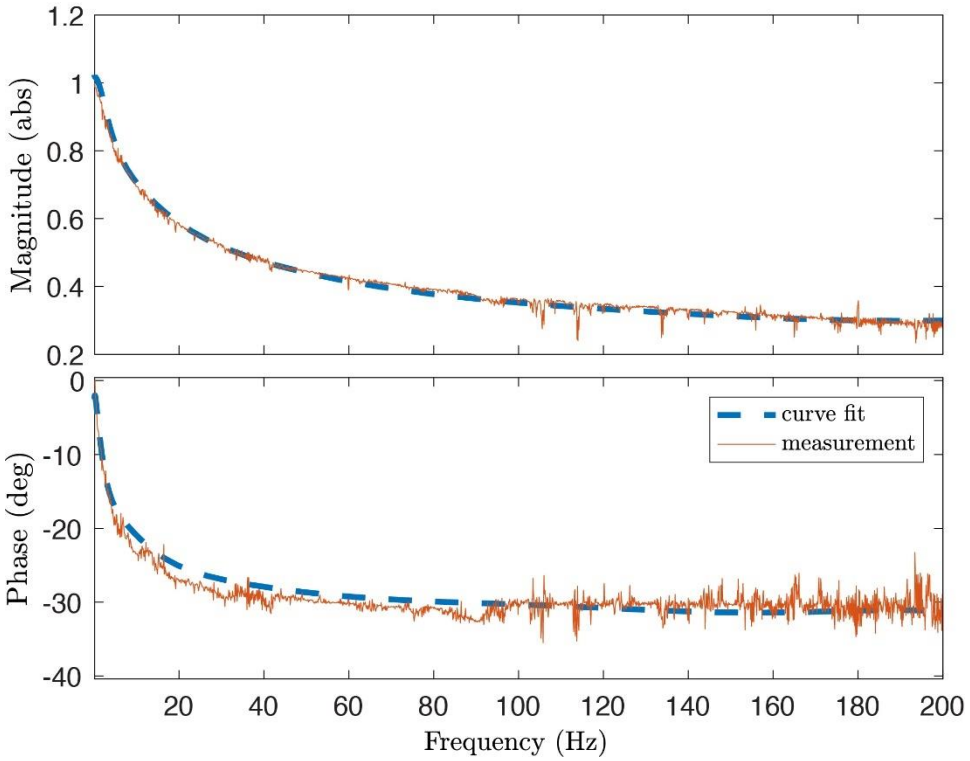

Figure 6.2 Curve Fitting for the C5AMB Frequency Response: Tilt Pole

In summary, the magnetic force generated by the C5AMB is given in:

$$\boldsymbol{f}_{em} = \boldsymbol{K}_p\left(\boldsymbol{q}_s^* - \boldsymbol{q}_f\right) + \boldsymbol{TF}_{if}\boldsymbol{K}_i\boldsymbol{I} \tag{6.1}$$

where $\boldsymbol{q}_s^*$ is the displacement vector of the stator nodes that holds the C5AMB. $\boldsymbol{q}_f$ is the displacement vector of the flywheel itself. $\boldsymbol{TF}_{if}\boldsymbol{K}_i\boldsymbol{I}$ is the current induced magnetic force term with $\boldsymbol{K}_i$ being the static current stiffness matrix, $\boldsymbol{TF}_{if}$ being the frequency dependent

transfer function matrix, and $\boldsymbol{I}$ being the excitation current vector. Aforementioned, the transfer functions are curve-fitted:

$$TF_i(j) = \frac{\sum_{i=0}^{N} a_i s^{N-i}}{\sum_{i=0}^{M} b_i s^{M-i}} \tag{6.2}$$

Modeling of the Support Structure

The shaftless design eliminates some of the flexible shaft modes. There is no need to model the flywheel as a flexible rotor. Nevertheless, The C5AMB is supported by a housing structure that plays an important role in system dynamics. A beam element FEM model is used for modeling the support structure and the C5AMB (together will be referred as the stator).

$$\boldsymbol{M}_s\boldsymbol{q}_s + \boldsymbol{C}_s\dot{\boldsymbol{q}}_s + \boldsymbol{K}_s\boldsymbol{q}_s = -\boldsymbol{f}_{em} \tag{6.3}$$

in which $\boldsymbol{M}_s$ and $\boldsymbol{K}_s$ are the mass and stiffness matrices. $\boldsymbol{q}_s$ is stator's displacement vector, defined as following:

$$\boldsymbol{q}_s = \left[\theta_{x,1}, \theta_{y,1}, x_1, y_1, z_1, \dots, \theta_{x,n}, \theta_{y,n}, x_n, y_n, z_n\right]^T \tag{6.4}$$

where n is the number of free nodes. The $\boldsymbol{C}_s$ matrix is proportional damping based on:

$$\boldsymbol{C}_s = a\boldsymbol{M}_s + b\boldsymbol{K}_s \tag{6.5}$$

The coefficients are obtained by assuming normalized 2% damping at 60Hz and 1% damping at 100Hz. The finite element model of housing structure includes 28 nodes and 144 DOF. As depicted in Figure 6.3, two types of beam elements are used. The green colored elements are solid beams arranged in an octagon shape for approximating the circle thin wall component in the housing structure. The reaction force from the flywheel is applied to the theses nodes. The orange colored elements are I-beams for modeling the

rest part of the structure. The 28-node-FEM model has similar natural frequencies comparing to the solid model but requires much less computational effort. Figure 6.3 depicts the FEM. To include the C5AMB into the housing structure, it is modeled by shell elements defined by the green nodes. These elements bring further stiffness in addition to the thin wall elements.

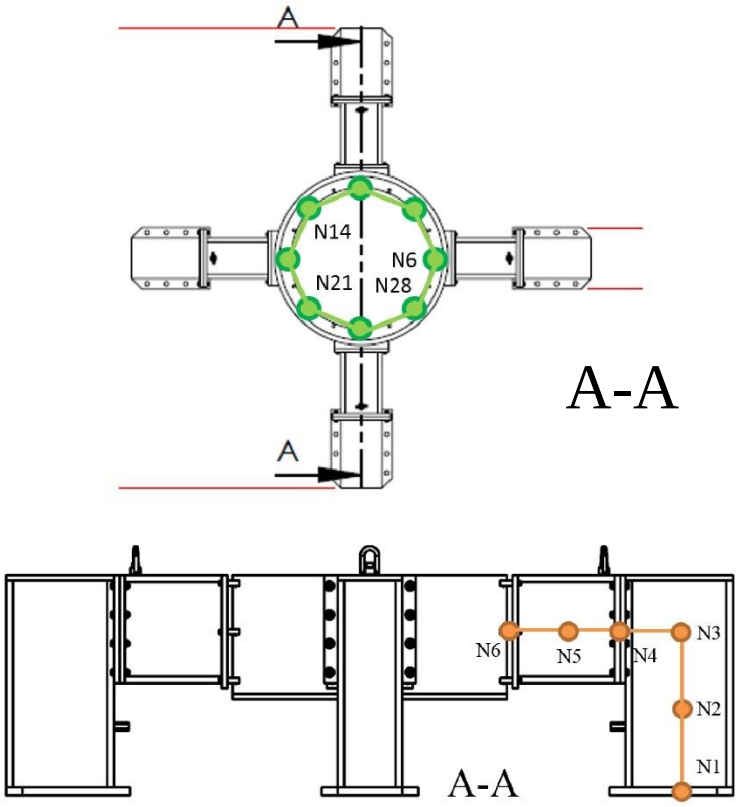

Figure 6.3 Housing Structure Nodes and Beam Elements

A 3D view of the model in beam elements is illustrated in Figure 6.4 and Figure 6.5.

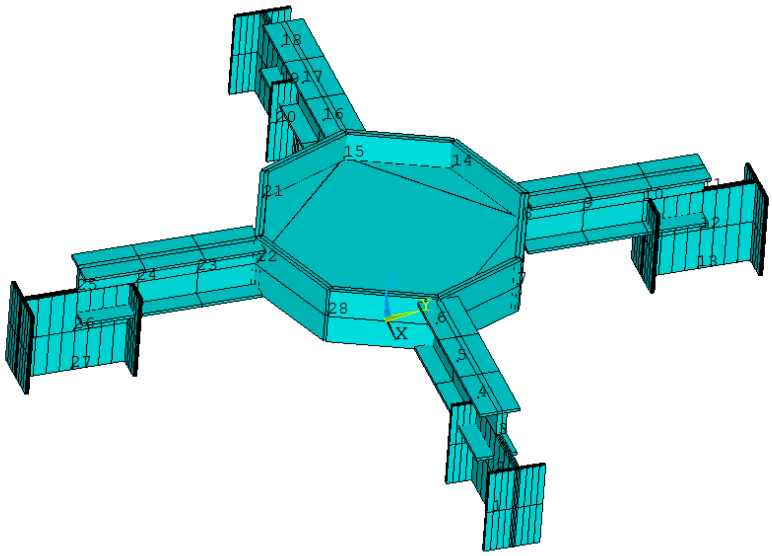

Figure 6.4 Housing Structure Modeling in FEA Software

TABLE 6.2 FORCE AND SENSOR ALLOCATION ON HOUSING NODES

	Radial		Axial	Moment	
	X	Y	Z	M_{θ_x}	M_{θ_y}
Reaction force Nodes	N6, N15, N8, N22 N7, N14, N21, N28		N6~8, N14~15, N21~22, N28	N7 N8 N14, N21 N22 N28	N14 N15 N21, N6 N7 N28
Sensor nodes	N6, N15, N8, N22		N6, N15, N8, N22	N8, N22	N15, N6

Table 6.2 describes the allocation of force/sensor nodes. The force/moment distribution matrix $\boldsymbol{D}_f$, which converts the magnetic forces from the C5AMB's coordinate to the coordinate of the housing structure, is defined in (6.6):

$$\boldsymbol{f}_{em}^{st}(i) == \boldsymbol{D}_f(i)\begin{bmatrix} M_{\theta x} \\ M_{\theta y} \\ f_x \\ f_y \\ f_z \end{bmatrix} \tag{6.6}$$

where:

$$\boldsymbol{D}_f(6) = \begin{bmatrix} 0 & 0 & \frac{1}{8} & 0 & 0 \\ 0 & 0 & 0 & \frac{1}{8} & 0 \\ 0 & -m2f & 0 & 0 & \frac{1}{8} \\ 0 & & \dots & & 0 \\ \vdots & & \ddots & & \vdots \\ 0 & & \dots & & 0 \end{bmatrix}, \boldsymbol{D}_f(7) = \begin{bmatrix} 0 & 0 & \frac{1}{8} & 0 & 0 \\ 0 & 0 & 0 & \frac{1}{8} & 0 \\ m2f & -m2f & 0 & 0 & \frac{1}{8} \\ 0 & & \dots & & 0 \\ & & \ddots & & \\ 0 & & \dots & & 0 \end{bmatrix},$$

$$\boldsymbol{D}_f(8) = \begin{bmatrix} 0 & 0 & \frac{1}{8} & 0 & 0 \\ 0 & 0 & 0 & \frac{1}{8} & 0 \\ m2f & 0 & 0 & 0 & \frac{1}{8} \\ 0 & & \dots & & 0 \\ \vdots & & \ddots & & \ddots \\ 0 & & \dots & & 0 \end{bmatrix}$$

$$\boldsymbol{D}_f(14) = 0\begin{bmatrix} 0 & 0 & \frac{1}{8} & 0 & 0 \\ 0 & 0 & 0 & \frac{1}{8} & 0 \\ m2f & m2f & 0 & 0 & \frac{1}{8} \\ 0 & & \dots & & 0 \\ \vdots & & \ddots & & \vdots \\ 0 & & \dots & & 0 \end{bmatrix}, \boldsymbol{D}_f(15) = \begin{bmatrix} 0 & 0 & \frac{1}{8} & 0 & 0 \\ 0 & 0 & 0 & \frac{1}{8} & 0 \\ 0 & m2f & 0 & 0 & \frac{1}{8} \\ 0 & & \dots & & 0 \\ \vdots & & \ddots & & \vdots \\ 0 & & \dots & & 0 \end{bmatrix}$$

$$\boldsymbol{D}_f(21) = \begin{bmatrix} 0 & 0 & \frac{1}{8} & 0 & 0 \\ 0 & 0 & 0 & \frac{1}{8} & 0 \\ -m2f & m2f & 0 & 0 & \frac{1}{8} \\ 0 & & \dots & & 0 \\ \vdots & & \ddots & & \vdots \\ 0 & & \dots & & 0 \end{bmatrix}, \boldsymbol{D}_f(22) = \begin{bmatrix} 0 & 0 & \frac{1}{8} & 0 & 0 \\ 0 & 0 & 0 & \frac{1}{8} & 0 \\ -m2f & 0 & 0 & 0 & \frac{1}{8} \\ 0 & & \dots & & 0 \\ \vdots & & \ddots & & \ddots \\ 0 & & \dots & & 0 \end{bmatrix}$$

$$\boldsymbol{D}_f(28) = \begin{bmatrix} 0 & 0 & \frac{1}{8} & 0 & 0 \\ 0 & 0 & 0 & \frac{1}{8} & 0 \\ -m2f & -m2f & 0 & 0 & \frac{1}{8} \\ 0 & & \cdots & & 0 \\ \vdots & & \ddots & & \vdots \\ 0 & & \cdots & & 0 \end{bmatrix}$$

where $m2f = -\frac{1}{(\sqrt{2}+1)D_s}$ is the factor that converts the flywheel moment to node magnetic forces.

The sensor transfer matrix, which collects the position sensor data in the structure housing's coordinate and converts them to the controller/flywheel coordinate, is defined in (6.7):

$$\boldsymbol{q}_s^c = \begin{bmatrix} \theta_x \\ \theta_y \\ x \\ y \\ z \end{bmatrix} = \sum \boldsymbol{D}_s(i)\boldsymbol{q}_s(i) \tag{6.7}$$

where:

$$\boldsymbol{D}_s(6) = \begin{bmatrix} 0 & 0 & 0 & 0 & 0 & 0 \\ 0 & 0 & \frac{1}{D_s} & 0 & 0 & 0 \\ \frac{1}{8} & 0 & 0 & 0 & 0 & 0 \\ 0 & \frac{1}{8} & 0 & 0 & 0 & 0 \\ 0 & 0 & \frac{1}{8} & 0 & 0 & 0 \end{bmatrix}, \boldsymbol{D}_s(7) = \begin{bmatrix} 0 & 0 & 0 & 0 & 0 & 0 \\ 0 & 0 & 0 & 0 & 0 & 0 \\ \frac{1}{8} & 0 & 0 & 0 & 0 & 0 \\ 0 & \frac{1}{8} & 0 & 0 & 0 & 0 \\ 0 & 0 & \frac{1}{8} & 0 & 0 & 0 \end{bmatrix},$$

$$\boldsymbol{D}_s(8) = \begin{bmatrix} 0 & 0 & \frac{1}{D_s} & 0 & 0 & 0 \\ 0 & 0 & 0 & 0 & 0 & 0 \\ \frac{1}{8} & 0 & 0 & 0 & 0 & 0 \\ 0 & \frac{1}{8} & 0 & 0 & 0 & 0 \\ 0 & 0 & \frac{1}{8} & 0 & 0 & 0 \end{bmatrix}$$

$$\boldsymbol{D}_s(14) = \begin{bmatrix} 0 & 0 & 0 & 0 & 0 & 0 \\ 0 & 0 & 0 & 0 & 0 & 0 \\ \frac{1}{8} & 0 & 0 & 0 & 0 & 0 \\ 0 & \frac{1}{8} & 0 & 0 & 0 & 0 \\ 0 & 0 & \frac{1}{8} & 0 & 0 & 0 \end{bmatrix}, \boldsymbol{D}_s(15) = \begin{bmatrix} 0 & 0 & 0 & 0 & 0 & 0 \\ 0 & 0 & -\frac{1}{D_s} & 0 & 0 & 0 \\ \frac{1}{8} & 0 & 0 & 0 & 0 & 0 \\ 0 & \frac{1}{8} & 0 & 0 & 0 & 0 \\ 0 & 0 & \frac{1}{8} & 0 & 0 & 0 \end{bmatrix}$$

$$\boldsymbol{D}_s(21) = \begin{bmatrix} 0 & 0 & 0 & 0 & 0 & 0 \\ 0 & 0 & 0 & 0 & 0 & 0 \\ \frac{1}{8} & 0 & 0 & 0 & 0 & 0 \\ 0 & \frac{1}{8} & 0 & 0 & 0 & 0 \\ 0 & 0 & \frac{1}{8} & 0 & 0 & 0 \end{bmatrix}, \boldsymbol{D}_s(22) = \begin{bmatrix} 0 & 0 & -\frac{1}{D_s} & 0 & 0 & 0 \\ 0 & 0 & 0 & 0 & 0 & 0 \\ \frac{1}{8} & 0 & 0 & 0 & 0 & 0 \\ 0 & \frac{1}{8} & 0 & 0 & 0 & 0 \\ 0 & 0 & \frac{1}{8} & 0 & 0 & 0 \end{bmatrix},$$

$$\boldsymbol{D}_s(22) = \begin{bmatrix} 0 & 0 & 0 & 0 & 0 & 0 \\ 0 & 0 & 0 & 0 & 0 & 0 \\ \frac{1}{8} & 0 & 0 & 0 & 0 & 0 \\ 0 & \frac{1}{8} & 0 & 0 & 0 & 0 \\ 0 & 0 & \frac{1}{8} & 0 & 0 & 0 \end{bmatrix}$$

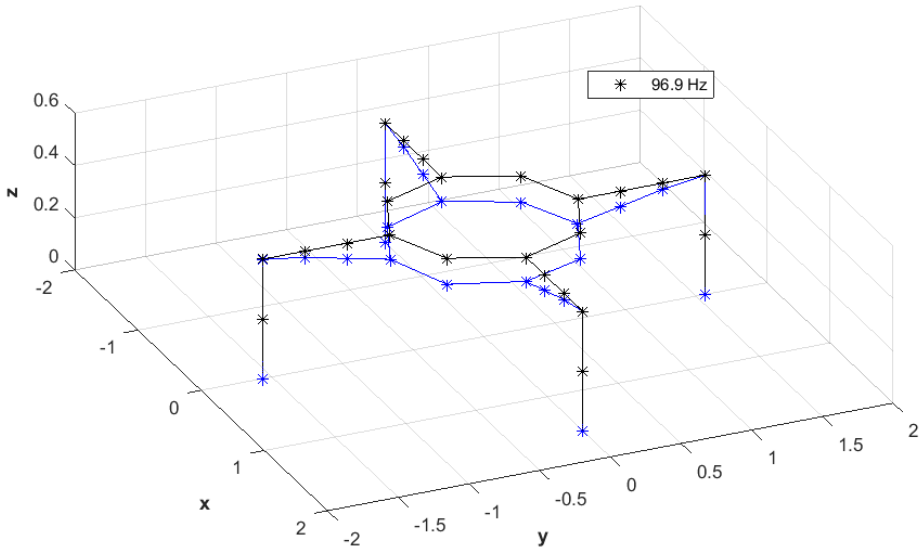

Figure 6.5 Housing Structure Mode Shapes

The flywheel's equation of motion (EOM) is given below:

$$\boldsymbol{M}_f\ddot{\boldsymbol{q}}_f + \boldsymbol{G}_f(\omega)\dot{\boldsymbol{q}}_f = \boldsymbol{f}_{em} + \boldsymbol{f}_{im} \tag{6.8}$$

In which $\boldsymbol{q}_f = \left[\theta_{x,f}, \theta_{y,f}, x_f, y_f, z_f\right]^T$ denotes the flywheel position vector. The Imbalance force is defined as $\boldsymbol{f}_{im} = [0,0, me\omega^2 cost(\omega t), me\omega^2 \sin(\omega t), 0]^T$. $\boldsymbol{G}_f(\omega)$ denotes the speed dependent gyroscopic matrix.

Modeling of the Power Amplifier and Coil

Power amplifiers are modeled as simple proportional feedback systems that include coil inductance and resistance. The governing equations of power amplifiers are given in the following:

$$\boldsymbol{V} = \boldsymbol{K}_{PA}(\boldsymbol{G}_{PA}\boldsymbol{v} - \boldsymbol{i}) = \boldsymbol{L}\frac{d\boldsymbol{i}}{dt} + \boldsymbol{R}\boldsymbol{i} \tag{6.9}$$

where $\boldsymbol{K}_{PA}$ denotes the feedback gain matrix and $\boldsymbol{G}_{PA}$ denotes the amplification matrix for the power amplifiers respectively. The amplifier voltage and current are limited to their maximum thresholds:

$$-\boldsymbol{V}_{lim} < \boldsymbol{V} < \boldsymbol{V}_{lim} \tag{6.10}$$

AMB coil inductances have substantial effects on the power amplifier bandwidth. To accurately estimate the flywheel's dynamics, inductances are measured experimentally by exciting each coil with sinusoidal voltages and recording their current responses:

$$\frac{I(\omega)}{V(\omega)} = \frac{1}{Lj\omega + R} \tag{6.11}$$

While more sophisticated models consider the frequency-dependent characteristics of *R* and *L* [69]. Adopted here is a simple model. The measurements were carried out when the flywheel is at the equilibrium position. The inductances and resistance are derived around the operational frequency (5000 RPM).

Modeling of the Sensors and Disturbances

Proximity sensors, which are often referred to as Eddy Current sensors, are typically used in AMB suspension control. In general, these sensors have a relatively high bandwidth of nearly10 kHz. The sensor dynamics are summarized as follows:

$$\boldsymbol{u} = \frac{\boldsymbol{G}_{sn}}{(\boldsymbol{T}_{sn}s + 1)}\left(\boldsymbol{q}_s - \boldsymbol{q}_f + \boldsymbol{q}_r\right) \tag{6.12}$$

where $\boldsymbol{q}_s$ and $\boldsymbol{q}_f$ are the stator and flywheel position vectors in the C5AMB's coordinate. $\boldsymbol{G}_{sn}$ and $\boldsymbol{T}_{sn}$ are the sensitivity and filter constant matrices. As depicted in Figure 6.6, the average sensitivity is about 178mv/mil.

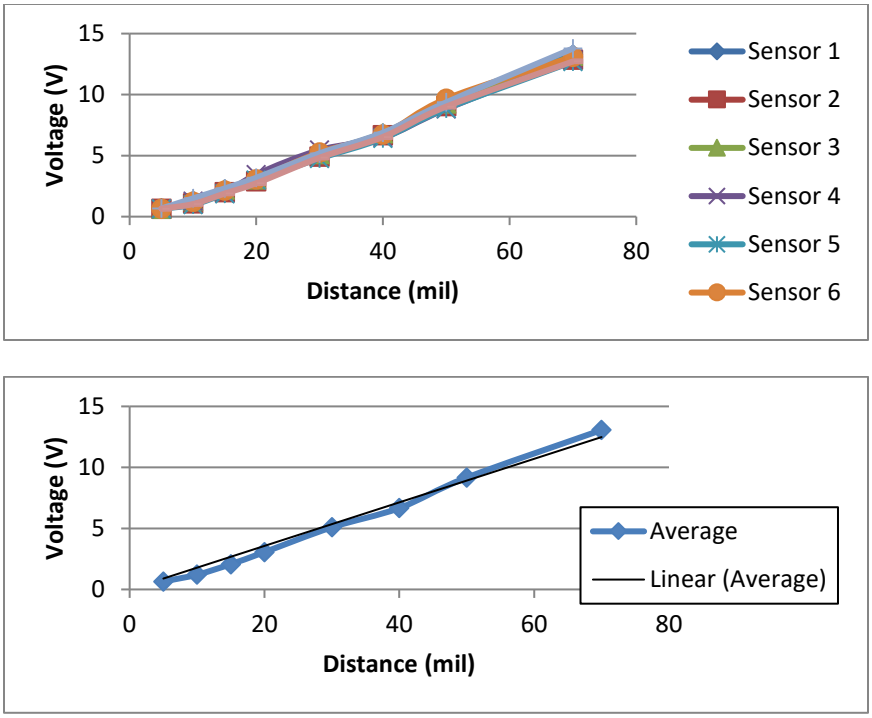

Figure 6.6 Sensitivity Measurements of the Proximity Sensors

The $\boldsymbol{q}_r$ vector denotes the sensor runout components. As defined in (6.13), they are modeled as a synthesis of sinusoidal signals that are speed-dependent of the running speed:

$$\boldsymbol{q}_r = \sum_{i=1}^{N} A_n \sin(f_n \omega t) + B_n \cos(f_n \omega t) \tag{6.13}$$

The magnitude A_n of the n^{th} harmonic is measured by slowly rolling the flywheel when it is magnetically suspended. Notice that, apart from the surface unevenness of the flywheel, vertical or horizontal misalignments between the flywheel and the stator may also contribute to the runouts.

Multiple-Input-Multiple-Output (MIMO) Control

Since the flywheel itself is very close to the form of a thin disk. The ratio of I_p to I_t is almost 2. The gyroscopic effect is notable. It generates pairs of forward and backward conical modes. As the spin speed increases, the rigid body forward modes will converge to a slope of spin speed ($\omega I_p/I_t$), and the backward one will converge to zero. Gyroscopic effect alone only pulls the poles to the imaginary axis, which causes the system to become marginally stable. However, with certain phase lags from the AMB, amplifiers or other parts of the system, these modes will become unstable. While a single-input-single-output (SISO) control algorithm will levitate the flywheel at zero RPM, it is not able to stabilize the system when the flywheel is at a higher speed. Multiple-input-multiple-output (MIMO) algorithm [39,70,71] is applied to cancel some of the gyroscopic moment effects. The controller also features a proportional and derivative (PD) stage, multiple lead-lag filters and multiple notch filters. Main task of the control algorithm is to stabilize the flywheel and prevent the power amplifier, digital controller and the magnetic bearing from being working under saturation conditions. The rotor imbalance and sensor runout signals can be viewed as speed dependent disturbances in the system with the imbalance being applied to the flywheel and runout signals applied to the sensor. In particular, high frequency harmonica components of the sensor runout signals will be magnified by derivative feedback, causing a great burden on the power amplifiers. Therefore, multiple notch filters are designed for each controlling target to suppress the disturbances.

The overall control algorithm is summarized by (6.14):

$$\boldsymbol{v} = \left(\boldsymbol{P} + \boldsymbol{D}\frac{s}{\tau s + 1}\right)\left[\boldsymbol{L}_l \boldsymbol{L}_g \boldsymbol{N}_f\right]\boldsymbol{T}_{u2v}(\boldsymbol{u} - \boldsymbol{u}^T) \tag{6.14}$$

The proportional gain matrix is defined as (6.15)

$$\boldsymbol{P} = \begin{bmatrix} P_x & & & & \\ & P_y & & & \\ & & P_{\theta x} & P_{\theta c} & \\ & & -P_{\theta c} & P_{\theta y} & \\ & & & & P_z \end{bmatrix} \tag{6.15}$$

And the derivative matrix is defined in (6.16)

$$\boldsymbol{D} = \begin{bmatrix} D_x & & & & \\ & D_y & & & \\ & & D_{\theta x} & -D_{\theta c} & \\ & & D_{\theta c} & D_{\theta y} & \\ & & & & D_z \end{bmatrix} \tag{6.16}$$

where $P_{\theta c}$ and $D_{\theta c}$ are the cross-couple proportional and derivative coefficients. In the effort of weakening the gyroscopic effect, the cross-coupled feedback applies torque in one plane per the angular position/velocity of its quadrature plane. This strategy reduces the speed dependency of system dynamics (conical modes) and lower the frequency of forward modes so that the direct derivate gains can be more effective [39]. In addition to the PD regulators and lag compensators, each feedback channel also includes various lead compensators and notch filters. The lead compensator provides derivatives for a specific range of frequencies so that the system's stability and response can be improved. The transfer function being used for the lead compensator is defined in (6.17):

$$\boldsymbol{L}_l = \prod_{i=1}^{N} \boldsymbol{diag}_i \left(\frac{\alpha(1)T(1)s + 1}{T(1)s + 1} \quad \cdots \quad \frac{\alpha(5)T(5)s + 1}{T(5)s + 1} \right) (lead\ stages)$$
$$where\ \alpha(i) = \frac{1 + \sin(\phi_i)}{1 - \sin(\phi_i)}\ and\ T(i) = \frac{1}{\omega_c(i)\sqrt{\alpha(i)}} \tag{6.17}$$

in which $\phi(i)$ and $\omega_c(i)$ denote the maximum phase and the center frequencies respectively. The notch filters are instrumental in canceling high frequency structural modes or suppressing sensor runouts, which could lead to amplifier saturations and instabilities. The transfer functions of notches filters are given by the following equations:

$$\boldsymbol{N} = \prod_{k=1}^{Q} \boldsymbol{diag}_k \left(\frac{s^2 + \omega^2(1)}{s^2 + 2\zeta(1)\beta_n(1)\omega(1) + \left(\beta_n(1)\omega(1)\right)^2}, \ldots, \frac{s^2 + \omega^2(5)}{s^2 + 2\zeta(5)\beta_n(5)\omega(5) + \left(\beta_n(5)\omega(5)\right)^2} \right) \tag{6.18}$$

where $\zeta(i)$ determines the rejection bandwidth and depth. $\omega(i)$ is the notch frequency and β_i decides the pole position offset. The lag compensator's transfer functions are defined in (6.19):

$$\boldsymbol{L}_g = \prod_{j=1}^{M} \boldsymbol{diag}_j \left(\frac{s + z(1)}{s + p(1)} \quad \cdots \quad \frac{s + z(5)}{s + p(5)} \right) \tag{6.19}$$

Simulation

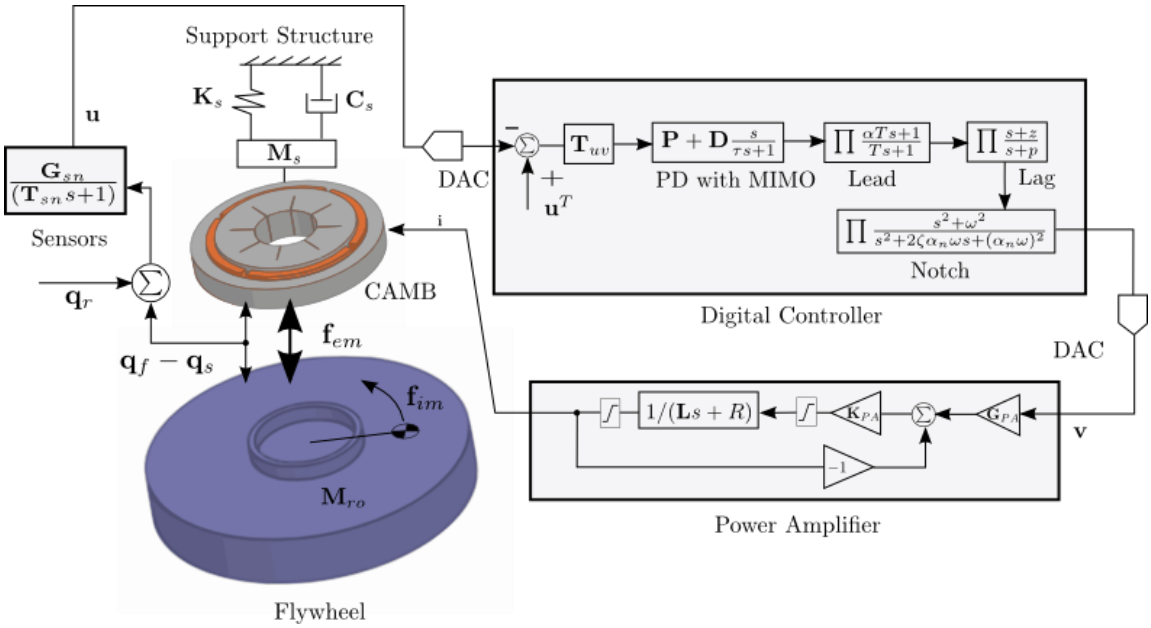

Figure 6.7 Flywheel Dynamics Simulation Schematic

As shown in Figure 6.7, Simulation platform is developed for the SHFES in Matlab/Simulink. Motor dynamics are not included since it has minimal effects on the magnetic levitation. The flywheel is assumed to be ideally speed-controlled by the BLDC motor. What needs to be emphasized is that this is a software-based simulation code. Therefore, parameters or running speed input profiles need to be pre-defined.

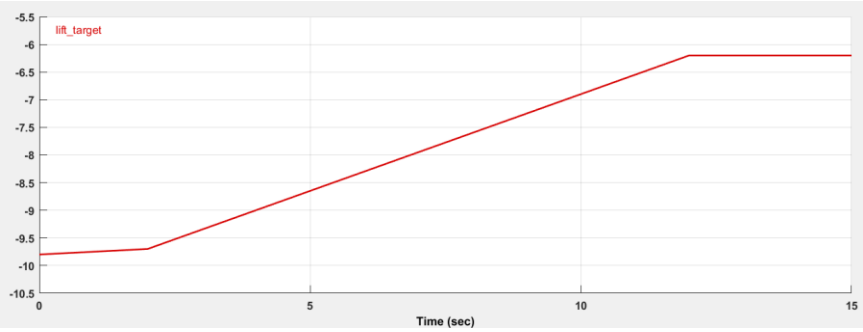

Figure 6.8 Axial Target Profile

During the levitation process, the axial target (see Figure 6.8) is set to be raised slowly to the equilibrium position to avoid excessive overshoots. A slower lag filter is given to the axial controller so that the flywheel will achieve radial levitation at first. This technique facilitates the later axial levitation. One notch per channel is used for each radial controller during lift-up. Two notches are used for the remaining channels. The axial control target must be gradually raised to 45 mils (1.1 mm) to prevent de-levitation resulted by overshoot. Because of this approach, the actual rotor will stay on the catcher bearing for several seconds (see Figure 6.9 and Figure 6.10) after the controller is turned on. This increases the demand on the axial amplifier (see Figure 6.11). But the demand quickly diminishes when the rotor loses contact with the catcher bearings. The radial actuator has the least problem during both lift-up and steady state due to their comparably less inductance. As depicted in Figure 6.12 , the axial force generated by current excitation gradually increases when the lag compensator is engaged. When it reaches the maximum value, the flywheel leaves the catcher bearing. In the meantime, the stator was pulled down

by 5 mils (0.13 mm) as shown in Figure 6.13. After the flywheel reaches the equilibrium position, the current generated magnetic force is close to zero.

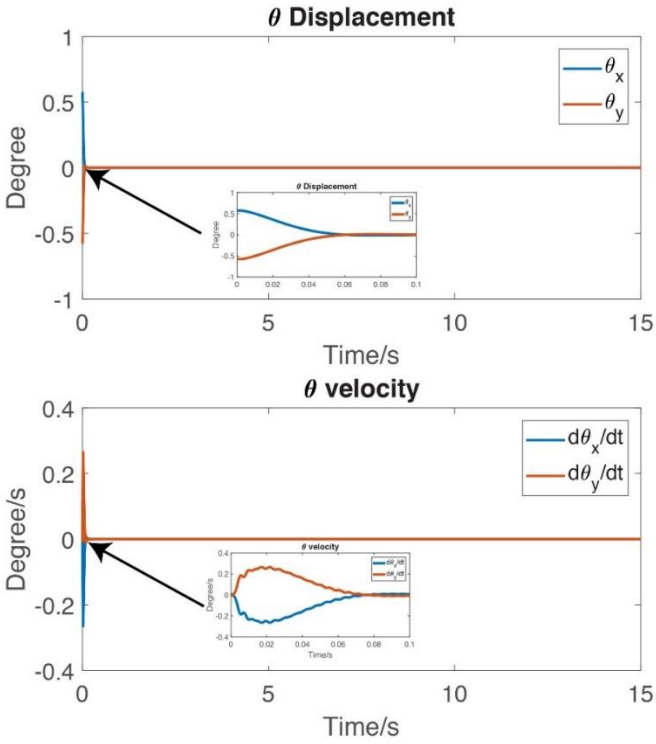

Figure 6.9 Flywheel Tilt Motions During Lift-up

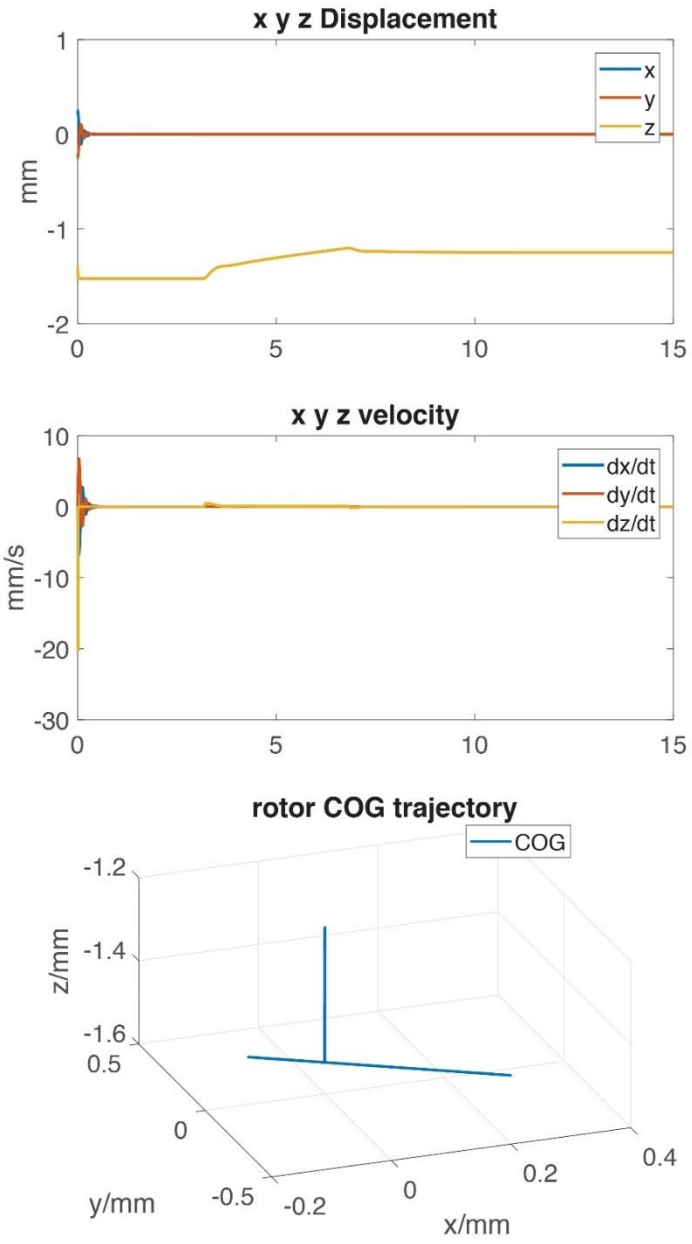

Figure 6.10 Flywheel Displacements and Trajectory During Levitation

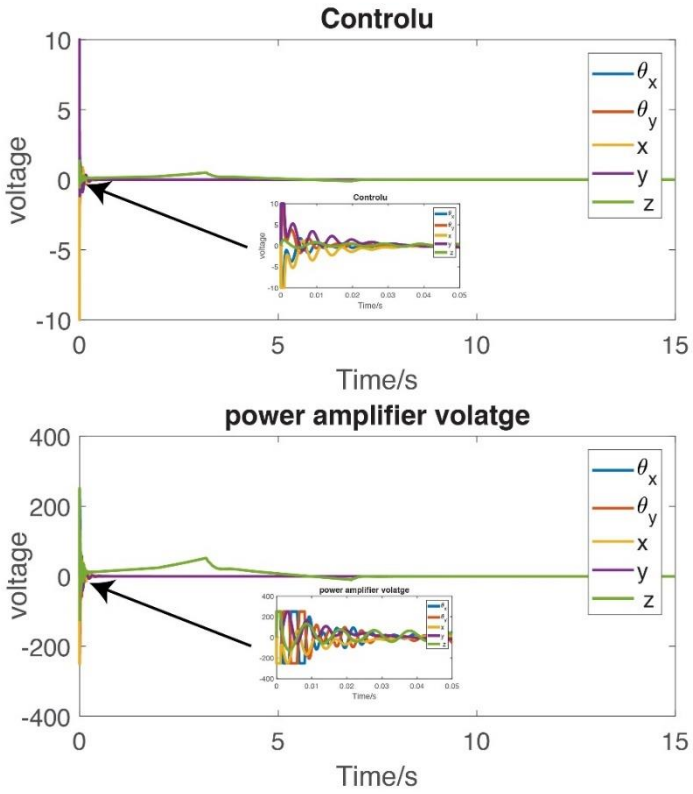

Figure 6.11 Controller Output and Power Amplifier Voltage During Lift-up

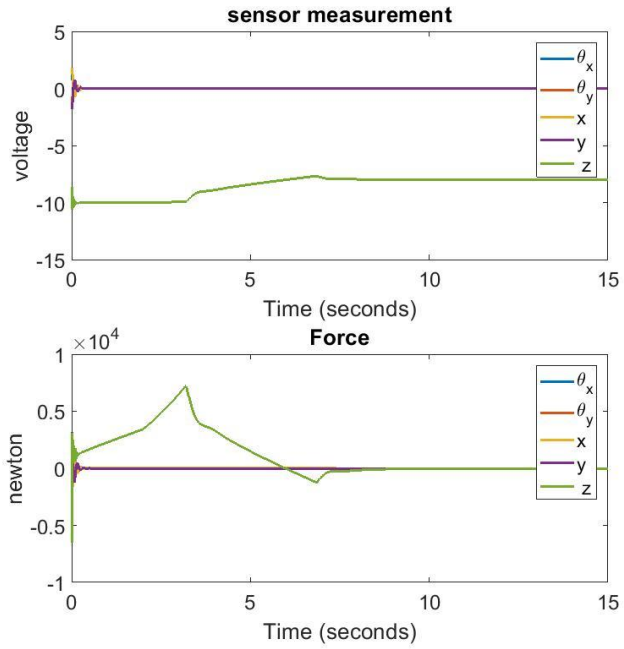

Figure 6.12 Sensor and Magnetic Force Measurements During Lift-up

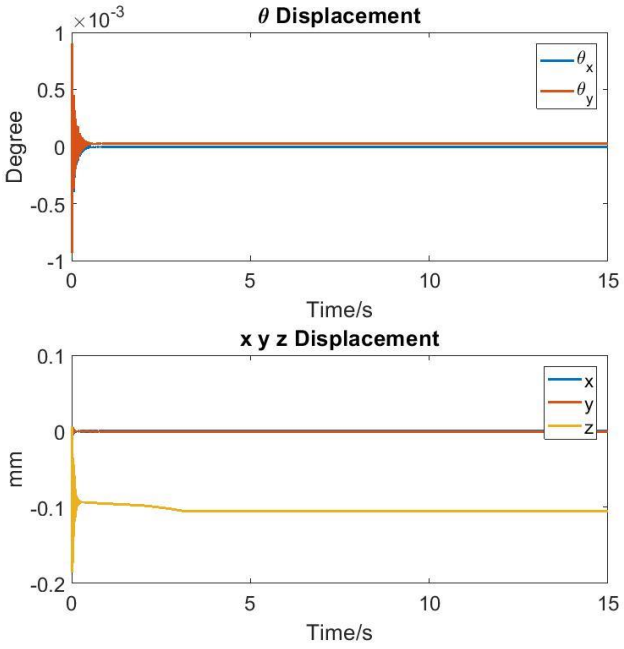

Figure 6.13 Stator Vibrations During Lift-up

Simulation of the Flywheel at High Speed

SISO Controlled High-Speed Flywheel Operation

The following simulation is carried out when the flywheel is operating at the rated 5000 RPM. To demonstrate the MIMO controller's effectiveness, it is not used at first. Instead, A SISO controller is applied. Due to the large $I_p \; to \; I_t$ ratio, the gyroscopic effect is very significant and it drives the system to unstable. The large vibrations in the $\theta_x - \theta_y$ plane is shown in Figure 6.14 and Figure 6.15.

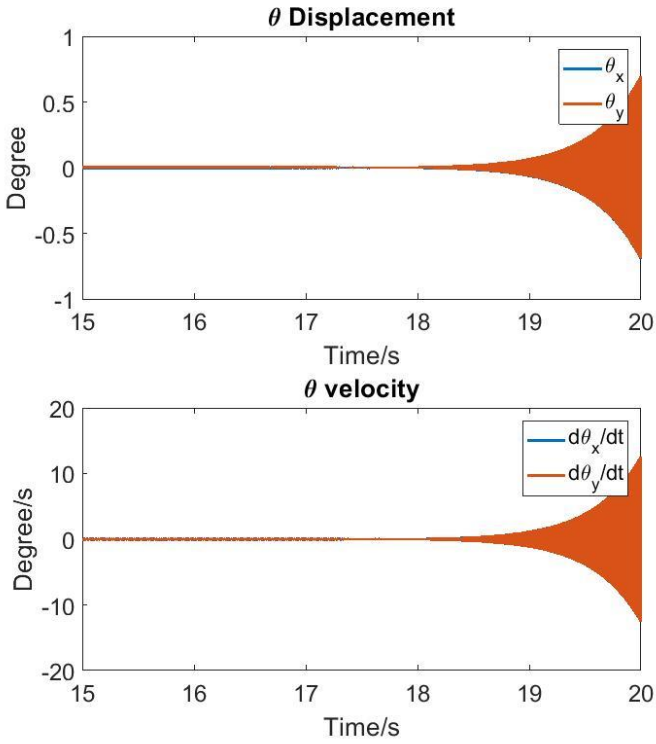

Figure 6.14 High-Speed Flywheel Attitude Vibrations (without MIMO control)

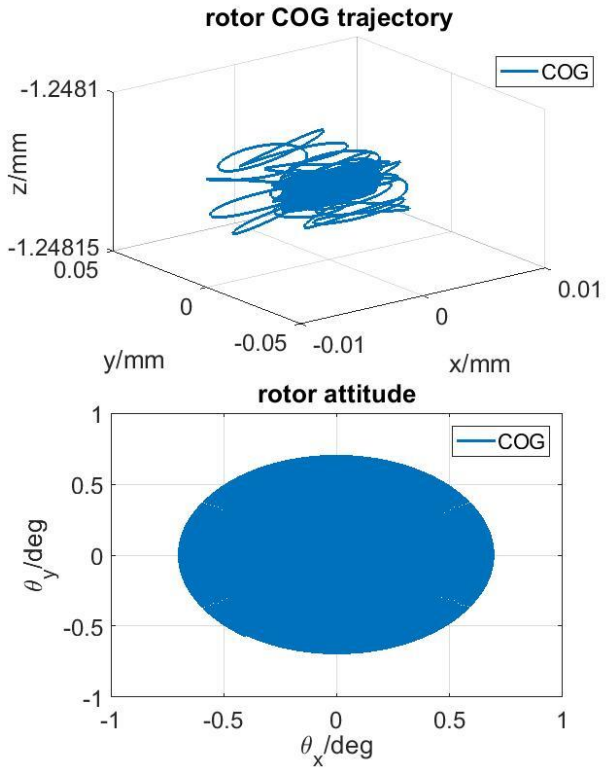

Figure 6.15 High-Speed Flywheel Trajectory (without MIMO Control)

As depicted in Figure 6.16 and Figure 6.17, SISO control caused significant amplifier voltage saturation. The controller finally failed to compensate the tilt motion after 20s. Notice that the catcher bearing system is not included in the model. Therefore the tilt motion continues to grow exponentially.

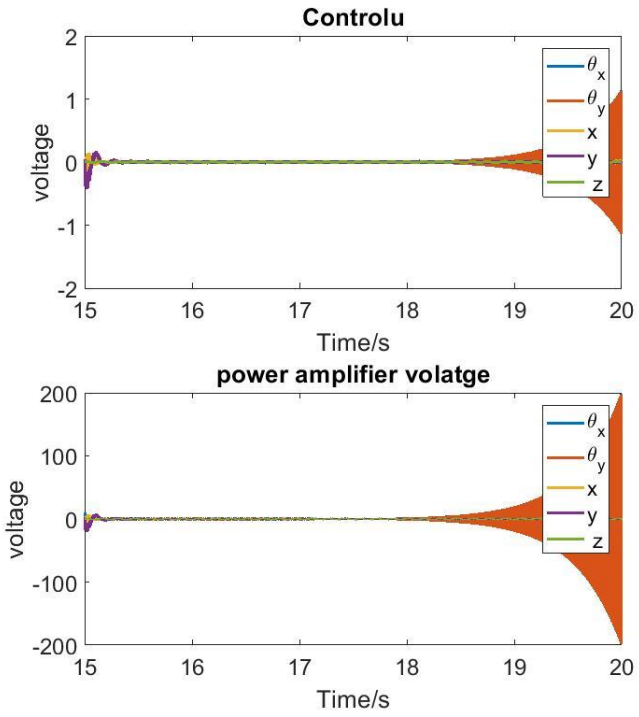

Figure 6.16 High-Speed Controller and Power Amplifier (without MIMO Control)

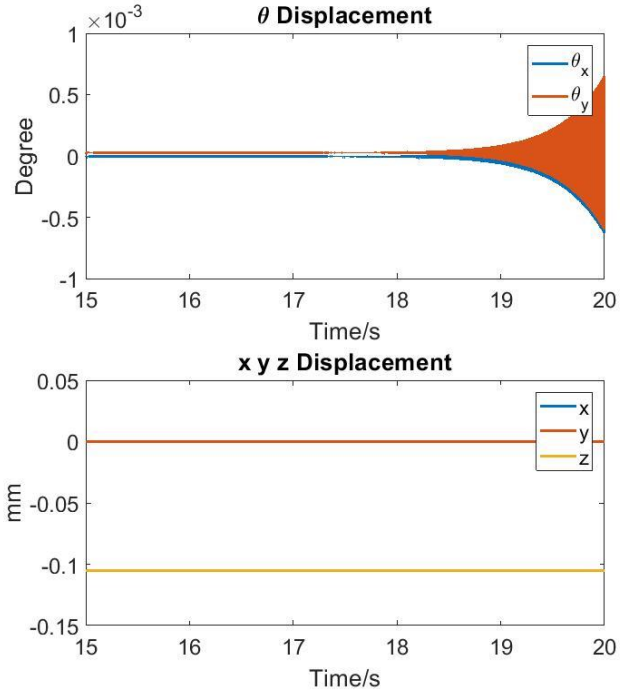

Figure 6.17 High-Speed Stator Attitude Vibrations (without MIMO Control)

MIMO Controlled High-speed Flywheel Operation

. As depicted in Figure 6.18, Figure 6.19, Figure 6.20 and Figure 6.21, with the MIMO controller applied, the flywheel is stabilized at 5000 RPM. The amplifier outputs for radial actuators oscillate in the range of less than 5v pk-pk. The remaining amplifiers will oscillate around 7v pk-pk. At least two notches are needed to deal with the runout effects, which will likely cause excessive burden on the power amplifiers and de-levitate the rotor without any mitigation. Imbalance forces are much less harmful than runout because that they only affect the radial actuator which has less inductance burden.

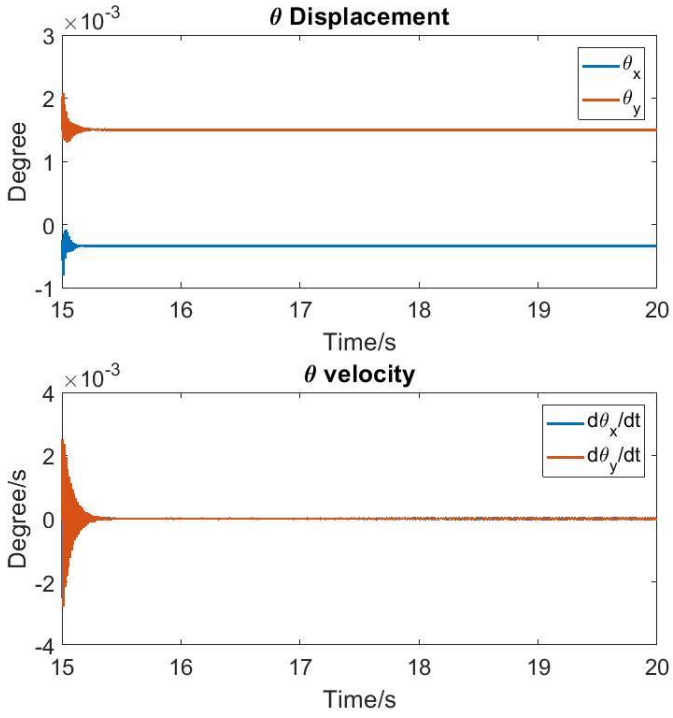

Figure 6.18 High-Speed Flywheel Attitude Vibrations (with MIMO Control)

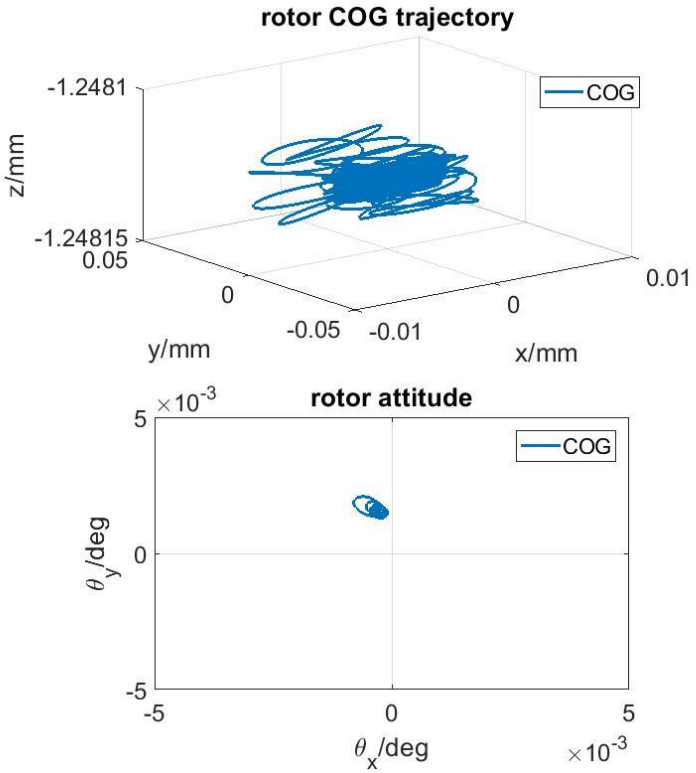

Figure 6.19 High-Speed Flywheel Trajectory (with MIMO Control)

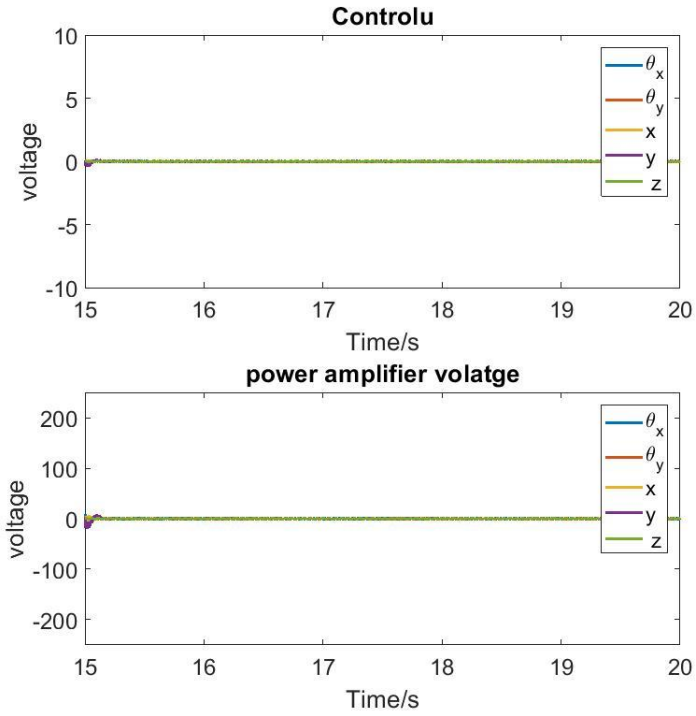

Figure 6.20 High-Speed Controller and Power Amplifier (with MIMO Control)

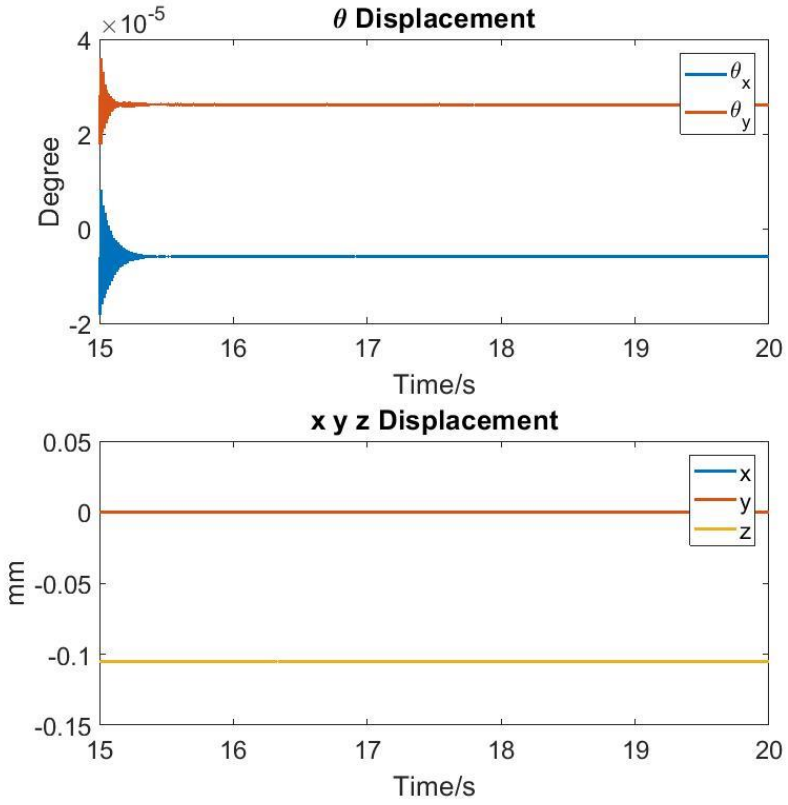

Figure 6.21 High-Speed Stator Attitude Vibrations (with MIMO Control)

Proof-of-Concept Test Rig

The small-scale test rig includes a 150lbs flywheel, preliminary C5AMB, controller/sensor, motor drive and catcher bearings. This prototype flywheel was successfully levitated in 5 axes and motored at low spin speed around 200 RPM. The controller used is a DS1104 R&D rapid development board made by dSPACE Inc. The board features a 1Ghz Power-PC based CPU, 8 A/D and D/A channels and a slave DSP. The digital solver is set to 50k interrupts per second (as for per control cycle). The motor controller is implemented on a separate TI DSP board. The controller is connected to a communication card which connects to the PC through PCI bus. The controller further

connects to an instrument panel through cables to receive sensor inputs and give command signals to the power amplifiers. Motor coils are attached to curved plexiglass sheets, which are bracketed to the upper plate. As shown in Figure 6.22, the segments hang in a groove with permanent magnets near the outer edge. Each coil has a lead wire that connects them in series. The current output for maintaining axial levitation is about 3 to 4 amperes. For the radial part, current output is about 2 to 3 amperes. The measured coil temperature is around 105 Fahrenheit with fan cooling. The prototype experiments have provided valuable experiences for building the six-ton, 100 kWh flywheel system.

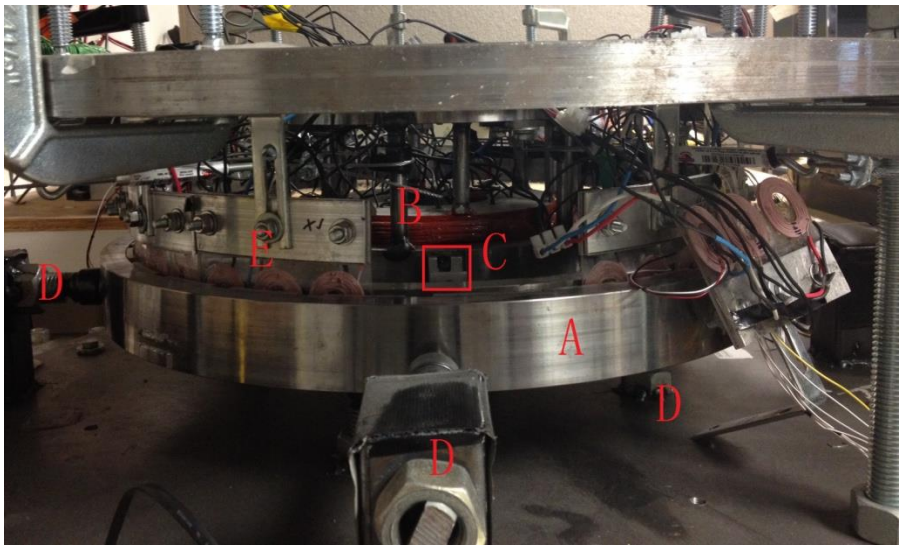

Figure 6.22 Small-Scale SHFES Test Rig

Note: A-Shaftless Flywheel, B-AMB, C- Sensor, D-Catcher Bearings, E-Motor Coils. One of the motor segments is taken out to give a better view of the AMB.

CHAPTER VII

FABRICATION AND TESTING OF THE SHFES*

Flywheel Testing Center

As shown in Figure 7.1, a dedicated facility was built for testing the 100 kWh SHFES. A 10-foot-deep pit is built for placing the flywheel. The pit is lined with a soil retainer wall, which would be penetrated in the event of a flywheel burst, allowing the surrounding soil to capture the energy in a relatively harmless manner. The location is at a remote site away from the main campus. The fabrication process of the SHFES took about 3 months. Some of the key procedures are depicted in Figure 7.2, Figure 7.3, Figure 7.4, Figure 7.5, Figure 7.6, Figure 7.7, Figure 7.8 and Figure 7.9.

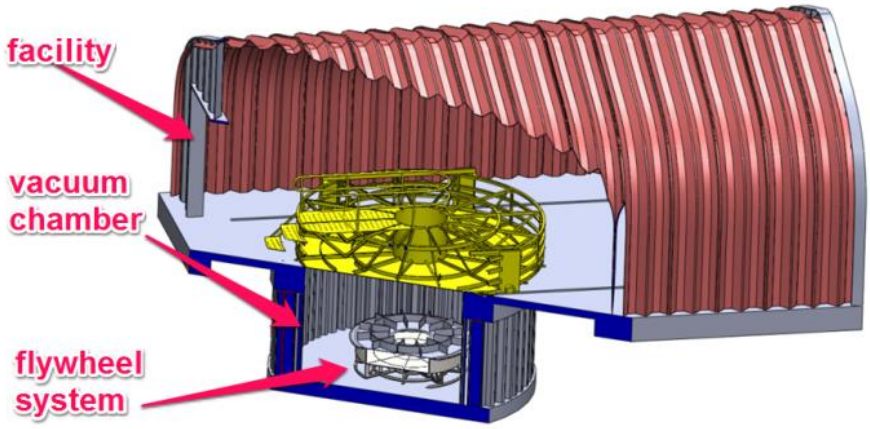

Figure 7.1 Cutaway View of the SHFES Test Center

*Part of this chapter is reprinted with permission from "A coreless permanent-magnet machine for a magnetically levitated shaft-less flywheel" by B. Anvari and X. Li, 2017., *2017 IEEE International Electric Machines and Drives Conference (IEMDC),* Copyright [2017] by IEEE.

Fabrication of the SHFES

Figure 7.2 The SHFES and Its Supporting Structure

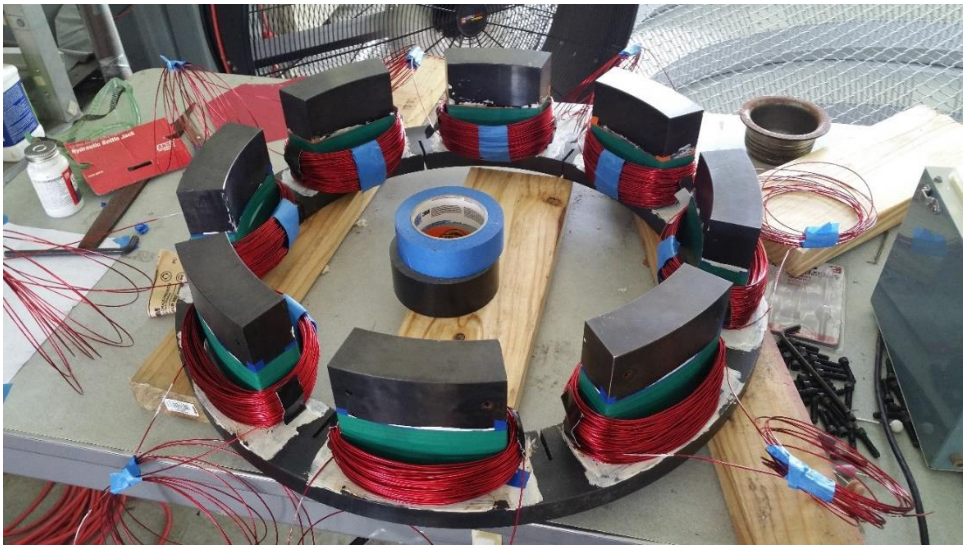

Figure 7.3 Installation of the Radial Coils

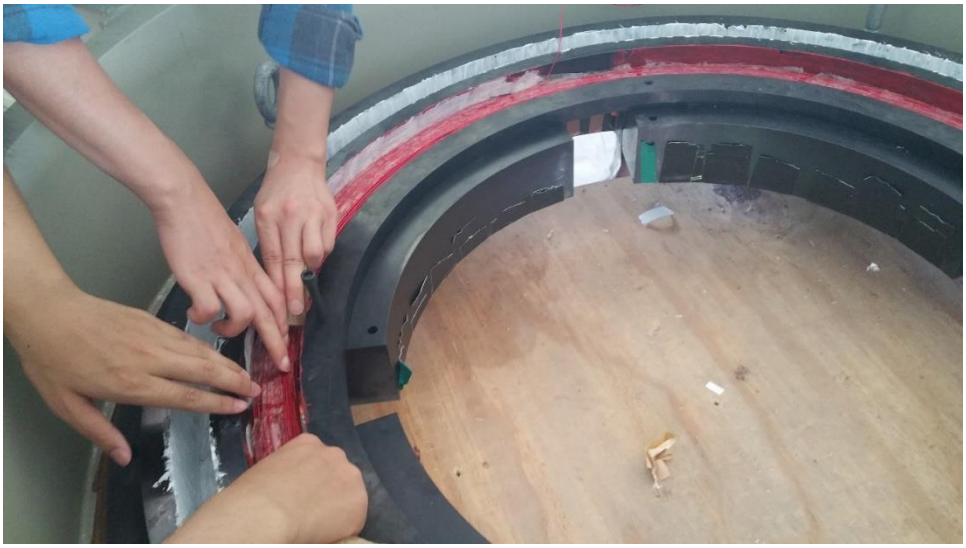

Figure 7.4 Installation of the Axial Coils

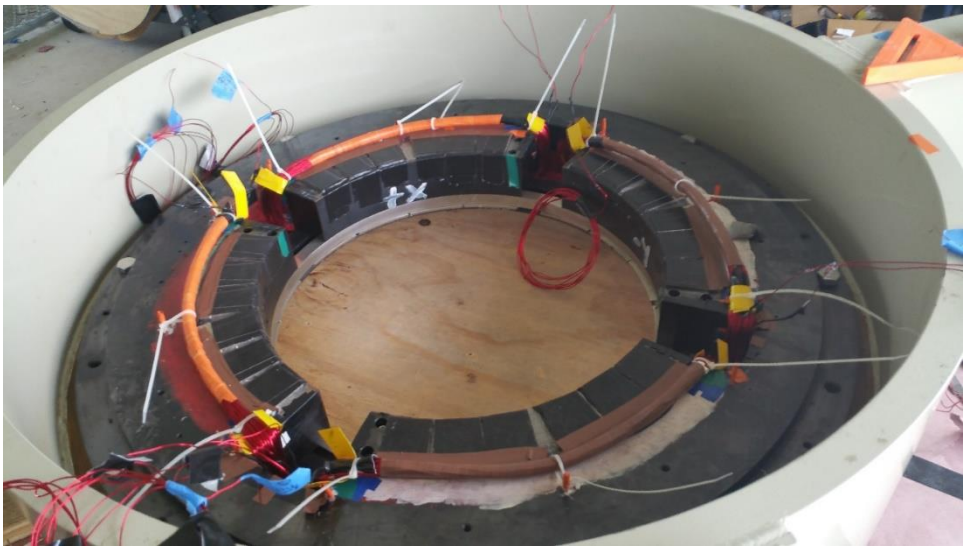

Figure 7.5 Installation of the Tilting Coils

Figure 7.6 Installation of the Upper Permanent Magnets

Figure 7.7 Installation of the Bottom Permanent Magnets

Figure 7.8 Final Assembly of the C5AMB

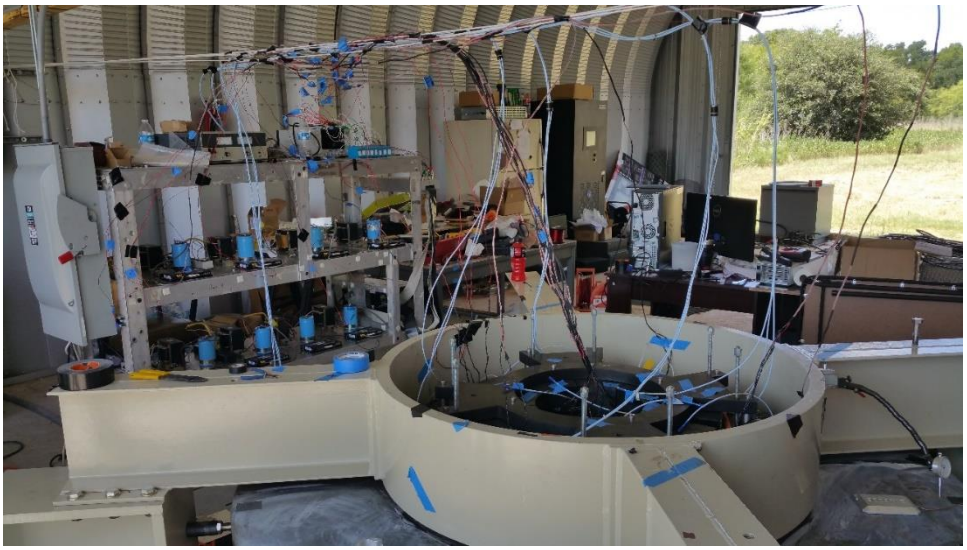

Figure 7.9 Overview of The SHFES-C5AMB

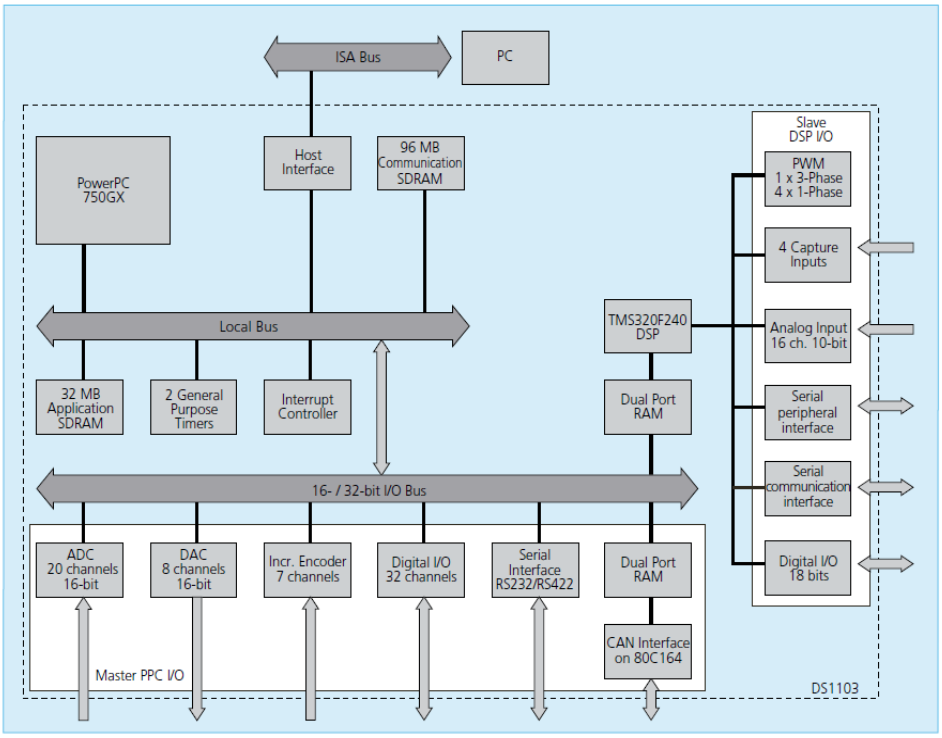

Figure 7.10 dSPACE 1103 Processor Hardware Architect, reprinted from [72]

The feedback algorithm is implemented on dSPACE's RTOS system (see Figure 7.10) with an HMI operable via a PC. The compensators are implemented in Simulink time-domain structures with integrators. The integrator solver is set to discrete modes such as ode4. The solver step size and solver type are adjusted to balance between controller performances and overrun risks.

Flywheel Levitation Test

Based on the system dynamics simulation implemented in MATLAB/Simulink, the control parameters are derived and then fine-tuned during the onsite testing at the facility. The levitation test is carried out in two steps: At first, the flywheel is controlled radially while it is still vertically supported by the ball transfers. This technique facilitates the axial levitation later because that the C5AMB's axial magnetic flux distribution also relies on its radial position. As depicted in Figure 7.11, the flywheel is at first controlled radially to move from its initial position (-0.42 mm, -0.31 mm) to an intermediate position at (0.04 mm, -0.09 mm) before it finally reaches the geometric center (0.19 mm, - 0.04 mm). Figure 7.11 shows that there are steady state control currents when the flywheel reaches its radial center. These currents are compensating the inevitable manufactural and assembling inaccuracies, which causes the flywheel to experience PM pulling force at its geometric center. The gravity force may contribute in the radial directions as well since the flywheel is not perfectly leveled. Once the flywheel reaches its radial targets, the axial control is then switched on, and the reference signal is gradually raised to the target value of 1.13 mm to prevent de-levitation resulted from a large overshoot. As illustrated in Figure 7.12, the axial control current goes up to 8A to lift the flywheel at the starting air gap of 2.33 mm. Once it's off the ball transfers, the control current begins to drop gradually as the flywheel approaches its target. At the steady state, the air-gap between the flywheel and the C5AMB is about 0.1 mm larger than the magnetic equilibrium. The flywheel is set to stay slightly below the neutral position to prevent it from jumping and damaging the C5AMB in case of power shortage. As a result, there is about 1.87 ampere

of steady-state axial current for providing partial lifting force while the majority of the flywheel's weight is suspended by the PM-generated pulling force. The tilting coils are used for merely maintaining the flywheel's leveled orientation during the axial levitation.

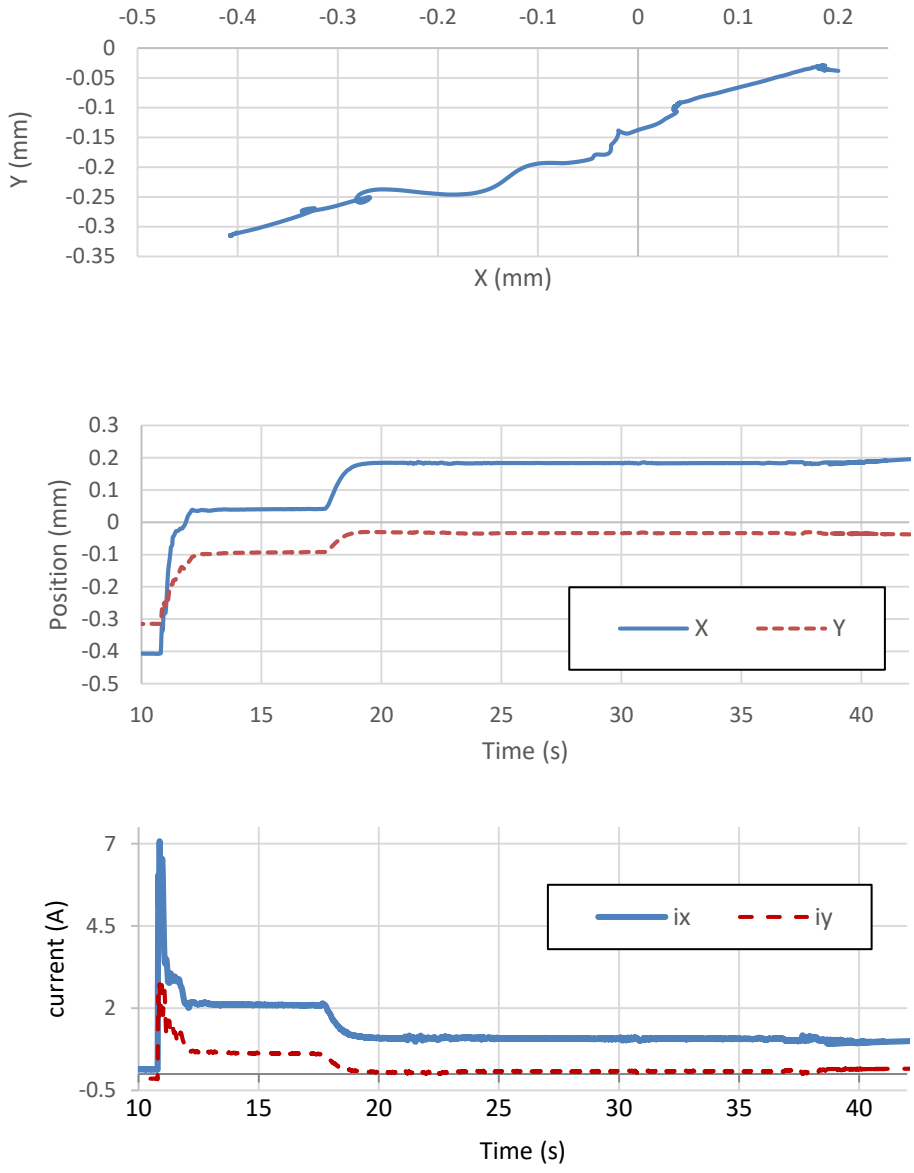

Figure 7.11 Measurement of Position and Current Signals During Radial Levitation.

Note: The Radial Targets are Set Per the C5AMB's Geometric Center.

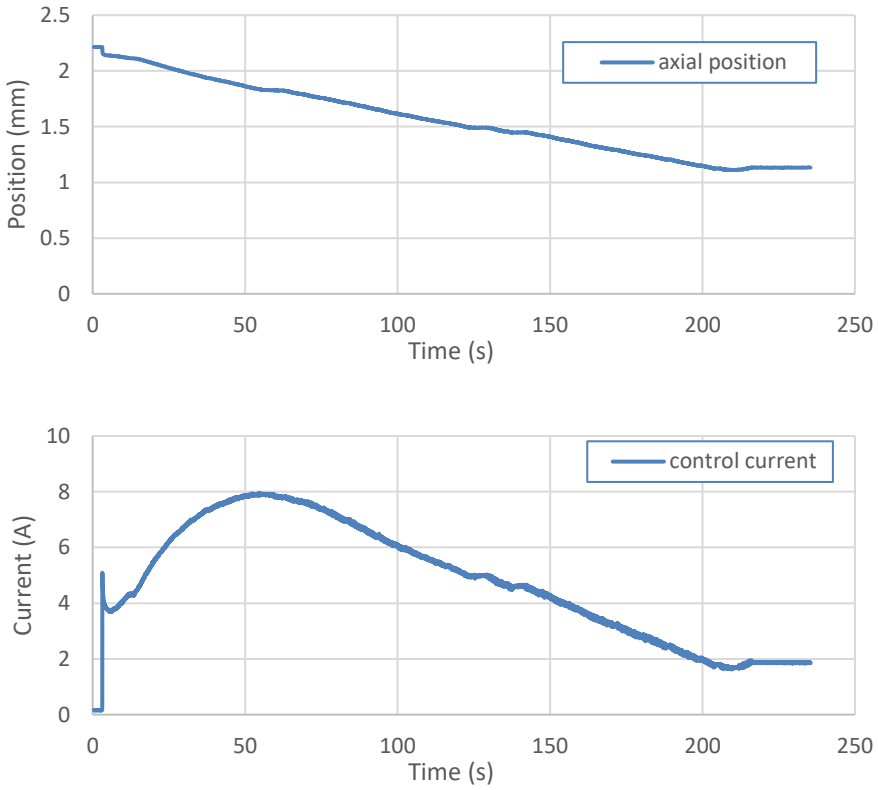

Figure 7.12 Measurement of Position and Current Signals During Axial Levitation.

Note: The Target Signal is Gradually Moved to 1.13 mm

Controller Parameters for Levitation

For the tilt controller, the experiment settings have similar DC gains but lower derivative gains compared to the simulation ones. In general, it is found that the notch filters for the structures modes are not necessary for practice. However, extra notch filters at 238Hz and 383 Hz are added to mitigate the flywheel's bending mode. The radial control parameters used in simulation and experiments matches well. For the axial control, the experimental parameters have reduced derivative gains due to the sensor noises.

Figure 7.13 Flywheel Controller HMI: Control Panel

Testing of the C5AMB

Along with the SHFES, the C5AMB is fabricated, assembled and tested. While the flywheel is being levitated, position and current stiffness are measured per the following steps. Firstly, a load cell with flexible support is used to apply external forces to the flywheel and to record the reaction force. In the meantime, lag compensator of the AMB controller is switched on. Because of the lag compensator, the flywheel is controlled at its magnetic equilibrium position. Figure 7.13 shows the control panel for magnetic levitation operation. Figure 7.14 depicts one of the AMB test setups.

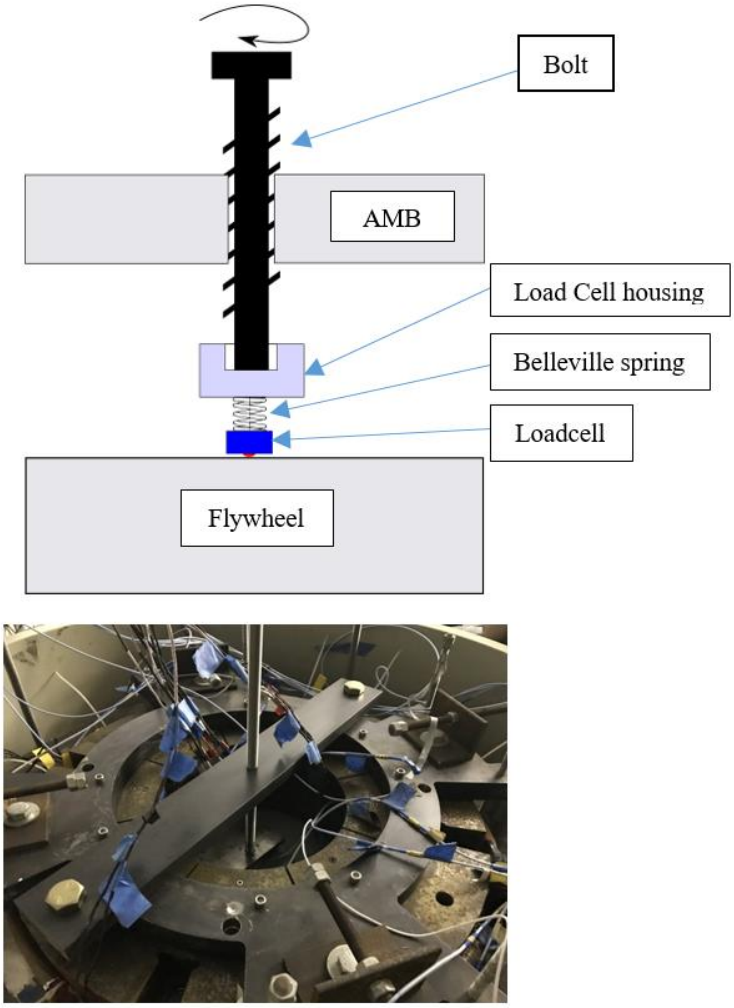

Figure 7.14 AMB Testing Set-up for Axial Stiffness Measurements

Stiffness coefficients are acquired based on the following equation:

$$f_{re} = K_i \Delta i + K_p \Delta p \tag{7.1}$$

During the current stiffness measurement, the recorded flywheel position is close to zero ($\Delta p = 0$), f_{re} is the recorded reaction force and Δi is the recorded current. For the measurement of the position stiffness, the load cell support is replaced with a rigid structure and, all the lag compensators are turned off. A new set of data for force, current, position is recorded. In this case, the displacements are not zero ($\Delta p \neq 0$). Along with the

acquired current coefficients (K_i), the position stiffness (K_p) is derived by solving equation (7.1) .

As depicted in Figure 7.15, the measured position-to-force/moment data is compared with FEM and EMCM simulation results. Notice that the axial force is the summation of recoded force and flywheel's weight. With regret, the range of measurement is confined by the limited load cell capacity and PA current output. Notably, during the measurement of position stiffness, feedback control current generated force takes a significant portion of the load cell capacity. Due to this reason, axial position stiffness is only evaluated between .02mm and .08 mm of increment to the air gap. A further increase of external force will cause the axial coil to overheat. Nevertheless, the testing results are still useful for modeling and controller design since the flywheel will be controlled near the equilibrium position during operation. The results show satisfying stiffness that is in general consistent with the simulation estimation. In addition, the force/moment-to-position measurements follow a linear pattern, which is crucial to the flywheel's high-speed control. The measured current-to-force/moment data is depicted in Figure 7.16. Again, they are in good agreement with either FEM or EMCM estimations, and it shows good linearity.

The position and current stiffness are summarized in Table 7.1. Notice that the axial stiffness of the EMCM and FEM are also evaluated in a smaller range. The difference between measured and FEM axial position stiffness is only about 4% whereas the difference between measurements and EMCM has a somewhat 10% higher estimation. Similarly, the tilting position stiffness of FEM and measured data are closer to each other

(within 20%) than the EMCM estimation. For the radial position stiffness, the FEM and EMCM estimations are within differences of 20% and 10% compared to the measured one. Figure 7.16 shows the current stiffness measurements that cover a more extended range and show good agreements with simulation results. For axial current stiffness, the difference is within 12%. For the radial current stiffness, the EMCM is giving 20% higher estimation than the FEM and testing results. Tilting pole's current stiffness has the smallest difference of less than 6% between the measurements and simulations.

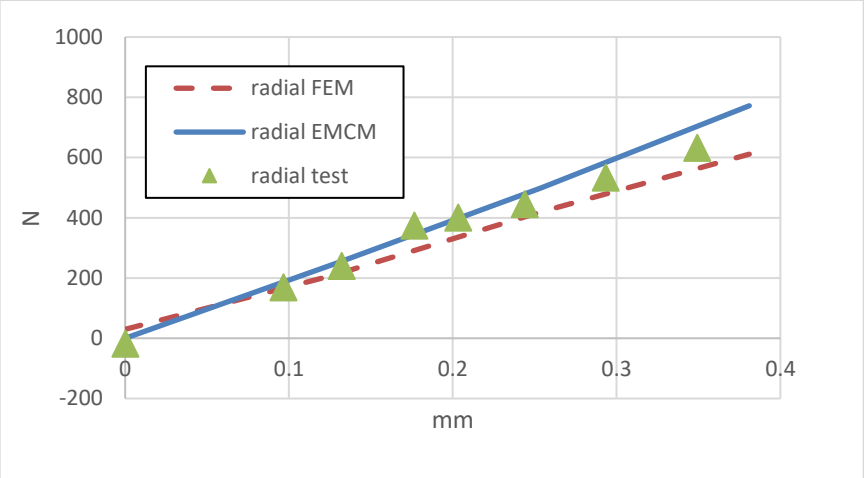

(a)

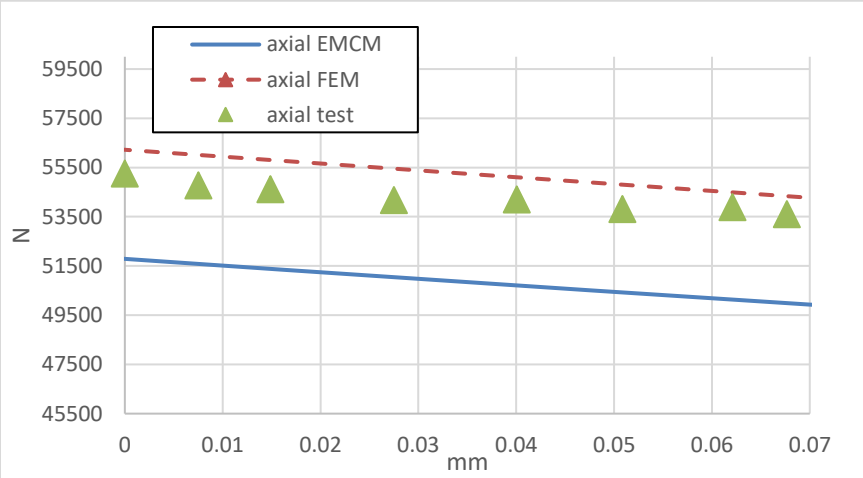

(b)

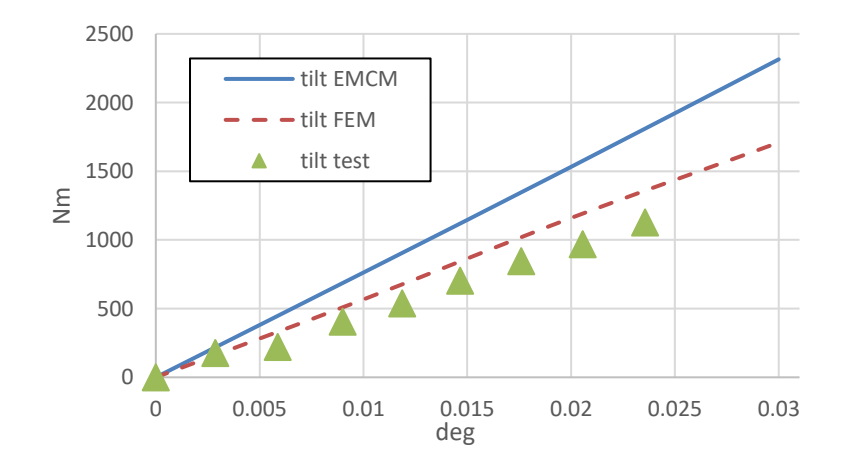

(c)

Figure 7.15 The Measured Force/Moment vs. Position/Attitude

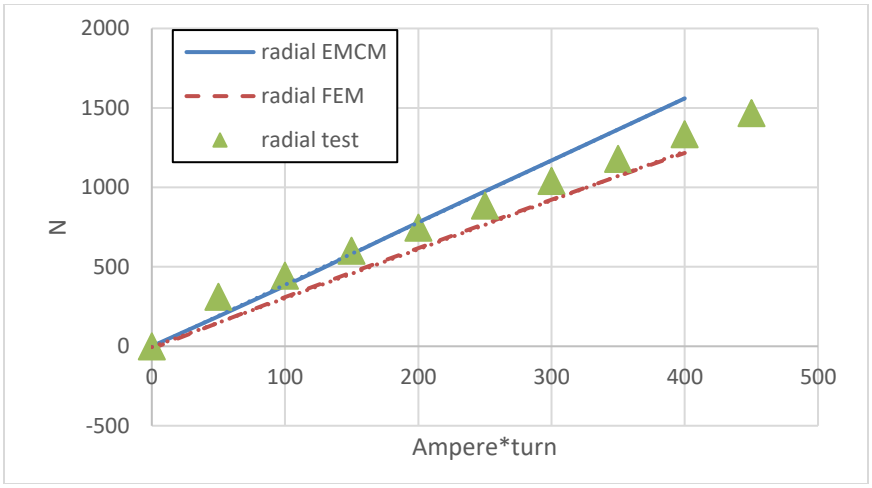

(a)

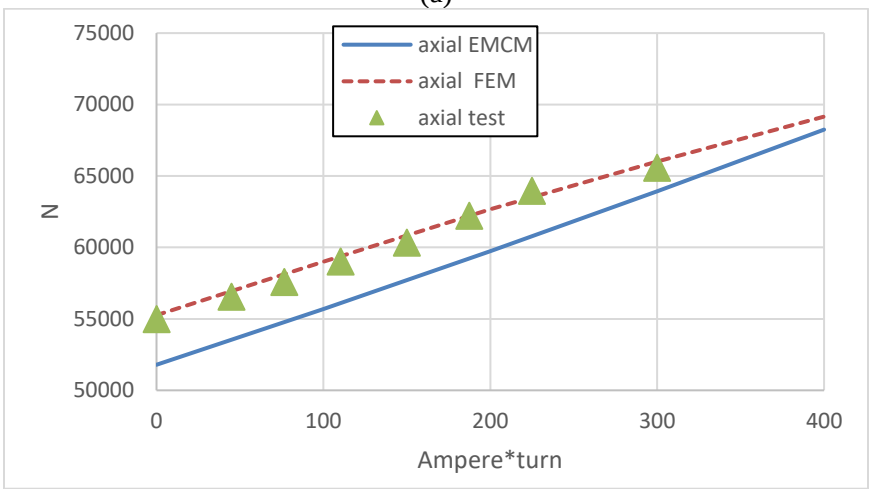

(b)

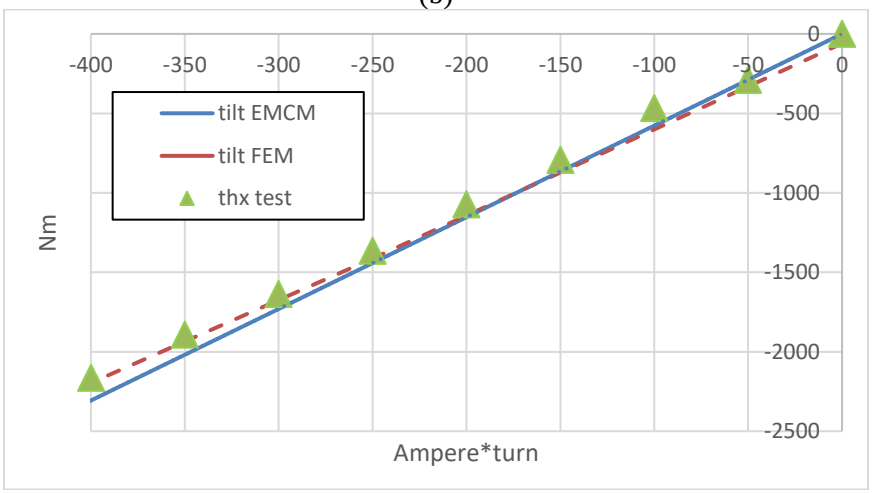

(c)

Figure 7.16 The Measured Force/Moment vs. Current Excitations

Experimental results demonstrate that the magnetic bearing can provide levitation for the 5443-kg flywheel at an air gap around 1 mm with minimal current consumption. In addition, current and position stiffness measurements of the C5AMB shows good agreement with the simulations. The acquired results are useful in the modeling of the flywheel levitation control under high speed as well as in motor control.

TABLE 7.1 CURRENT AND POSITION STIFFNESS

Stiffness		Axial	Tilting	Radial
current	*EMCM*	4114 (N/A)	576 (Nm/A)	390 (N/A)
	FEM	3480 (N/A)	533 (Nm/A)	308 (N/A)
	test	3714 (N/A)	546 (Nm/A)	343 (N/A)
position	*EMCM*	- 28211 (N/mm)	-77134 (Nm/deg)	-2023 (N/mm)
	FEM	- 24988 (N/mm)	-57200 (Nm/deg)	-1539 (N/mm)
	test	-25987 (N/mm)	-47762 (Nm/deg)	-1858 (N/mm)

Modal Testing of the Flywheel

The flywheel's flexible modes are acquired during the levitation. Also, these modes (see Figure 7.17) are compared with FEM simulations (Figure 7.18) for verification purpose. The modes are summarized in Table 7.2. All modes are well above the flywheel's operational speed range, which is between 42 Hz to 84 Hz. The 1st bending has some effects on the tilt control. It was found that a notch filter may need to be applied for this mode if the flywheel does not start levitation from a relative leveled initial state. For the 2nd bending modes, which affects the tilt and axial controller, notch filters are needed during the lift-up process and for maintaining a stable levitation. For the rest of the modes, they do not show any noticeable impact on the magnetic levitation.

TABLE 7.2 FLYWHEEL FLEXIBLE MODES SUMMARY

Mode Number	Measured Frequency (Hz)	Frequency FEA (Hz)
1	230	224
2	383	383
3	502	491
4	802	799

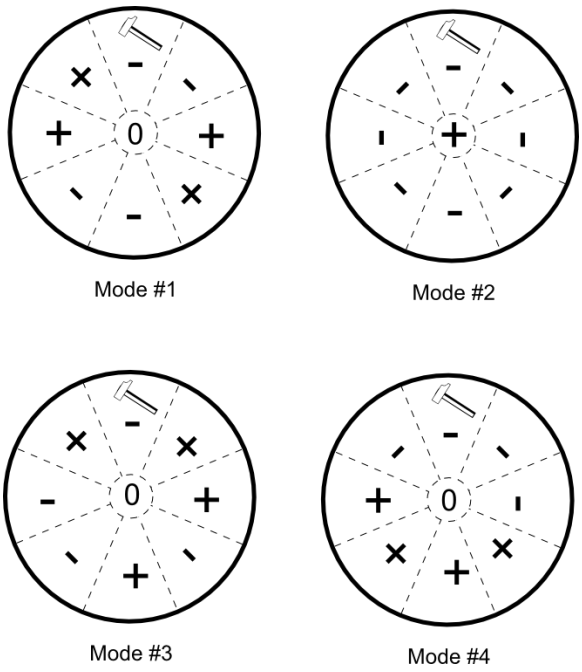

Figure 7.17 Measured Mode Shapes

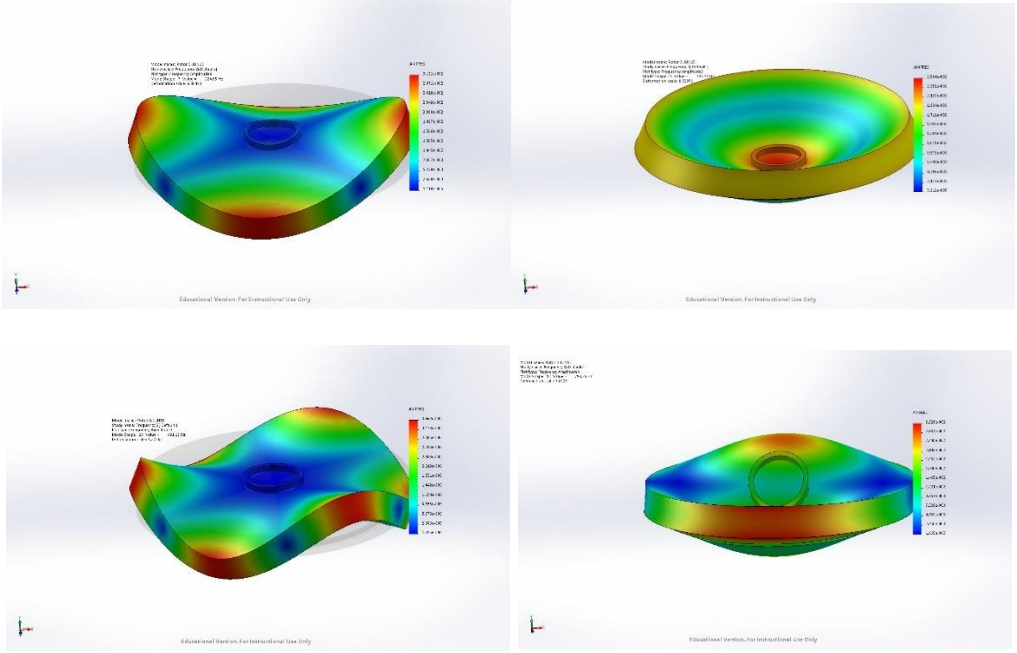

Figure 7.18 Modeshape by FEM Simulations

Development and Test of the Preliminary Motor/Generator

The motor design is summarized in [51], it is a 64 pole, coreless, brushless PM motor. Its power rating is 100KW. Due to the sheer size of the flywheel and the use of 4340 for higher yield strength. The motor has relatively low torque density. However, the core-less design allows a robust coil-holding structure.

Figure 7.19 Coil Holder Assemblies Installed Underneath the Flywheel.

As depicted in Figure 7.19, the coil holders are made of structural steel and designed to be adjustable. The based plates are directly bolted to the ground. A single holder assembly includes three-phase coils, which are potted together with compounds to provide a better electrical resistance and thermal conductivity. Due to the coreless design, the force applied

to the winding must be examined. An efficient holding structure will prevent the magnetic field force from causing excessive deflections. The radial, tangential and vertical forces are calculated by FEA. Figure 7.20 depicts the force applied to the winding in the cylindrical coordinate system at a rated current of 210 A. The applied force peak value is 100 N in the radial and is 120 N in the tangential directions. The force is also calculated at 1928 rpm, where the highest current of 300 A is supplied. In this case, the peak forces in the radial and tangential directions are 200 N and 300 N, respectively. One coil support structure consists of two L-shape brackets made of plain carbon steel. The upper bracket has unthreaded holes for inserting the fasteners. The lower bracket has two matched slots. The coils can be moved upward or downward by adjusting the amount of overlap between the two brackets. Each of the upper coil holders supports three coils, each of which carries the current for a single phase. As depicted in Figure 7.21 and Figure 7.22, static FEA analysis shows that when the flywheel is operating at 1928 rpm, the holder experiences 31 Mpa of stress and 0.83 mm of deformation in the radial direction, which are acceptable given an air gap of 10.5 mm. The stress level is also under the material's yielding point, which is typically 250 Mpa or higher. The structure is stiffer in the tangential and vertical directions. The maximum Von Mises stresses and deformations under peak current are only 27 Mpa/0.39 mm for tangential load and 5.3 Mpa/0.19 mm for axial load,

When the flywheel is operating at 5000 rpm, due to the reduced current, the radial stress level and deformation drop to 14 Mpa and 0.39 mm which is only 3% of the air gap. The tangential and vertical loads cause 22 Mpa/0.32 mm and 8.5 Mpa/0.16 mm of maximum stress and deformation.

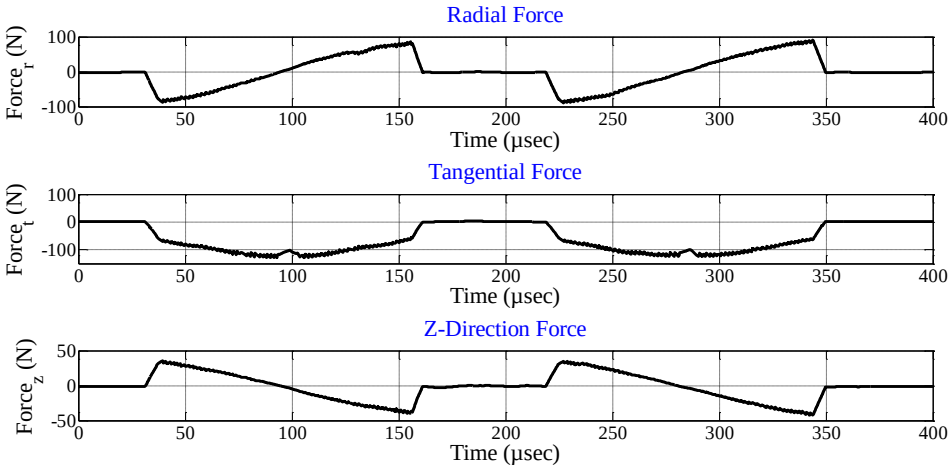

Figure 7.20 Force on the Coils at 210 A.

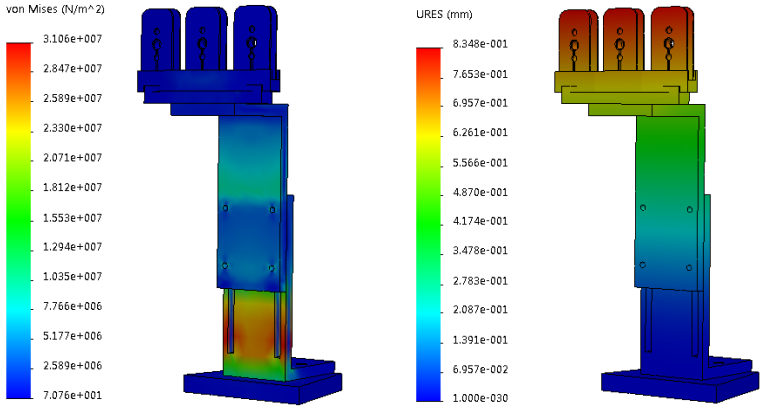

Figure 7.21 Coil Holder Radial Stress and Deformation: Motor Current 300 A.

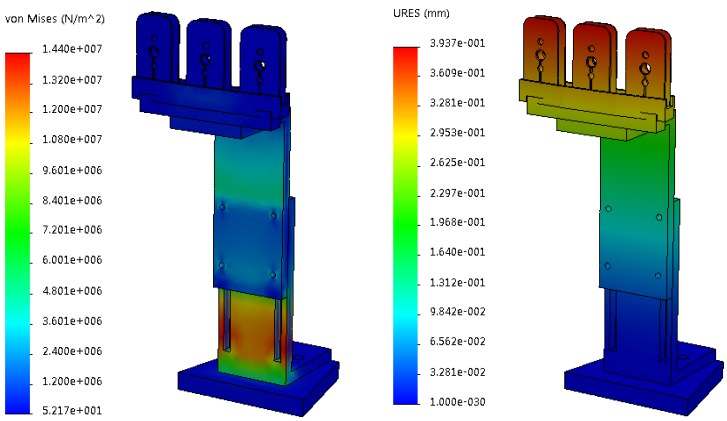

Figure 7.22 Coil Holder Radial Stress and Deformation: Motor Current 210 A.

Figure 7.23 The Potting Assembly Includes Three Coils, One for Each Phase.

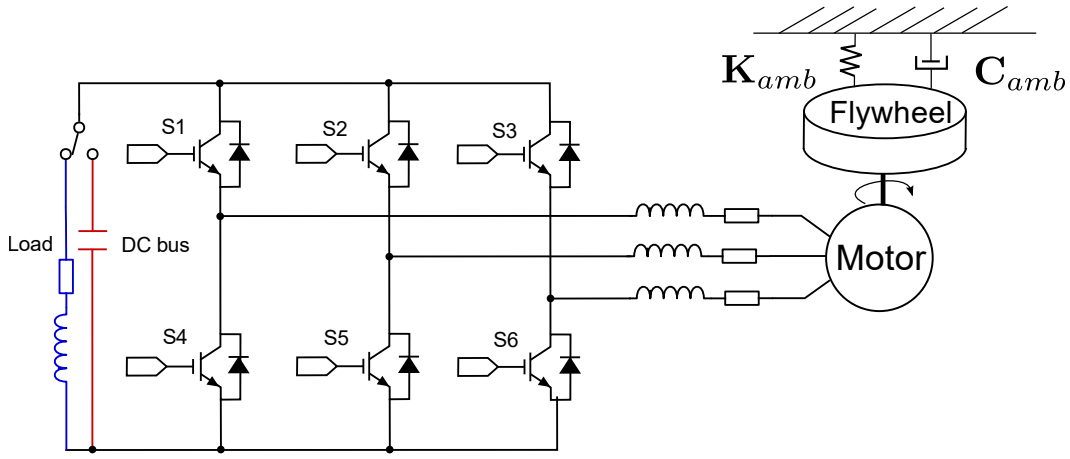

Figure 7.24 Motor Wiring Scheme During Charge and Discharge.

The potting assembly is depicted in Figure 7.23. The motor/generator (see Figure 7.24) is tested with a Coley Control Xenus-230-36 drive, which can provide 12A/36A continuous/peak current. The PWM switching frequency is 10Khz. The coils are measured to determine their electrical properties such as resistance and inductance. The drive is then autotuned to achieve a current loop bandwidth of 1.3KHz. The current loop proportional and integral feedback coefficients are 1284 and 267. During the initial test, the flywheel is motorized in an open-loop drive mode. Due to multiple factors including the large rotor size, limited drive capability, the presence of eddy current loss, and the lack of feedback control, it takes a relatively long time to drive the flywheel to a low speed.

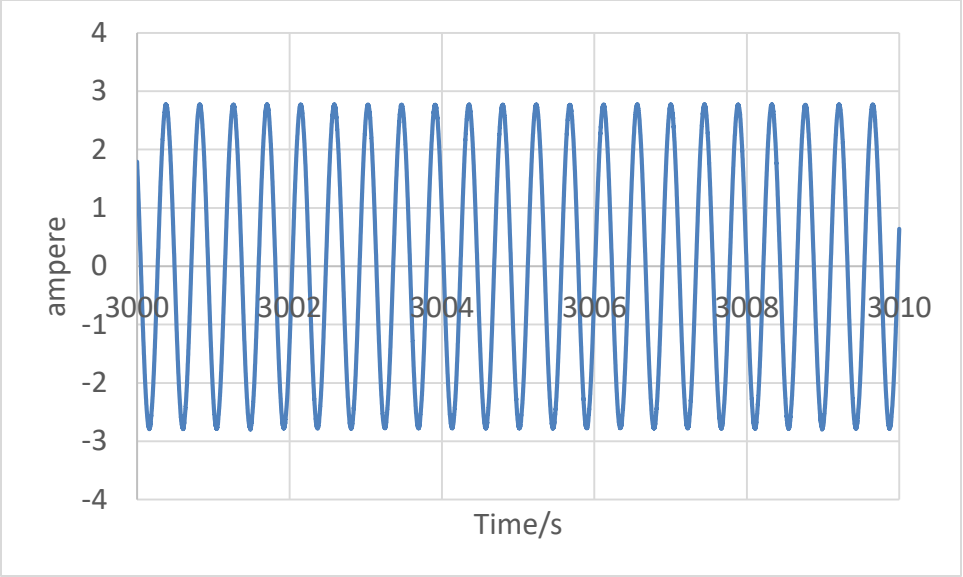

Figure 7.25 The Motoring Current at Charge Mode (Single Phase).

During the charging mode, the drive current is limited to ±5 A (see Figure 7.25). AIt takes about 80 seconds for the flywheel to be fully discharged in the regeneration mode. As depicted in Figure 7.26, the single-phase current decreases from 1.7 A to almost 0 as the flywheel slows down. Again, eddy current loss has played a role in dissipating energy.

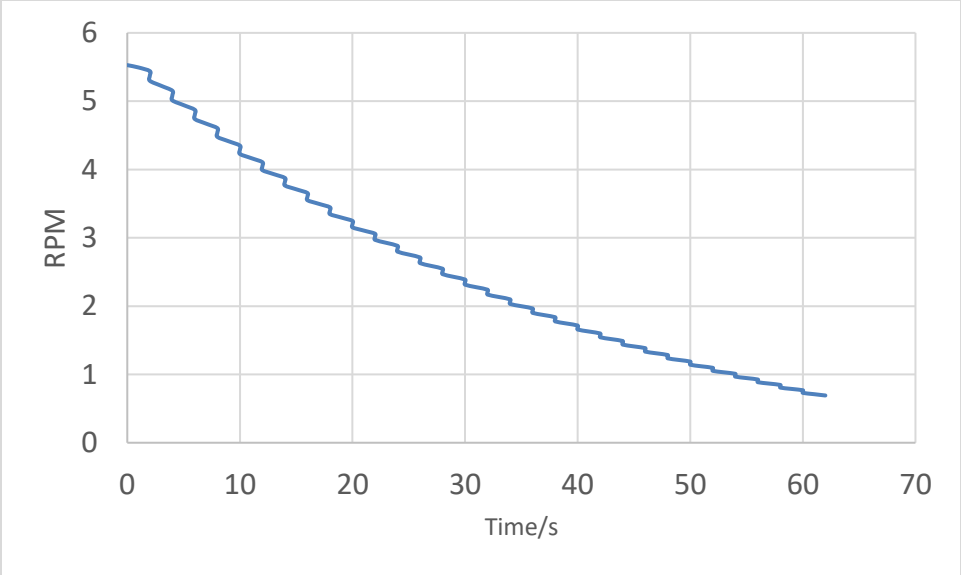

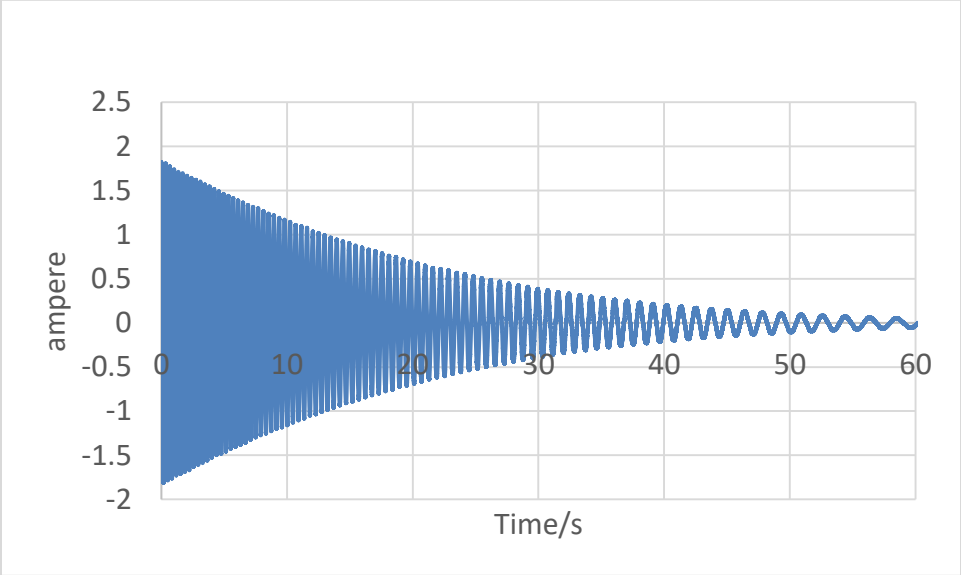

Figure 7.26 The Regeneration Mode: Flywheel Speed and Discharge Current

CHAPTER VIII

CONCLUSIONS AND FUTURE WORK

The design and development of an innovative, state-of-the-art FESS are represented. The SHFES introduced in this dissertation is aimed at providing a more commercially viable flywheel energy storage technology for utility applications. In addition to the innovative shaftless flywheel and C5AMB design that yields a high energy and power capacity. The SHFES also utilizes low cost and readily available high strength steels as the building materials, making it a considerate advancement of the state-of-art flywheel technology. The significance of it is summarized by following:

1. A shaftless, hubless, high strength steel flywheel with doubled energy density compared with a conventional HSS flywheel. It provides competitive specific energy and superior energy density to LCFM flywheels.
2. A single C5AMB capable of 5-DOF levitations.
3. Successful assembly, magnetic levitation control of the shaftless flywheel with the undersize and solid-core C5AMB.
4. Preliminary motor development and test of motor/regen for the FESS.
5. Synthesis and formulation of a high fidelity model for the C5AMB-SHFES and design of a MIMO control scheme to stabilize the system under the rated speed.

The next step is the high-speed test of motor/regeneration. To demonstrate its performance, The SHFES should be tested with variable electrical loads or renewable energy resources. It is necessary to pair the motor/generator with a more capable drive. The high-speed test will also require the use of MIMO control [73] for the C5AMB. Fine-

tuning gains for different speed experimentally to travel through critical speed is another challenging task. Also, the flywheel's imbalance must be compensated so that it meets a fine balancing grade. The C5AMB can be used to balance the flywheel automatically. Other future works include: To further reduce the costs of SHFES: The prototype system has a relatively high-cost and CPU based controller. Because that the nature of the AMB and the motor controls require multichannel feedbacks. FPGA (Field Programmable Gate Arrays) can provide a cost-effective and high-performance controller solution for the both of them [74]. Last but not the least, in-depth study of the shaftless flywheel's failure modes is needed so that the safety design could be improved to meet commercial standards.

REFERENCES

[1] Boden, T.A., G. Marland, and R.J. Andres. 2011. "Global, Regional, and National Fossil-Fuel CO2 Emissions. " Carbon Dioxide Information Analysis Center, Oak Ridge National Laboratory, U.S. Department of Energy, Oak Ridge, Tenn., U.S.A.

[2] "US Energy Information Administration," [Online]. Available: http://www.eia.gov/tools/faqs/faq.cfm?id=77&t=11.

[3] Karaeusel, J., Wanner, B., and Kesicki, F., 2010, "World Energy Outlook 2010 Edition," Executive Summary, International Energy Agency, pp. 431–442.

[4] Sebastián, R., and Peña Alzola, R., 2012, "Flywheel Energy Storage Systems: Review and Simulation for an Isolated Wind Power System," *Renewable and Sustainable Energy Reviews*, **16**(9), pp. 6803–6813.

[5] International Electrotechnical Commission. Electrical energy storage: white paper. Geneva, Switzerland: International Electrotechnical Commission, 2011.

[6] Patrick McMullen, V., "Reducing Peak Power Demand with Flywheel Technology." [Online]. Available: http://www.electricenergyonline.com/show_article.php?mag=&article=680

[7] Remillard, J. S., 2016, "Facility Scale Energy Storage: Applications, Technologies, and Barriers," *Strategic Planning for Energy and the Environment*, **36**(2), pp. 22–42.

[8] Janse Van Rensburg, P. J., Groenwold, A. A., and Wood, D. W., 2013, "Optimization of Cylindrical Composite Flywheel Rotors for Energy Storage," *Structural and Multidisciplinary Optimization*, **47**(1), pp. 135–147.

[9] R H. Jansen, T. P. Dever, "G2 Flywheel Module Design," NASA Technical Note, CR-2006-213862, pp. 1 – 20, August 2006.

[10] Cardenas, R., Pena, R., Perez, M., Clare, J., Asher, G., and Wheeler, P., 2006, "Power Smoothing Using a Flywheel Driven by a Switched Reluctance Machine," *IEEE Transactions on Industrial Electronics*, **53**(4), pp. 1086–1093.

[11] Sun, G., 2006, “Rotor Drop and Following Thermal Growth Simulations Using Detailed Auxiliary Bearing and Damper Models,” *Journal of sound and vibration*, **289**(521), pp. 334–359.

[12] Arvin, A. C., and Bakis, C. E., 2006, “Optimal Design of Press-Fitted Filament Wound Composite Flywheel Rotors,” *Composite Structures*, **72**(1), pp. 47–57.

[13] Abrahamsson, J., Hedlund, M., Kamf, T., and Bernhoff, H., 2014, “High-Speed Kinetic Energy Buffer: Optimization of Composite Shell and Magnetic Bearings,” *IEEE Transactions on Industrial Electronics*, **61**(6), pp. 3012–3021.

[14] Thelen, R. F., Herbst, J. D., and Caprio, M. T., 2003, “A 2 MW Flywheel for Hybrid Locomotive Power,” *Vehicular Technology Conference*, 2003. IEEE 58th, **5**, pp. 3231--3235.

[15] Ha, S. K., Han, H. H., and Han, Y. H., 2008, “Design and Manufacture of a Composite Flywheel Press-Fit Multi-Rim Rotor,” *Journal of Reinforced Plastics and Composites*, **27**(9), pp. 953–965.

[16] Perry Tsao, M. Senesky and S. R. Sanders, 2003, "An integrated flywheel energy storage system with homopolar inductor motor/generator and high-frequency drive," in *IEEE Transactions on Industry Applications*, **39** (6), pp. 1710-1725.

[17] Kailasan, A., Dimond, T., Allaire, P., and Sheffler, D., 2015, “Design and Analysis of a Unique Flywheel Energy Storage System - an Integrated Flywheel, Motor/generator and Magnetic Bearing Configuration,” *Journal of Engineering for Gas Turbines and Power*, **137**(April), pp. 1–12.

[18] Sung, T. H., Lee, J. S., Han, Y. H., Han, S. C., Choi, S. K., and Kim, S. J., 2002, “300 Wh Class Superconductor Flywheel Energy Storage System with a Horizontal Axle,” *Physica C: Superconductivity and its Applications*, **372**–**376**(PART 3), pp. 1451–1456.

[19] Jinji, S., Ziyan, J., Weitao, H., and Gang, L., 2017, “A Novel Integrated 4-DOF Radial Hybrid Magnetic Bearing for MSCMG,” *Journal of Magnetism and Magnetic Materials*, **421**, pp. 86–97.

[20] Park, J., 2008, “MIMO Active Vibration Control of Magnetically Suspended

Flywheels for Satellite Ipac Service MIMO Active Vibration Control of Magnetically Suspended Flywheels for Satellite Ipac Service,"Ph.D. Thesis, Texas A&M University.

[21] Lei, S., and Palazzolo, A., 2008, "Control of Flexible Rotor Systems with Active Magnetic Bearings," *Journal of Sound and Vibration*, **314**(1–2), pp. 19–38.

[22] Rafsanjan, S. T., Talebi, R. S., Toliyat, H. A., McMullen, P., Huynh, C., and Filatov, A., 2005, "Advanced High-Speed Flywheel Energy Storage Systems for Pulsed Power Applications." *IEEE Electric Ship Technologies Symposium*, 2005., Philadelphia, PA, pp. 379-386.

[23] Hofmann, H., and Sanders, S. R., 1996, "Synchronous Reluctance Motor / Synchronous Reluctance Motor/Alternator for Flywheel Energy Storage Systems," *Proceedings of the IEEE*, pp. 199–206.

[24] Nagorny, A. S., Dravid, N. V., Jansen, R. H., and Kenny, B. H., 2005, "Design Aspects of a High Speed Permanent Magnet Synchronous Motor / Generator for Flywheel Applications," *IEEE International Conference on Electric Machines and Drives*, pp. 635–641.

[25] "Active Power Inc," [Online]. Available: http://www.activepower.com/en-US.

[26] "Calnetix VDC," [Online]. Available: https://www.calnetix.com/vdc-kinetic-energy-storag.

[27] Lashway, C. R., Elsayed, A. T., and Mohammed, O. A., 2016, "DC Voltage Ripple Quantification for a Flywheel-Battery Based Hybrid Energy Storage System," *2016 IEEE Applied Power Electronics Conference and Exposition (APEC)*, IEEE, pp. 1267–1272.

[28] Azubalis, M., Baranauskas, A., and Tamulis, G., 2013, "Wind Power Balancing Using Flywheel Energy Storage System,", *Elektronika Ir Elektrotechnika*, **19**, pp. 19–23.

[29] Mousavi G, S. M., Faraji, F., Majazi, A., and Al-Haddad, K., 2017, "A Comprehensive Review of Flywheel Energy Storage System Technology," *Renewable and Sustainable Energy Reviews*, **67**, pp. 477–490.

[30] Abdeltawab, H. H., and Mohamed, Y. A. R. I., 2016, "Robust Energy Management of a Hybrid Wind and Flywheel Energy Storage System Considering Flywheel Power Losses Minimization and Grid-Code Constraints," *IEEE Transactions on Industrial Electronics*. **63** (7), pp. 4242-4254.

[31] Carrasco, J. M., Franquelo, L. G., Bialasiewicz, J. T., Member, S., Galván, E., Guisado, R. C. P., Member, S., Ángeles, M., Prats, M., León, J. I., and Moreno-Alfonso, N., 2006, "Power-Electronic Systems for the Grid Integration of Renewable Energy Sources : A Survey," *IEEE Transactions on Industrial Electronics*, **53**(4), pp. 1002–1016.

[32] Li, W., and Joós, G., 2007, "Comparison of Energy Storage System Technologies and Configurations in a Wind Farm," *Power Electronics Specialists Conference*, pp. 1280–1285.

[33] Vajda, I., Kohari, Z., Benko, L., Meerovich, V., and Gawalek, W., 2003, "Investigation of Joint Operation of a Superconducting Kinetic Energy Storage (Flywheel) and Solar Cells," *IEEE Transactions on Applied Superconductivity*, **13**(2), pp. 2169–2172.

[34] Kirby, B. J., 2004, "Frequency Regulation Basics and Trends."

[35] Weissbach, R. S., Karady, G. G., and Farmer, R. G., 1999, "Dynamic Voltage Compensation on Distribution Feeders Using Flywheel Energy Storage," *IEEE Transactions on Power Delivery*, **14**(2), pp. 465–471.

[36] Hedlund, M., Lundin, J., de Santiago, J., Abrahamsson, J., and Bernhoff, H., 2015, "Flywheel Energy Storage for Automotive Applications," *Energies*.**8**(10), 10636-10663

[37] Smith, R. A., and Pullen, K. R., 2015, "Optimisation of Flywheel Energy Storage Systems with Geared Transmission for Hybrid Vehicles," *Mechanism and Machine Theory*, **87**, pp. 191–209.

[38] Yimin Gao, Gay, S. E., Ehsani, M., Thelen, R. F., and Hebner, R. E., 2003, "Flywheel Electric Motor/generator Characterization for Hybrid Vehicles," *2003 IEEE 58th Vehicular Technology Conference*, pp. 3321–3325 Vol.5.

[39] Park, J., Palazzolo, A., and Beach, R., 2008, "MIMO Active Vibration Control of Magnetically Suspended Flywheels for Satellite IPAC Service," *Journal of Dynamic Systems, Measurement, and Control*, **130**(4), p. 41005.

[40] Christopher, D. A., Beach, R. F., and Barton, J. R., "A Flywheel Energy Storage System Test on the International Space Station," *IECEC-97 Proceedings of the Thirty-Second Intersociety Energy Conversion Engineering Conference*, pp. 1762–1766.

[41] Edwards, J., Aldrich, J. W., Christopher, D. A., Beach, R. F., and Barton, J. R., "Flight Test Demonstration of a Flywheel Energy Storage System on the International Space Station," *Proceedings of the IEEE 1997 National Aerospace and Electronics Conference.* pp. 617–621.

[42] Swett, D. W., and Blanche IV, J. G., 2005, "Flywheel Charging Module for Energy Storage Used in Electromagnetic Aircraft Launch System," *IEEE Transactions on Magnetics*, **41**(1 II), pp. 525–528.

[43] Department of Energy, *20 MW Flywheel Energy Storage Plant*.

[44] "Beacon Power" [Online]. Available: http://beaconpower.com/carbon-fiber-flywheels/.

[45] "Calnetix" [Online]. Available: https://www.calnetix.com/products.

[46] Solis, O., Castro, F., Bukhin, L., Pham, K., Turner, D., and Thompson, G., "Saving money every day: la metro subway wayside energy storage substation."

[47] Wheals, R. J., Wheals, J. C., Lanoe, W., Engineering, A., Bombardier, M., and Taylor, J., 2016, "Rail Hybrid Using Flywheel," Copenhagen, **1115**, pp. 30–12.

[48] "Spinning Wheel," p. [Online]. Available: www.transportengineer.org.uk.

[49] Sanders, S., Senesky, M., He, M., and Hope, L. Ten, 2015, *Low-Cost Flywheel Energy Storage Demonstration*.

[50] Li, X., Anvari, B., Palazzolo, A., Wang, Z., and Toliyat, H., 2018, "A Utility Scale Flywheel Energy Storage System with a Shaft-Less, Hub-Less, High Strength Steel Rotor," *IEEE Transactions on Industrial Electronics*, **65**(8), pp. 6667–6675. doi: 10.1109/TIE.2017.2772205

[51] Anvari, B., Li, X., Toliyat, H. A., Palazzolo, A., Wang, Z., and Han, X., 2017, "A Coreless Permanent-Magnet Machine for a Magnetically Levitated Shaft-Less Flywheel," *2017 IEEE International Electric Machines and Drives Conference, IEMDC 2017*.

[52] Li, X., Palazzolo, A., McMullen, P., Wang, Z., and Tingey, D., 2015, "Shaft-Less Energy Storage Flywheel," *Proceedings of the ASME 2015 9th International Conference on Energy Sustainability*.

[53] Bolund, B., Bernhoff, H., and Leijon, M., 2007, "Flywheel Energy and Power Storage Systems," *Renewable and Sustainable Energy Reviews*, **11**(2), pp. 235–258.

[54] Genta, G., 1985, "Application of Flywheel Energy Storage Systems," *Kinetic Energy Storage*, Elsevier, pp. 27–46.

[55] Ha, S. K., Kim, S. J., Nasir, S. U., and Han, S. C., 2012, "Design Optimization and Fabrication of a Hybrid Composite Flywheel Rotor," *Composite Structures*, **94**(11), pp. 3290–3299.

[56] Krack, M., Secanell, M., and Mertiny, P., 2010, "Cost Optimization of Hybrid Composite Flywheel Rotors for Energy Storage," *Structural and Multidisciplinary Optimization*, **41**(5), pp. 779–795.

[57] Den Hartog, J. P., 1952, *Advanced Strength of Materials*.

[58] Clark, D. J., Jansen, M. J., and Montague, G. T., 2004, *An Overview of Magnetic Bearing Technology for Gas Turbine Engines*.

[59] Mcmullen, P. T., Huynh, C. S., and Hayes, R. J., 2000, "Combination Radial-Axial Magnetic Bearing." *7th International Symposium on Magnetic Bearing.ETH*, Zurich.

[60] Han, B., Zheng, S., Le, Y., and Xu, S., 2013, "Modeling and Analysis of Coupling Performance between Passive Magnetic Bearing and Hybrid Magnetic Radial Bearing for Magnetically Suspended Flywheel," *IEEE Transactions on Magnetics*, **49**(10), pp. 5356–5370.

[61] Imoberdorf, P., Zwyssig, C., Round, S. D., and Kolar, J. W., 2007, "Combined

Radial-Axial 500 , 000 Rpm Permanent Magnet Machine," *Twenty-Second Annual IEEE Applied Power Electronics Conference and Exposition*, pp. 1434–1440.

[62] Jiancheng, F., Jinji, S., Hu, L., and Jiqiang, T., 2010, "A Novel 3-DOF Axial Hybrid Magnetic Bearing," *IEEE Transactions on Magnetics*, **46**(12), pp. 4034–4045.

[63] Eryong, H., and Kun, L., 2012, "Investigation of Axial Carrying Capacity of Radial Hybrid Magnetic Bearing," *IEEE Transactions on Magnetics*, **48**(1), pp. 38–46.

[64] Mohamed, A. M., and Emad, F. P., 1989, "Conical Magnetic Bearings with Radial and Thrust Control," *Proceedings of the IEEE Conference on Decision and Control*, **1**(12), pp. 554–561.

[65] Lee, C.-W., and Jeong, H.-S., 1996, "Dynamic Modeling and Optimal Control of Cone-Shaped Active Magnetic Bearing Systems," *Control Engineering Practice*, **4**(10), pp. 1393–1403.

[66] Xu, S., and Fang, J., 2014, "A Novel Conical Active Magnetic Bearing with Claw Structure," *IEEE Transactions on Magnetics*, **50**(5), pp. 1–1.

[67] Tang, J., Sun, J., Fang, J., and Shuzhi Sam, G., 2013, "Low Eddy Loss Axial Hybrid Magnetic Bearing with Gimballing Control Ability for Momentum Flywheel," *Journal of Magnetism and Magnetic Materials*, **329**, pp. 153–164.

[68] Bjorn, G., and Semlyen, A., 1999, "Rational Approximation of Frequency Domain Responses by Vector Fitting," *Power Delivery, IEEE Transactions on*, **14**(3), pp. 1052–1061.

[69] Chiesa, N., and Gustavsen, B., 2014, "Frequency-Dependent Modeling of Transformer Winding Impedance from R/L Measurements," *IEEE Transactions on Power Delivery*, **29**(3), pp. 1511–1513.

[70] Okada, Y., Nagai, B., Shimane, T., and Bearing, T. M., 2014, "Cross-Feedback Stabilization of the Digitally Controlled Magnetic Bearing,". *ASME. J. Vib. Acoust*. 1992;**114**(1):54-59.

[71] Ahrens, M., Kucera, L., and Larsonneur, R., 1996, “Performance of a magnetically suspended flywheel energy storage device,” *IEEE Transactions on Control Systems Technology*, **4**(5), pp. 494–502.

[72] Dspace, “DS1103 Datasheet” [Online]. Available: https://www.dspace.com/en/inc/home.cfm.

[73] Li X, Palazzolo A. Multi-Input Multi-Output control of a utility scale, shaft-less energy storage flywheel with a 5-DOF combination magnetic bearing. *ASME. J. Dyn. Sys., Meas., Control*. 2018. doi:10.1115/1.4039857.

[74] Monmasson, E., and Cirstea, M. N., 2007, “FPGA Design Methodology for Industrial Control Systems - A Review,” *IEEE Transactions on Industrial Electronics*, **54**(4), pp. 1824–1842.

APPENDIX

Flywheel Controller Operation Manual

This Manual is for reference only, see the design manual for details. The error signals are generated by comparing sensor reading and sensor targets. After the error signals are transformed into the controller's coordinate, they go through five channels for feedback control, as depicted in Figure A.1

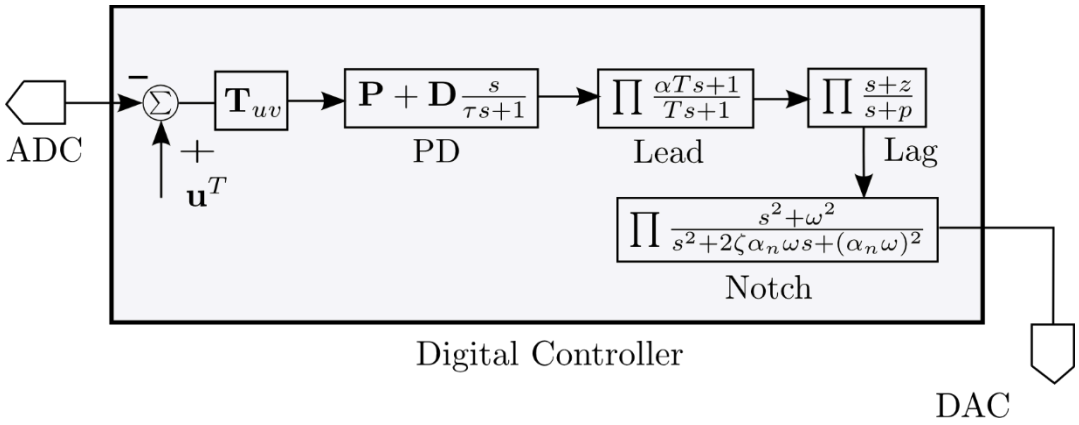

Figure A.1 Controller Architecture of a Single Channel

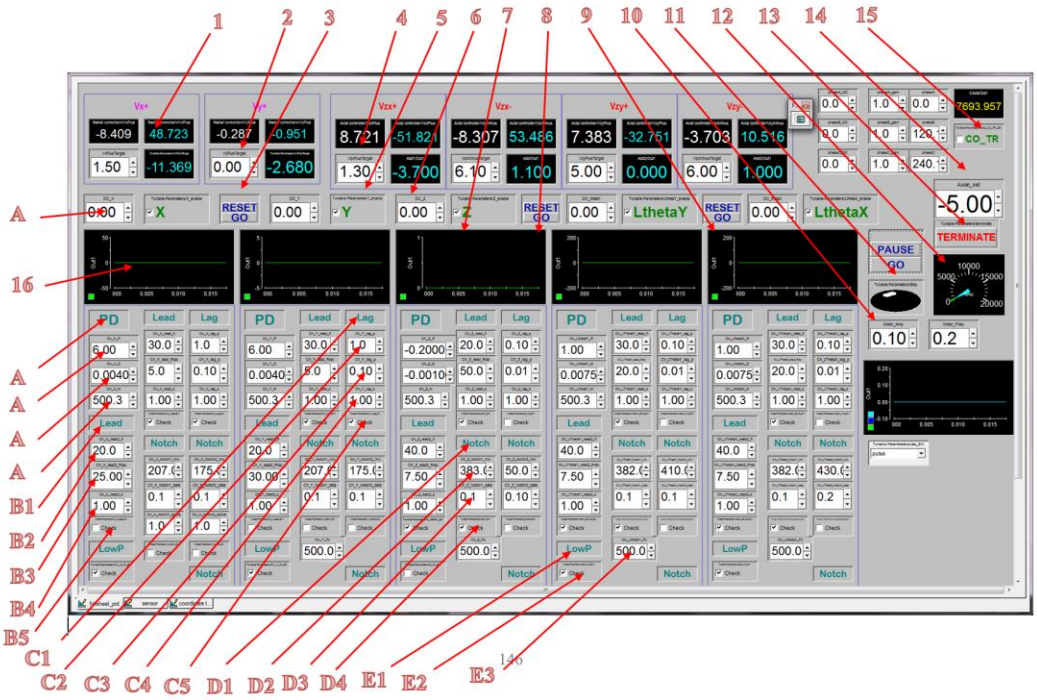

Figure A.2 Controller Main Panel

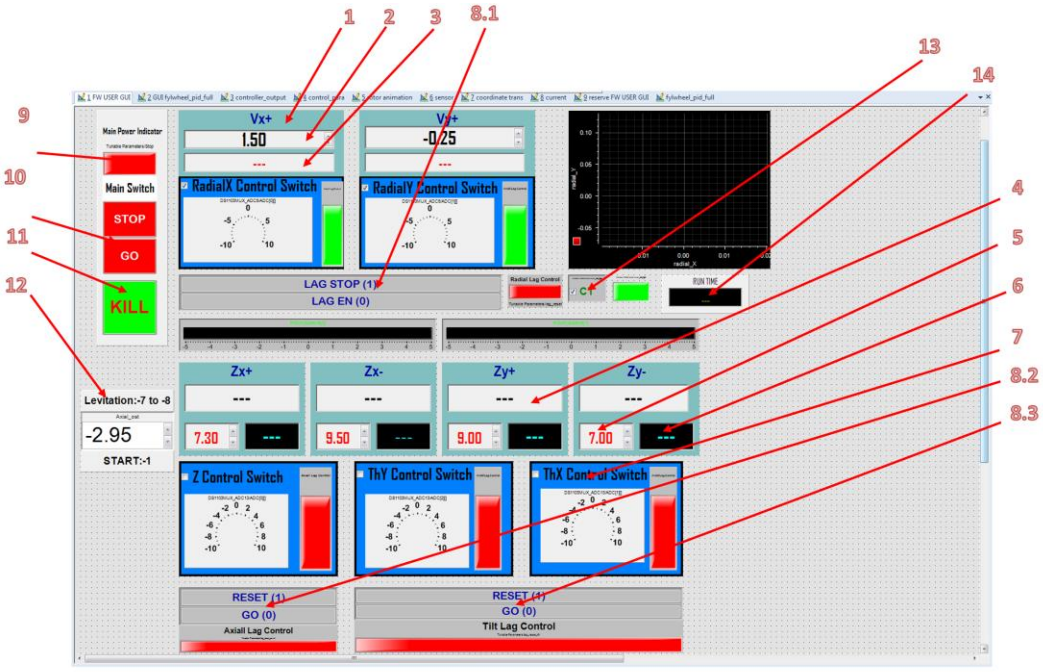

Figure A.3 Controller Operational Panel #1

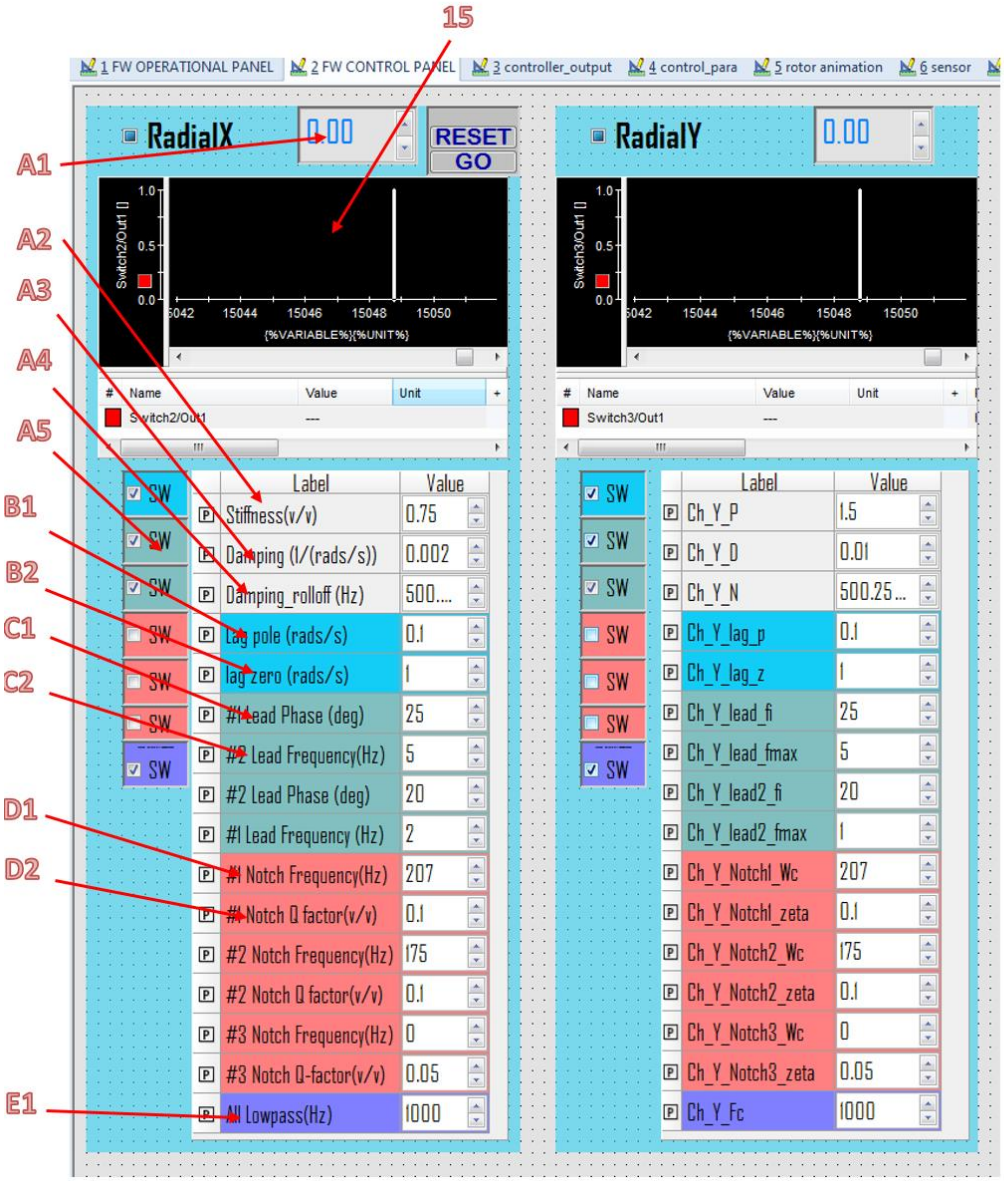

Figure A.4 Operational Panel #2

Button Description

Control Panel #1 (main, see Figure A.2)

1. Sensor label (X+,Y+,Vzx+, Vzx-, Vzy+, Vzy-)
2. Sensor voltage reading (radials).
3. Sensor voltage targets.
4. Sensor voltage reading (axial).
5. Sensor voltage targets (axial) after offset.
6. Real Sensor voltage targets (axial): this is for axial targets only.

   Real=targets(#5)+offset (#13)
7. Controller switch for the subject (UNCHECK will result in 0 output)
8. RESET and GO control for the axial lag integrator
9. RESET and GO control for the tilts lag integrator
10. Controller operation indicator (red on, black off)
11. Controller output switch: when press PAUSE, all outputs become zeros; press GO, resume all outputs
12. Flywheel speed meter
13. Controller TERMINATE switch when pressed; the program will be terminated by force.
14. Axial offset control: this button provides the same amount of offset for axial targets.
15. The coordinate transform switch
16. Output waveform plot for each controlling subject

A1 Feedforward control for each channel.

A2 PD stage label

A3 Proportional parameter for PD stage.

A4 Derivative parameters for PD stage.

A5 Filter parameters for Derivative in Hertz.

B1 Lead stage label

B2 Lead phase in degree

B3 Lead frequency in Hertz

B4 Lead stage switch: UNCHECK will bypass it

C1 Lag stage label

C2 Lag zero location

C3 Lag pole location

C4 Lag gain (leave it as unity in most cases)

C5 Lag stage switch: UNCHECK will bypass it

D1 Notch label

D2 Notch frequency in Hertz

D3 Notch 1/Q factor

D4 Notch stage switch: UNCHECK will bypass it

E1 Low pass filter label

E2 Low pass filter cutoff frequency

E3 Low pass filter switch: UNCHECK will bypass it

OPERATIONAL PANEL #1 (see Figure A.3)

1. Sensor label (X+, Y+, Vzx+, Vzx-, Vzy+, Vzy-)
2. Sensor voltage reading (radials).
3. Sensor voltage targets.
4. Sensor voltage reading (axial).
5. Sensor voltage targets (axial) before offset.
6. Real Sensor voltage targets (axial): after offset.
7. Controller switch for the subject (UNCHECK will result in 0 output)
8. RESET and GO control for the lag integrator (careful with windup)
9. Controller operation indicator (RED OFF, GREE ON)
10. Controller output switch: when press STOP, all outputs become zeros; press GO, resume all outputs (code is still running in STOP mode)
11. Controller TERMINATE switch when pressed; the program will be terminated by force
12. Axial offset control:
13. The coordinate transform switch
14. Running time clock in seconds
15. Output waveform plot for each controlling subject

OPERATIONAL PANEL #2 (see Figure A.4)

A1 Feedforward control for each channel.

A2 Proportional parameter for PD stage

A3 Derivative parameters for PD stage

A4 Filter parameters for Derivative in Hertz

A5 Switch control panel (color coded)

a. Lead stage switch: UNCHECK will bypass the lead

b. Lag stage switch: UNCHECK will bypass the lag

c. Notch stage switch: UNCHECK will bypass the notch

d. Low pass filter switch: UNCHECK will bypass the lowpass

B1 Lead phase in degree

B2 Lead frequency in Hertz

C1 Lag zero location

C2 Lag pole location

D1 Notch frequency in Hertz

D2 Notch 1/Q factor

E1 Low pass filter label

E2 Low pass filter cutoff frequency

Levitation Procedure

General rules

1. Output waveform, sensor readings, coil temperatures, and spectrum analyzers are useful in finding and solving potential problems.
2. Always make sure PAs are off before turn on the controller.
3. Always reset lag integrator before enabling the lag.
4. Always monitor radial and axial coil currents and temperatures during levitation.

For Radial Levitation

1. Make sure PAs are off, and the controller is paused
2. Bring up the flywheel so that all the axial sensor readings are within range (#4)
3. Put the flywheel on the Vertical ball transfers (VBT)
4. Disable ‘Z’,’LthetaY’ and ‘LthetaX’ controls by unchecking (#7)
5. Enable ‘X’ and ‘Y’ control (#7)
6. Set ‘X’ and ‘Y’ PD gains and lag control parameters (A2~A5 and C1~C5)
7. Observe the waveform window; the output waveform should be zero.
8. Set the X and Y sensor targets
9. Check the sensor readings of X and Y
10. Adjust the flywheel horizontally if necessary.
11. Reset ‘X,’ ’Y’ lag integrator.
12. Click on go controller (#11)
13. Observe the X and Y sensor readings to see if they go to the targets

14. If the X and Y readings are off target by a constant error, turn on the lag integrator and observe.

TABLE A.1 RADIAL LEVITATION TROUBLESHOOT TABLE

Potential Problem description	*Suggestions*
The flywheel is quickly pushed off targets and stuck during levitation	Overshoot: turn up damping and lower proportion and go back to step 8
The flywheel is slowly bouncing back and force	Not enough stiffness and damping. Raise them slowly
Output has a lot of spikes in the waveform windows. Humming noise from the stator	Damping too high: Lower damping and try to Lower low-pass filter cut off frequency, if the noise is significant.
The flywheel is in a slow mode, but damping is already high	Put a low-frequency lead compensator. Start with small phase lead.

For Axial levitation

1. Make sure axial PAs are off.
2. Bring up the flywheel to the right height and make sure that the flywheel is close to level.
3. Check axial sensor reading.
4. Record the axial sensor readings as the targets before offset (#5).
5. Put the flywheel on VBT.
6. Follow the radial levitation procedure and make sure there is a stable radial levitation.
7. Disable ‘Z’,’LthetaY’ and ‘LthetaX.’
8. Set ‘Z’,’LthetaY’ and ‘LthetaX’ control PD according to the troubleshooting table. Disable all rest compensator at this moment.
9. Check if the PAs are turned off.
10. Hit go button.
11. Turn on ‘Z’ only and give small offset amount in #13. Offset needs to be negative.
12. Continually monitor radial levitation by looking at the output windows, sensor readings, and coil temperature during full levitation. If any problem occurs, refer to the troubleshoot Table A.1
13. Check waveform windows and axial sensor reading to see if the flywheel has come upward.
14. If yes then go to the next step, if not check the current output and make sure the real target (#6) is smaller than the sensor reading (#4), increase offset if needed.

15. Turn on the tilt control with only PD.
16. During the levitation most like vibration problem is going to happen, refer to Table A.2
17. Now that the vibration is gone, the flywheel still may not be levitated fully at this moment.
18. Refer to nonvibration troubleshoot table (Table A.3). If nonvibration problem occurs during this process. Go back to 16.
19. Continuously watch temperature during the levitation.

TABLE A.2 AXIAL LEVITATION VIBRATION TROUBLESHOOT TABLE

Potential Problem description	*Possible causes and suggestions*
Axial vibration near 100hz, vibration is from the stator	Stator mode
Axial vibration at 232Hz/383hz, vibration source is the flywheel	Flywheel bending mode, use a notch
Any other low-frequency vibration	Use lead at the frequency start with small phase
Any other high-frequency vibration	use a notch with 1/Q=0.1 first, go smaller if necessary
New vibration when a lead/notch is placed	Lower the phase lead, reduce the notch Q
New Vibration occurs when the flywheel is about to leave the ball transfers	Try to turn off low-frequency lead to see if helps first. In some cases, it may need to be moved to the frequency where the vibration occurs because the system has changed.

TABLE A.3 AXIAL LEVITATION NON-VIBRATION TROUBLESHOOT TABLE

Potential Problem description	*Possible causes and suggestions*
Significant un-levelness observed during levitation.	1. The target is not acquired with leveled flywheel; it also causes considerable tilt current: Adjust targets to reduce tilting current and increase offset (#13) 2. Feedback has the wrong sign, chose the gain sign that reduces the error signal
The flywheel is bouncing up and down (nonvibration)	1. Flywheel partially rests on VBT: increase offset 2. controller output saturated: Restart levitation with a closer airgap. 3. Shorted coil,
The flywheel is rocking (non-vibration)	1. Flywheel partially rest on VBT-> increase offset or lower the VBT 2. Shorted coil
output waveform with significant spikes	1. Lower low pass cut off frequency 2. Lower damping 3. Check amplifiers bus voltage 4. Check if coils overheated